Material studies for flexible 3rd generation solar cells

Mohammad Ishaq Alkhatab

FACULTÉ DES SCIENCES ET TECHNOLOGIES

Université de Lille

THESE DE DOCTORAT

Présentée à

l'Université de Lille

Ecole Doctorale Régionale Sciences Pour l'Ingénieur

Université Lille Nord de France

pour l'obtention du grade de

Docteur en Électronique, microélectronique, nanoélectronique et micro-ondes

Par

Mohammad Ishaq Alkhatab

Material studies for flexible 3rd generation solar cells
Etudes de matériaux pour cellules solaires flexibles de 3ème génération

Soutenue le 22 Septembre 2020

Denis REMIENS	Président	Professeur, Université Polytechnique Hauts de France (Valenciennes)
Mireille RICHARD	Rapporteur	Directeur de Recherche CNRS, Institut des Matériaux Jean Rouxel de Nantes
Silvère BARRAT	Rapporteur	Professeur, Mines Nancy, Institut Jean Lamour
Abdelkader AISSAT	Examinateur	Professeur, Université de Blida 1
Ghassan JABBOUR	Examinateur	Professeur, Université d'Ottawa
Basma EL ZEIN	Co-encadrante	Assistant Professeur. University of Business and Technology (Djeddah)
Jean-Pierre VILCOT	Directeur de thèse	Directeur de Recherche CNRS, Institut d'Electronique, de Microélectronique et de Nanotechnologie (Villeneuve d'Ascq)

Abstract

Meeting the vast needs of energy all over the world in an environmentally sustainable way is one of the most essential technological challenges facing us today. During the photovoltaic technology development, numerous materials are investigated in order to obtain high-quality photovoltaic cells, evaluated by three major criteria: efficiency (ratio of the electric power output to the light power input), use of non-toxic materials and production cost.

Since the solar source is abundant, renewable, worldwide available and free of charge, considerable attention is given to get solar cell energy as eco-green as it can be.

Considering more particularly photovoltaics, solar energy is converted to electrical energy by a sequence of events: absorption of light, generation of charges carriers (electrons and holes), photogenerated carriers separation and transportation to electrodes.

Among all studied technologies, quantum dots sensitized solar cells (QDSSC's) are investigated owing to their promising power conversion efficiency, their simple device fabrication process, and their low cost.

Zero-dimensional nanostructures have gained broad interest due to their unique properties, especially tuning the bandgap based on their size. Different types of structures that play the role of the absorber could then be studied by tuning their bandgap either by changing their size or changing the degree of cation disorder. In this research, La_2CuO_4 material has been investigated in terms of surface morphology, optical absorption, and electron mobility as an absorption layer in the solar cell. Also, different approaches and techniques were used for its fabrication, such as pulse laser deposition (PLD) and sputtering techniques.

Aside from absorber layers, the Transparent Conductive Oxides (TCOs) are an example of electrode material; within this group, Indium Tin Oxide (ITO) and Fluorine doped Tin Oxide (FTO) are widely used in new solar cells designs. On the other hand, they have many drawbacks as limited availability of indium (rare element), instability in the presence of acid or base, limited transparency in the near-infrared region, as well as current outflow caused by FTO structure defects. The search for newer electrode materials with high stability, high transparency, and excellent conductivity is, therefore, a critical goal for solar

cells. Graphene appears to have none of these drawbacks, as well as it is cheap and sustainable. Moreover, the graphene has also been investigated in terms of durability and electron conductivity as top and back electrodes: various fabrication techniques were used, such as chemical vapor deposition (CVD) and laser-induced Graphene (LIG).

Keywords: Sensitized, solar cells, Quantum Dots, electrodes and Graphene

Dedication

To my family for the love that always lights my way.
I love you all.

Acknowledgments

My thesis has been carried out at the Université de Lille, with the support of two great entities, the Institut d'Electronique, de Microélectronique et de Nanotechnologie (IEMN) in France and the University of Business and Technology in KSA. It was a dream that came true. I am very grateful for all the knowledge and experience I gained from both institutions in all aspects of my life.

Humbly, I would like to start by acknowledging my supervisors, Dr. Jean-Pierre Vilcot and Dr. Basma EL Zein, for their great support, encouragement, and guidance throughout every step in my Ph.D. As the main supervisory and the leader of the OPTO group, Dr. Jean-Pierre Vilcot has been there in all parts of my research, providing the guidance needed in all forms. Dr. Basma EL Zein was the key that started the Ph.D. program, with her patience and support towards Ph.D. students in a startup program that was created under her Deanship. She always finds the time for our problems despite her tight schedule. I am honored and very fortunate to had the chance to meet and work with both of them.

My gratitude to Dr. Abdullah Dhlan and Mohaned Dhlan for their help in times of need and for giving me a chance to start this program.

A big thanks to Dr. Boubakeur Ayachi and IEMN's OPTO group for their help and support during my laboratory work in IEMN. I could not achieve most of my work there without their help. Without forgetting the memorable times we spend together.

Last but not least, my friend Dr. Ahmad Shawqi deserves exceptional thanks. He supported and guided me in the last three years, pushing me to finish my studies despite all the circumstances.

Preamble

The seed of this work was the collaboration between the University of Business and Technology (UBT) in Jeddah, Saudi Arabia, and the Institut d'Electronique de Microélectronique et de Nanotechnologie (IEMN, University of Lille) in France.

The collaboration topic dealt with the development of new photovoltaic technologies based on green materials and techniques. At that time, this topic was new in both institutions. UBT, as a young established university, pursued the service of the Core Labs at King Abdullah University of Science and Technology (KAUST) located in Thuwal.

In the first two years of my work, the development, fabrication, and characterization of the materials took place in Saudi Arabia with short stays in France mainly to carry out some complementary characterizations. The last part of my work was done in France to continue investigating different materials and other deposition techniques. Nevertheless, it reasonably soon became apparent that the initial goal targeting a full working cell based on new materials within my Ph.D. work was particularly challenging, and work was built around investigating material growth conditions and corresponding material properties in order reaching the initial goal eventually.

Contents

Chapter 1

Introduction and Motivations

1.1 Introduction

More and more, we become depending on the technology for our life routine; it becomes necessary more than a luxury spending energy - electrical primarily - in every second of our life. The more we use, the more the world's hunger for energy increases and it made be clear that pursuing such a way of keeping current rules will give an impossible equation to solve. Today, the population is around seven billion and is estimated to grow to nine billion by 2050, and about ten billion by 2100. [1] Adding to that, most of this progression is located in the fast-growing countries, which means even faster energy demands. To meet those needs, a range of technologies for energy supply was developed in several directions, most of the time, without any constraints or concerns. [2]

With the awareness that the key to solve this energy demand will not be represented by oil, gas, coal, or other fossil energy sources since:

- they are expected to run out eventually,
- their harmful effects on the environment, inherited from the past century human activity, will lead us to pay for it by spending more energy to purify the earth from that heritage in the near future [3],

a way of thinking in harvesting energy raised with offshoots such as eco-green, sustainable, reliable, and affordable concerns. The sun displays an enormous mass of energy source -about 386 billion billion megawatts evaluated by NASA- generated by nuclear fusion reactions. It represents one of the suitable leading solutions to satisfy the energy request since it fulfills all the main conditions with the addition of its vast and free availability, its main drawback consisting of its intermittent and weather-dependent nature. Different technologies utilize sun energy directly in such ways:

a. Solar thermal collectors exploit the heat energy from the sunlight.
b. Solar fuels convert and save sunlight energy under chemical reactions.
c. Solar cells, also known as photovoltaics (PV), converts sunlight energy directly into electricity.

In this thesis, our concern is the photovoltaic technology that has seen significant development primarily in the past few decades, owing to the fluctuation of the prices of other sources like oil and the global awareness about climate change, the reduced carbon

footprint and the goal of making electricity affordable to every household. Many studies support this technology since harvesting only the equivalent to 1.5 surface area of the landscape of the Sahara Desert with 10% efficient solar panels could cover the present global energy needs. [4]

The increased interest in PV is observed from the industrial sector for which the global market capacity leaped rapidly for the past decade; it reached around 430GW of cumulated power by the end of 2018 (Fig. 1).

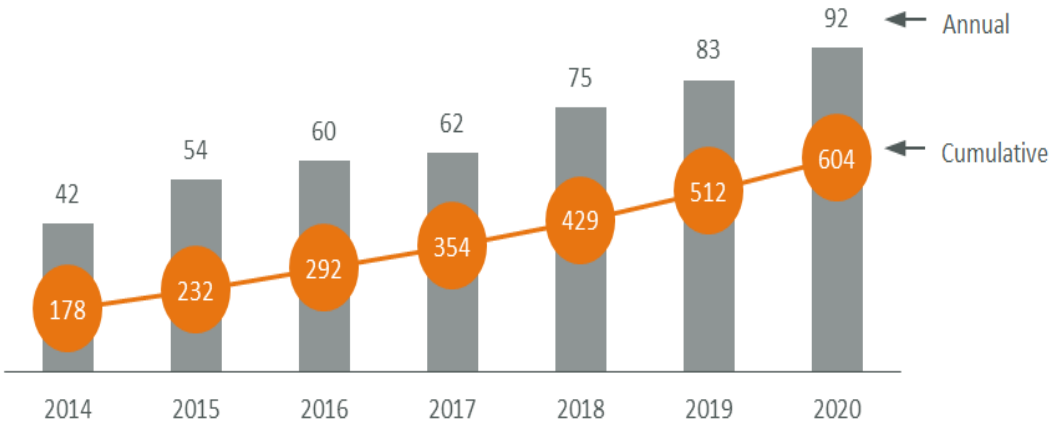

Figure 1: Global annual and cumulative installations in (GW), 2014–2020 [5].

1.2 The beginning of photovoltaics

Historically, the starting point was when Becquerel first observed the photovoltaic effect. It was definitely as the emergence of an electric voltage between two electrodes within a liquid system when a shining light introduces into this system.

Adams and Day made the first demonstration of the photovoltaic effect in a solid-state system in 1876. Then Fritts, in 1883, was there to present what is considered as the first thin-film solar cell. After Fritts, development was prolonged to what is called the copper-cuprous oxide junction. In the same years, the potentialities of silicon as a PV material was rising [6-9].

The properties of sharpened metal point contacts to various crystals were known since at least 1874 [10], and silicon was firstly receiving full attention for its use in such point

contact rectifiers. At the starting point of radio development, such silicon crystal rectifiers were the most commonly used in communication applications, but most crystal rectifiers were replaced with the development of thermionic tubes. Tungsten demonstrated to be a suitable material for making contact points with silicon surfaces. Research into the purity of silicon also led to further understanding of the properties of this material. [10].

In search of recrystallized pure silicon prepared for this purpose, Ohl [11] discovered the presence of a well-defined potential barrier in ingots from commercially high-purity silicon. In 1941, silicon photovoltaic devices based on these natural junctions were described [11]. The high-purity silicon showed a good photovoltaic response, exhibited a high thermoelectric coefficient, and had excellent rectifying properties. The silicon developed a negative potential when it was illuminated and had to be biased negatively in order to show low resistance to current flow through the barrier or the point of contact onto it [12]. Using silicon for solar cells had a significant impact on the development timescale of photovoltaic technology. However, before going through that and the different paths that it took until modern technology, it would be preferable to explain the solar cell concept first.

1.3 The concept of early solar cells

To reveal how early solar cells – the name early solar cells as the oldest concept of solar cells illustrated from many references - harvest solar energy, two issues come in the picture. The first one is the device that implies its design, materials, and fabrication process. The second part is the light, which consists of photons and their energy and how they affect the device behavior.

The early solid-state solar cell was silicon-based. Silicon has four valence electrons in its pure crystalline form. Introducing atoms with a different number of valence electrons into the crystal, in a process called "doping", will change the overall balanced number of electrons. For example, doping using an atom of the 3rd group of the periodic table like boron, indium, or gallium that reduces the valence electron number by one for every replaced atom of the semiconductor material produces a p-type semiconductor. On the other hand, doping using an atom of the 5th group of the periodic table like arsenic,

antimony or phosphorus, will add one extra valence electron, then producing an n-type semiconductor.

In those materials, the energy required to remove the extra electron or to fill its vacancy - or hole - is quite small, and the thermal energy in the crystal is sufficient for this purpose. Thus, the electron, or hole, moves about freely in the crystal and contributes to the electrical conductivity just as in metals, although in the semiconductor case, the conductivity is much smaller than in metals.

An interesting thing happens to the electrons and holes once n-type and p-type semiconductors are attached. At first, there will be a significant number of mobile electrons within the n-type side, but few mobile electrons in the p-type side due to the respective doping of those materials and vice versa. Therefore, due to the random thermal motion of the free electrons and holes, electrons from the n-type side diffuse into the p-type side. Similarly, holes on the p-type side diffuse across into the n-type side. This would continue until eventually the electrons and holes uniformly distribute throughout the two semiconductors. However, as the electrons in the n-type material diffuse towards the p-type side, they leave behind positively charged ions near the interface.

Similarly, the holes in the p-side region diffuse towards the n-side and leave behind negatively charged ions. These fixed ions build up an electric field right in the interface region. This electric field points from the positively charged ions in the n-side material to the negatively charged ions in the p-side material. [13] This generated electric field influences the free charges with the electrons attracted towards the positive ions (n-type) and the holes attracted towards the negative ions (p-type). Thus, the electric field causes some of the electrons and holes to flow in the opposite direction to the flow caused by diffusion, denoted as drift process, until an equilibrium state is reached, as shown in Fig. 2.

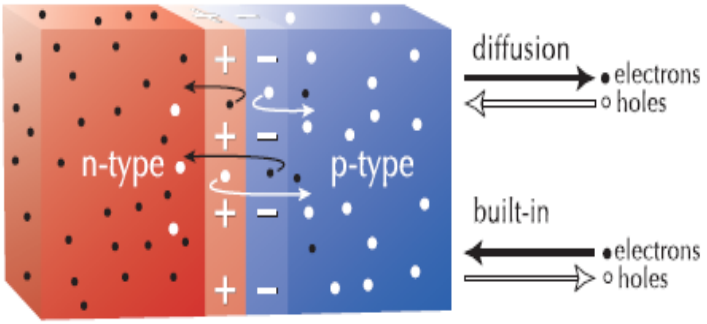

Figure 2: Displacement of mobile electrons and holes due to diffusion and drift phenomena [13].

This junction has so a depleted zone of free carriers close to the interface in which an internal electric field acts; those are the keys to the operation of the solar cells that are p-n junctions [13, 14].

In order to understand how light interacts with the semiconductor material constituting the solar cell, one has to consider the light wave under its quantum description as photons composition. Having sufficient energy when they hit the semiconductor to excite the electrons into a higher energy state, the valence bond is broken – note that the bonds are partially broken; otherwise, the silicon would melt – and a free hole-electron pair is created. If those pairs are near the junction, the electrical field will cause them to separate so that the holes will flow into the p- side material and electrons into the n- side material creating a potential difference, as shown in (Fig. 3).

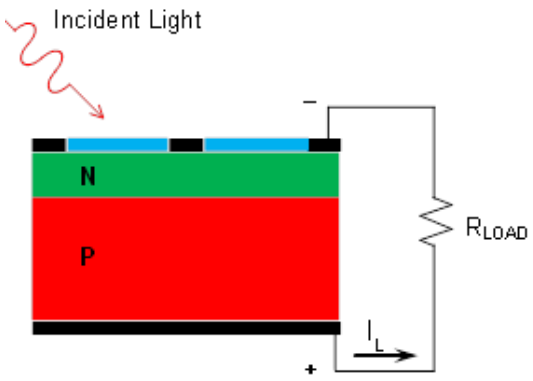

Figure 3: Basic structure of a solar cell based on a p-n junction in a functional electrical circuitry. I_L results from solar illumination, and R_L is the load resistance.

It is essential to mention that the electrons and holes can remain excited only for a short period. In a process called recombination, excited electrons stray too close to holes, and

the two fall back into combined positions. When that happens, the electrical energy - free carriers - is lost as a thermal release. The solar cell efficiency will then decrease as much as the number of recombination increases. That is why free carriers should be collected before that any recombination happens. [13].

1.4 Important factors in photovoltaics

PV technologies, like any other energy technology, have to concern with many factors before it can be considered a success. The most common of those factors are efficiency in conversion of energy, cost (that is in terms of fabrication and its feasibility payback), lifetime and recycling. As mentioned before, other recent aspects join such as environmental footprint, sustainability and, for particular applications, flexibility.

Irrespective of the types of solar cells, most of them share a similar operation principle behind their behaviors. Such a property is solar cell efficiency, abbreviated as η, is its main primary functional parameter. It is also the main parameter that is used to compare solar cell technologies and structures between each others. It is also known as the power conversion efficiency or PCE and, as it will be detailed below, it can be obtained almost effortlessly by comparing the behavior of solar cells under illumination and darkness.
It is noted that in darkness, the PV cell acts as a diode. Under illumination, the light acts as a free carrier generator, so as a current generator. Thus, in a first approach, solar cells can be electrically represented as a current source in parallel with a diode [15].
The PV cell current is treated as the sum of dark (I_0 is the diode saturation current) and photo-generated (I_L) currents.

$$I = I_0 \left[e^{\frac{qv}{KT-1}} \right] - I_L$$

We achieve a solar cell that has a typical diode behavior in darkness and a vertical shift caused by the light-induced current under illumination shown in (Fig.4) on the current-voltage curve [16-18]. Solar cell efficiency can be predicted based on this current-voltage curve. The quadrant of interest is the lower right one (V>0, I <0). It is usually the only one

that is shown, and, by convention, it is usually reversed relative to the X-axis (V) in order to display positive currents.

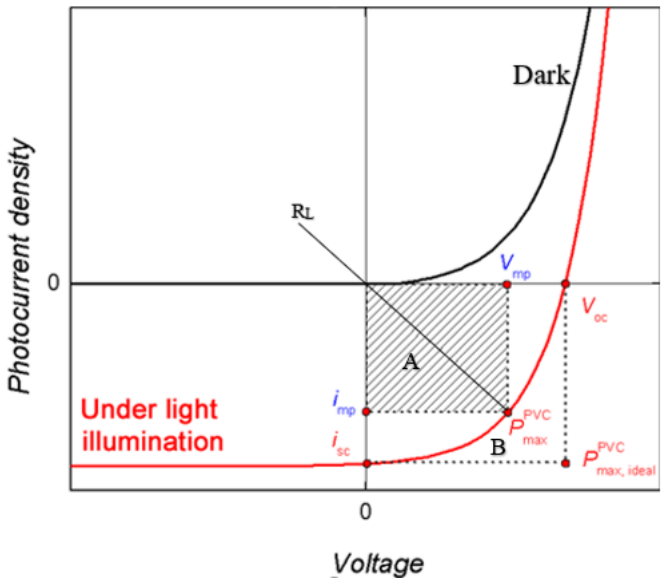

Figure 4: Typical solar cell I-V curve [19].
(Sometimes, current density (J) is reported instead of current allowing a more direct comparison of cell performances whatever the surface area is).

The necessary notations of solar cell current-voltage diagrams are [20]:

- **Short-circuit current density (J_{sc}):** it is defined as the current density produced in a solar cell device when illuminated when R_L =0.
- **Open-circuit voltage (V_{oc}):** It is defined as the voltage at solar cell terminals when no external load is connected (R_L=∞).

$$V_{0c} = \frac{KT}{q}\ln\left(\frac{I_{sc}}{I_0} + I_0\right)$$

- **Fill factor (FF):** The ratio of maximum electrical power that can be supplied to the ultimate virtual maximum power obtained by the product of short-circuit current and open-circuit voltage.

$$\mathrm{FF} = \frac{\mathrm{P_{max}}}{\mathrm{P_{max,ideal}}} = \frac{\mathrm{P_{max}}}{\mathrm{Jsc\ x\ Voc}}$$

- **Power conversion efficiency (PCE) or η:** The power conversion efficiency is defined as the ratio between maximum electrical power generated and the corresponding incident optical power (Pin).

In sake of comparison, P_{in} corresponds to a standard terrestrial solar spectral irradiance distribution denoted as **Air mass 1.5 (AM 1.5):**

$$\mathrm{PCE} = \frac{\mathrm{P_{max}Pm}}{\mathrm{P_{in}}} = \frac{\mathrm{Jsc\ x\ Voc\ x\ FF}}{\mathrm{P_{in}}}$$

- **External Quantum Efficiency (EQE):** It is the number of electrons extracted in an external circuit divided by the number of incident photons under short circuit conditions. It can be calculated for the whole AM1.5 spectrum or at a particular wavelength.

$$\boldsymbol{EQE = \frac{Number\ of\ electrons}{Number\ of\ photons} = \frac{J_{sc}(\lambda)/e}{Pin(\lambda)/(\frac{hc}{\lambda})}}$$

where: λ is the wavelength, e the elementary charge, h the Planck constant and c the speed of light in vacuum [20].

Those parametres cover most of the essential properties that we will come across in this study. Shockley–Queisser limit is also a valuable property that must be concerned about, due to its effect on the way of new generation fabrication, including ours.

1.5 Shockley–Queisser limit

Considering single-junction solar cells, the efficiency cannot exceed a maximum value that is known as the Shockley-Queisser limit. It relies on the optimal absorption of the solar spectrum by a semiconductor; this semiconductor being characterized by its bandgap value in a first approach. For silicon, the theoretical limit rounds as 33%, but a practical limit is considered to be 29% [21]. A Carnot heat engine determines the ultimate efficiency limit in the conversion of sunlight energy to electrical energy. This limit is about 94%, based on the high temperature of the sun's black body at 5,800 K and the cell temperature of about 350 K. As mentioned, the Shockley–Queisser limit only applies to

single-junction solar cells; then, multiple junction concepts can outperform this limit. Nevertheless, other criteria mentioned above and, firstly, the production cost can then override this benefit and limit such developments in the industrial market place.

1.6 The development of solar cells

In 1952, new silicon solar cells were reported by Kingsbury and Ohl, using purer silicon to prevent growth junction formation and the ion bombardment of the surface from forming the rectifying junction. Just in two years, Chapin develops a crystal growth technique forming the basis of the first modern silicon cell. This cell has an efficiency of around 6%, but it was the first real prospects for power generation using photovoltaics and a big milestone for this technology. [22, 23]

Although there are many ways to simplify and distinguish different types of solar cells that come after Chapin's attempt, the most used approach to understand their development is to divide them into three categories or, as many references called them, generations. The first and the oldest generation is then obviously structured as a silicon homojunction. The second generation was mainly started when applying thin-film technology to photovoltaics designs. Last, the third generation contains photovoltaics technologies that have the potential to overcome the limitations of the first and second generations with additional properties that were not a concern when the last two were made. Nevertheless, it has to be noticed that, right now, more than 90% of the solar cell market is composed of first-generation devices, the rest being filled by second-generation devices. Third generation devices have no market declination, up to now.

1.6.1 *First-generation*

As mentioned before, the oldest silicon-based solar cell technology is called the 1st generation and is made of bulk silicon. This technology has matured by a lot of research and development because it did not have any other competitors over the first three decades allowing it to be adopted by many research labs and the industrial community. Also, the fact that raw material (SiO_2) - sand in general - is widely available and its

treatment and extraction techniques are well known and in constant progress [24] contribute to maintain the 1st generation as the leading one as today.

In 1954, based on the Chapin's crystal growth technique that was initially developed for transistors and integrated circuits, some researchers at Bell Laboratories were able to announce their first successes concerning crystalline silicon solar cells formed by dopant diffusion into wafers (Fig.5). [25]

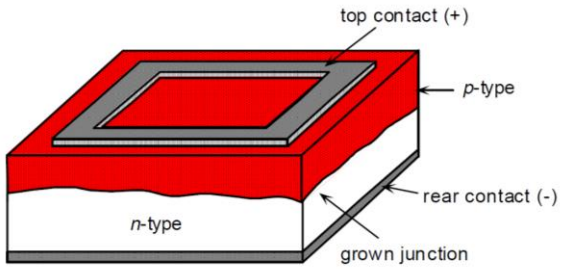

Figure 5: Solar cell design, reported in 1954 [25].

Although at that time, those cells exhibited weak performance such a 6% efficiency and an expensive fabrication cost, there were no competitors, and they did find an immediate use in space segment. Due to the space program race at that era (1955 -1975), the need for an energy source that can be reliable outside the terrestrial atmosphere pushed the development in cell technology such that Hoffman Electronics was able to introduce cells with increased efficiency of 9% in 1958 and 10% in 1959. By the early 1960s, the energy conversion efficiency reached 14% under terrestrial sunlight. [26]

The initial cell design remained unchanged until the early 1970s. Then a new branch of research started adopting thin-film technologies for solar cell fabrication, it was denominated as the 2nd generation. Even if some advantages can be pointed out over the first one, the industrial community did not abandon the first-generation or give up on its development. As a consequence, in 1985, the University of New South Wales, Australia, demonstrated a 1st generation solar cell over 20% efficiency. It was patented in 1992 as a module. [27]

In the 21st century, many companies reached higher values of efficiency for the 1st generation, such as the Amonix company, with 27%, even though it has been noticed some saturation effect and slowdown in efficiency increase slope as this latter was approaching the Schockley-Queisser limit (Fig. 6). It is worth to mention that the

fabrication cost has been continuously decreasing with time owing to the improvement of fabrication processes as well as setting-up of ultra large scale fabrication plants. [27]

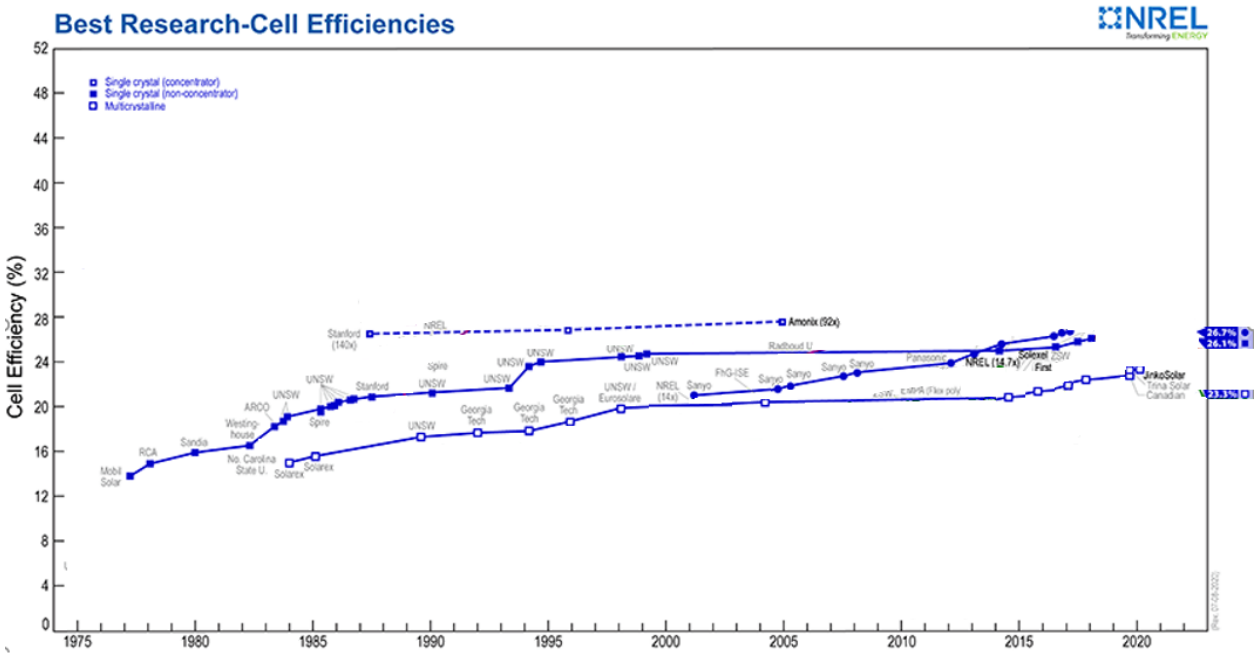

Figure 6: Comparison of 1st generation efficiency with the timeline (NREL).

There are two main classes for 1st generation solar cells, and they correspond to how the Si material is obtained: mono-crystalline (mono c-Si) or poly- (or multi-) crystalline (poly (or multi) c-Si). Those two types of solar cells shared roughly equally the Si solar cell market, currently. The typical cell dimension is identical for both technologies, 156mm x 156mm, that allows getting the same panel integration processes whatever the cell type is.

1.6.1.1 Monocrystalline Silicon solar cell

This type of cell constitutes about 40% of the market for PV technology. The cell dimension is 156 mm pseudo-square (rounded corners) and results from the ingot wafers are cut from. A 8" (200mm) cylindrical monocrystalline ingot is melted in a way leading to a minimal number of impurities at high temperature (around 1420˚C) using the so-called Czochralski method (CZ method). During the crystal growth process of that ingot, doping to about one part per million with boron (for p-type) or phosphorus (for n-type) is made in

order to get the base type of the solar cell. This ingot is diced in wafers of 0.2mm (or even less, now) in thickness. Then boron-doped base wafers have phosphorus diffused at high temperatures, a fraction of a micron into the surface to form the so-called emitter and the resulting p-n junction (the reverse process is made for n-type base wafers, i.e., boron is diffused to create the emitter that is p-type in that case). Electrodes contacts to both the n-Si and the p-Si sides of the junction are formed by screen printing a metal paste (most commonly silver based) that is then diffused at high temperature into the Si through the passivation/anti-reflection coating layers. The formed solar cell has J_{sc} and V_{oc} value, respectively, around 35 mA/cm^2 and over 0.6V for best cells. The maximum efficiency of such cells has reached 24.7%. The used melting process in the fabrication of the Si ingot cell is high energy and time consuming, which leads to high production costs. A lot of research and development is done at industrial level trying to improve the fabrication process to overcome this point. [28]

Due to the silicon material, the efficiency enhancement was limited by the amount of energy produced by the photons since it decreases at higher wavelengths. Moreover, illumination with lower wavelengths leads to thermal dissipation and mainly causes the cell to heat up hence increasing the internal resistance and speeding the recombination processes leading to a reduction in its efficiency. More limiting factors such as solar radiation reflected by the electrode contacts on the top side, electrode resistance, and surface recombination are sources of generated energy losses.

1.6.1.2 Multicrystalline silicon solar cell

The attempts of the industry to drive the research on crystalline Si in a way that reduces costs and increases production have led to the development of multi-crystalline silicon based solar cells. They are very similar to monocrystalline cells in terms of theoretical concepts, but the fabrication process of wafers is the main difference.

Multi-Si material is fabricated from pure molten Si (that can be tailings from Si microelectronic industry or photovoltaic kerf) in a square shape tank. The cooling down (solidifying) is an essential step because it determines the grain size and the distribution

of impurities. Historically it has been firstly developed by a company called Evergreen Solar. [29, 30]

Over time, this technology became more attractive because its manufacturing is lower in cost and the corresponding cells are only slightly less efficient compared to mono-Si. Currently, the efficiency difference between mono- and multi-Si cells (and modules) is around 4%. [31]

For the time being, there is only a minor difference when comparing multi-Si and mono-Si solar cells regarding performance, efficiency, and costs; on the other hand, other merits are often very similar such as lifetime. One particular advantage concerns the module design where the square shape of multi-Si wafers, instead of the “pseudo-square” shape of mono-Si wafers, eases their arrangement in modules that are made without dead spaces. Nevertheless, in the next few years, mono-Si and multi-Si cells are planned to share the market equally.

1.6.2 *Second generation*

The second-generation of solar cells mainly emerged with thin-film fabrication technology. The driving idea was to furnish a solution towards reducing the used energy and raw material consumption, and so price during fabrication. The first considerations concerning thinner silicon films for solar cells were referred to Wolf and Lofersky in the 70s while they were looking for the ideal parameters achieving high-efficiency solar cells. They pointed out the relation between the geometry factor - mainly cell thickness - and the energy generated [26, 32]. In their work, they concluded the benefits introduced by thin-film materials of a thickness - around 30 μm - such as low surface recombination velocities and good optical confinement. After these results, it took more than a decade to get an increase in research interest from other laboratories. In 1980, the University of Delaware demonstrated a thin-film solar cell exceeding 10% efficiency using copper sulfide and cadmium sulfide. Since that date, several materials were investigated, and the research was to balance the grain size and conversion efficiency (Fig. 7). [33]

There are many ways to classify and to categorize the branches of this generation. Some references assigned them based on the substrate material maximum allowed temperature during processing [35, 36] and, therefore, fit into one of these three categories:

- High-temperature approach (melting point depending on the material used).
- Low-temperature approach (room temperature).
- Transfer techniques.

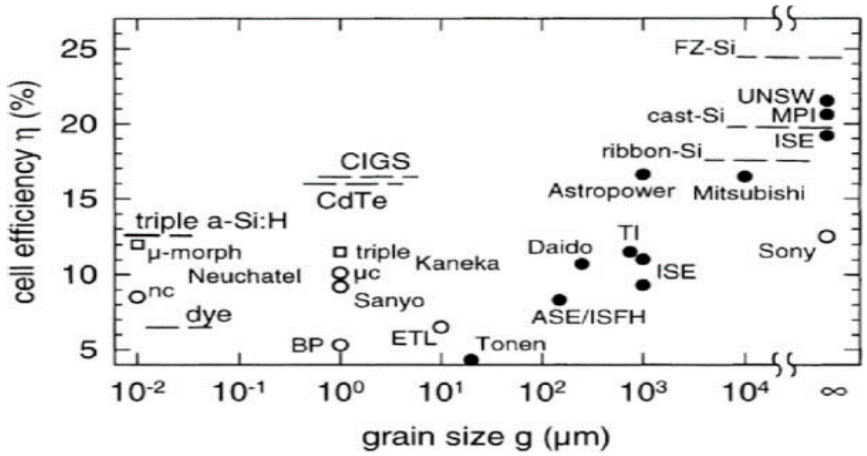

Figure 7: Thin-film solar cell efficiency as a function of the material grain size [34].

It may also be classified by the deposition technology used, such as:

- Chemical Vapor Deposition (CVD).
- Plasma Vapor Deposition (PVD).
- Pulsed Laser Deposition (PLD).
- Atomic Layer Deposition (ALD)

There is not too much data about the economic aspects of the different deposition methods in large-scale industrial production of those solar cells, but there is a trend towards CVD owing to the potential for continuous inline processing and achieved deposition rates of more than 5 μm/min.

However, the most common way to classify this generation is by the used materials, such as amorphous silicon (a-Si), cadmium telluride (CdTe) and copper indium gallium selenide (CIGS), because it may contain overlap between the technologies and substrates but not the materials.

Apart from the reduction of material needs that this solar cell technology brings as improvement, the processes are usable with large surfaces that are either flexible or rigid substrates. So except for some particular designs, those cells do not adopt the 156mm cell size of 1st generation.

1.6.2.1 Amorphous-Si solar cell

In 1973, the first fabrication of non-crystalline silicon materials, commonly referred to as amorphous silicon (a-Si), emerged. The silicon atoms are randomly located from each other compared to other crystalline silicon structures, as shown in Fig. 8.

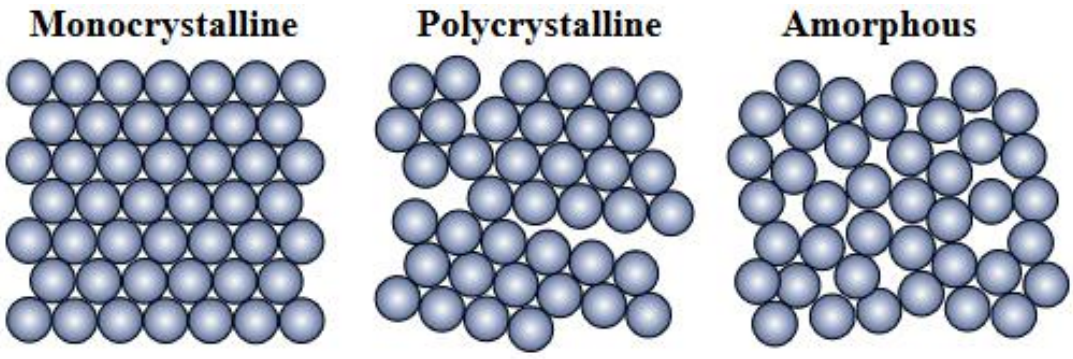

Figure 8: Illustration of, mono- and multi-, crystalline silicon and amorphous silicon structures.

It has been noted early in the 70s while using the glow discharge process in silane (SiH_4) gas that the a-Si layer had unusually good electronic properties. [37] This note led Spear and LeComber laying out that those properties could be increased enormously either by mixing some phosphine (PH_3) gas - becoming an n-type layer - or some diborane (B_2H_6) gas - becoming p-type layer – launching the idea of creating an a-Si solar cell. [38]

In 1976, Carlson and Wronski, RCA Laboratories, fabricated first a-Si photovoltaic cells consisting of a single sequence of p-i-n layers, using the vapor-deposition process. The concept was based on the introduction of an intrinsic or undoped layer (i-layer) between p-and n-type layers. The whole i-layer acts as an active layer in which the requested electric field for the photogeneration process is slowly decreasing. [39]

A well-known drawback of a-Si solar cells is the significant degradation in their power output when exposed to the sunlight almost in the range of 15-35%. That can be improved using thinner layers. However, light absorption will be reduced as well as cell conversion efficiency. So it is balancing between stability and efficiency (Fig. 9).

Some designs consist of a double or triple-junction, raising the efficiency to 8–10%. Other designs focused on the material enhancement itself such that amorphous silicon carbide (a-SiC), amorphous silicon germanium (a-SiGe), amorphous silicon nitride (a-SiN) and hydrogenated amorphous silicon (a-Si:H).

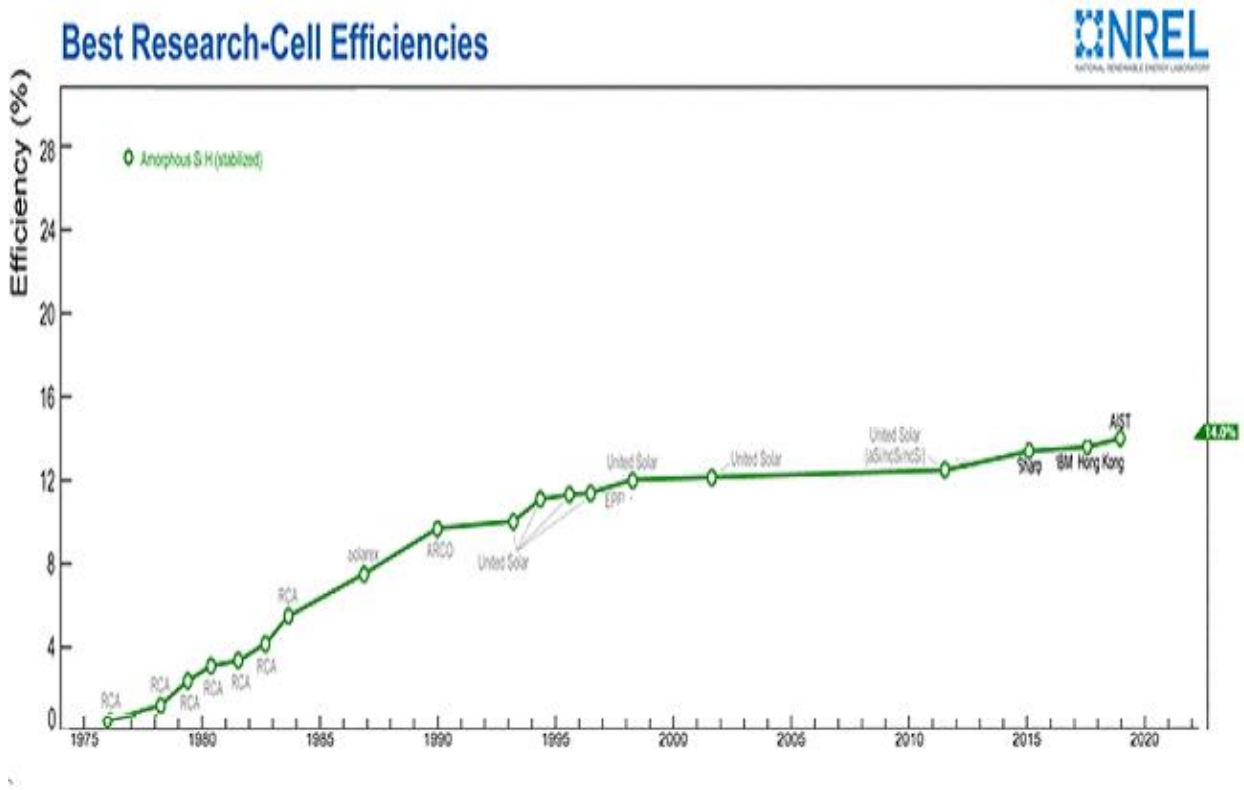

Figure 9: Amorphous silicon solar cell efficiency (NREL).

1.6.2.2 CdTe thin-film solar cells

Research in cadmium telluride (CdTe) material was started back in 1954. Owing to its optimum bandgap of 1.45eV, it exhibits a high optical absorption coefficient. A variety of fabrication methods based on stable raw materials made it one of the best choices for

such applications [40, 41] (at that time, environmental concerns were not raised). However, due to the obstacles such as finding the right structure obtaining low-resistance contacts to p-type CdTe, decreasing the recombination losses associated with the junction interface, and the difficulty of doping p-type CdTe during fabrication, CdTe solar cells did not develop as fast as their silicon counterparts.

Nevertheless, similarly to silicon, cadmium telluride went through many stages of development/improvement; the first attempts have been made with a single crystal at the RCA Labs with 2.1% conversion efficiency. At the same time in the USSR, CdTe solar cells reached efficiencies of even 4%. The borderline of 10% efficiency was crossed in 1982, obtained in Kodak labs using a CdTe heterojunction solar cell. [42] In the end, it finds its rightful place using thin-film technologies.

In 1992, the National Renewable Laboratory at the University of South Florida developed a 15.9% efficient thin-film photovoltaic cell made of CdTe breaking the 15% barrier for the first time for this thin-film technology. Furthermore, it was combined with a robust structure and a high production throughput, which both accelerated the development of CdTe thin-film cells. These cells have gone through a faster track of development in recent years, due to their competitiveness regarding cost, high conversion efficiency, and the available manufacturing processes.

The fabrication of the CdTe solar cells starts in a focused composition of the vapor above a substrate with a temperature of some hundred degrees Celsius. The high self-stabilizing material can be deposited at a very high rate of more than 1 μm/min at substrate temperatures of 450–600 ^{o}C. Owing to the performance tolerance to material defects and grain boundaries, simple processes such as electrodeposition and screen printing are possible. These processes are a good prerequisite for large-scale production. [43]

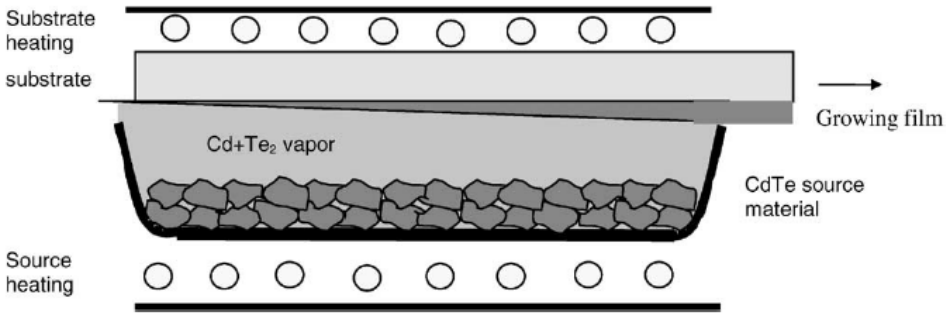

Figure 10: Schematic view of reactor for continuous deposition of CdTe by close-spaced sublimation [33].

The highest efficiencies are obtained with a process called close-spaced sublimation (CSS), a modified evaporation process, where substrates and sources are very close together with a relatively small difference in temperature so that the film growth occurs close to an equilibrium condition as shown in Fig. 10. Nowadays, industrial CdTe solar cell efficiency reaches 16.5% [33] as research cell one exceeds 20% (Fig. 11).

For those reasons, it is not overstating to say that CdTe is leading the thin-film solar cell technology for the time being even if, from recent years, environmental concerns question its use, whatever it concerns the fabrication or the deployment. The use of cadmium - toxic material - requires special attention during the production of the cells as well as the recycling phase at the end of their lifetime.

In order to discard the toxicity from solar cell production, the door opened to other thin-film materials to be investigated, such as the CIGS thin-film cell.

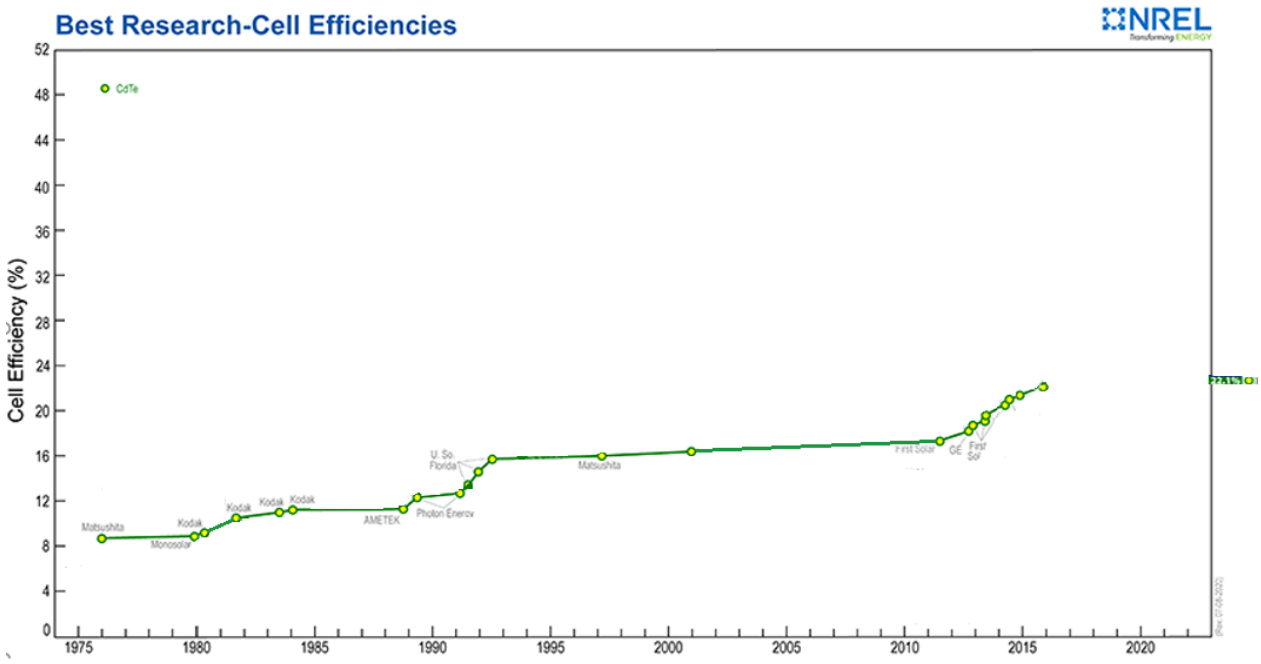

Figure 11: CdTe thin-film cell efficiency (NREL).

1.6.2.3 CIGS thin-film solar cell

This material line was first developed using ternary compound semiconductors such as $CuGaSe_2$, or $CuInS_2$ referred to as CGS or CIS solar cell. The first functional single crystal that worked was auspicious but was not wise because of the complexity of the material combination comparing to other thin-film technology. [44] It became evident that the CIS process technology could be a reasonable alternative when the pioneering work of Kazmerski showed immediate success using controllable and reproducible process conditions. [45] Establishing a well-controlled system for multisource co-evaporation by Boeing made then the CIS cell soon the front-runner concerning thin-film solar cell efficiencies. In the 80s, a fabrication technology for CIS solar cell adapted the thin-film processing developed by ARCO Solar, namely sputtering of metal films with a subsequent selenization (selenization and/or sulfurization (SAS) are the processes whereby a surface of a material is exposed to a selenium and/or sulfur-containing atmosphere at high temperature step [46]).

In those developments, the addition of Ga and S helped to increase efficiency, and a follow-up material line based on the quaternary compound CIGS emerged where S can

either be Se or S. This thin-film solar cell technology is the most promising one compared to other thin-film cells at that time. Their conversion efficiency is close to the conversion efficiency of multi-Si cells (Fig. 12).

The fabrication of such a cell is commonly made on glass or metal foil for flexible panels. It starts with a molybdenum layer, followed by a layer of an alloy of Cu (In, Ga) Se2 (di-selenide of copper, indium, and gallium), which is the photon absorber layer. This layer thickness is about two micrometers, and it is usually produced by co-evaporation of metallic materials under a high vacuum, which is followed by a selenisation step at a substrate temperature around 600°C. The substitution of In by Ga permits the adjustment of the energy gap (in between 1eV to 1.7eV) [47]. Then, an n-type buffer layer of CdS with a thickness of about 50nm is added. It helps to optimize the interface between the CIGS-absorber, the non-doped i-ZnO layer, and the n-type top window and contact layer (ZnO:Al). [47]

For now, producing CIGS solar panels at prices that can compete with silicon or cadmium telluride panels has not been possible. Moreover, concerns about In and Ga resources, and so their price in the medium/long term, impede the development of the technology for standard PV generation considering, moreover, that silicon technology cost is always decreasing.

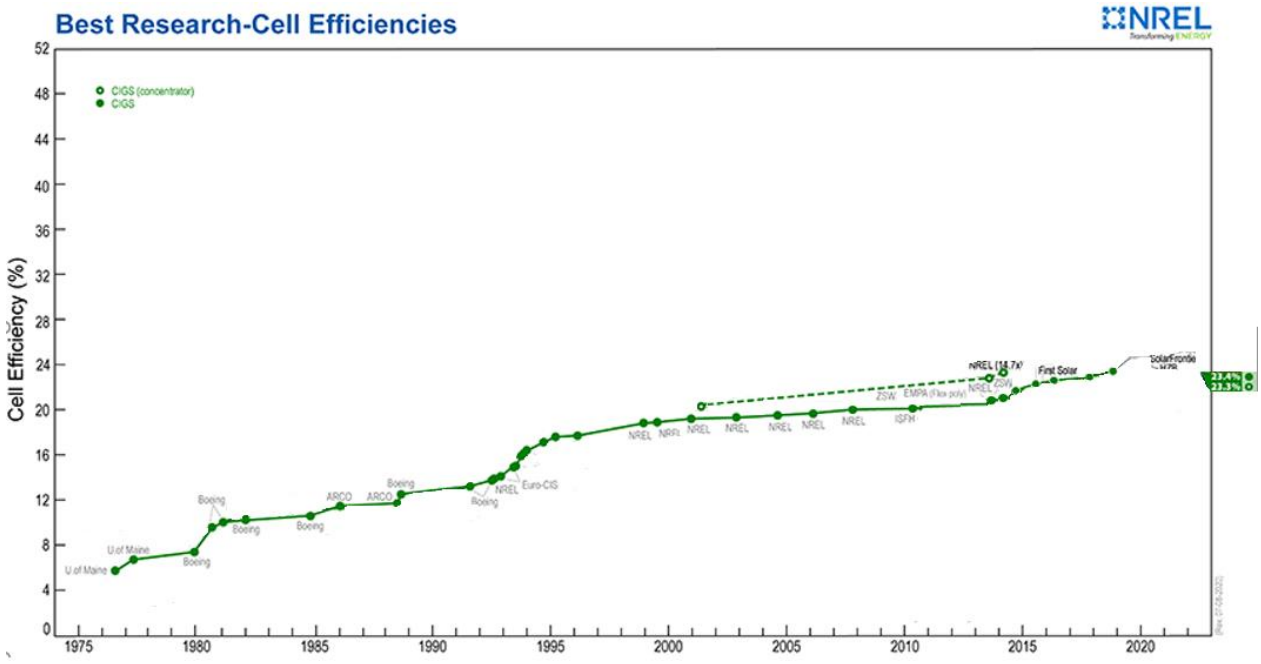

Figure 12: CIGS solar cell efficiency with the timeline (NREL).

1.6.3 *Third-generation*

Right now, silicon technologies represent close to 90% of market share, the other part being constituted of thin-film technologies (CdTe and CIGS). All technologies present an efficiency close to or even higher than 20% at an industrial level. Simultaneously, since a couple of decades, a considerable research effort is placed on new materials and novel concepts for photovoltaic modules trying to create a considerable gap either in fabrication cost or in the efficiency by reducing the needs in raw materials, in processing needs or by improving mainly the photon conversion. Those solar cells granted the name of the third generation, and numerous variations exist under multi-junction solar cells, organic solar cells [4], dye-sensitized solar cells (DSSC), as shown in Fig. 13.

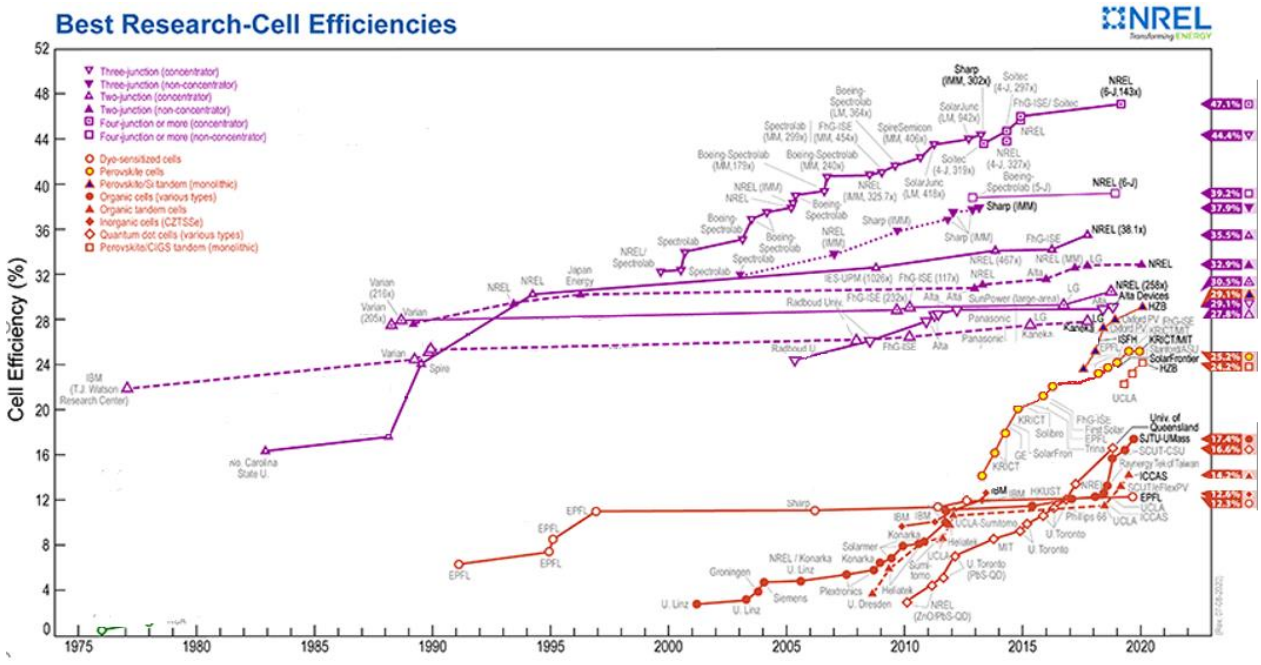

Figure 13: Comparison of the efficiency of some 3rd generation solar cell concepts with the timeline (NREL).

1.6.3.1 Multi-Junction Solar Cell

Multi-junction (MJ) solar cells, from their name, are composed of multiple p–n junctions made of different semiconductor materials. Each p-n junction produces an electric current

in response to a particular portion of the solar light spectrum. The use of multiple stacked semiconducting materials with different bandgap allows fitting the absorbance more closely to the solar spectrum, improving the overall cell efficiency.

The efficiency of traditional single-junction cells cannot exceed the theoretical limit (Shockley–Queisser) of 34%. Theoretically, an infinite number of junctions would exhibit a maximum efficiency value of 86.8% under highly concentrated sunlight. [48]

Currently, multi-junction cells have demonstrated the performance of over 43%. [49] On the other hand, this efficiency gained at the cost of increased complexity and manufacturing price. To date, their higher price to performance ratio has limited their use to particular roles, especially in aerospace, where their high power/weight ratio is a necessary aspect. In terrestrial applications, these solar cells have been suggested for use in concentrated photovoltaics (CPV) systems, with numerous small test sites around the world.

1.6.3.2 Organic Solar Cell

The intrinsic organic solar cell consists of two layers: one electron donor and one electron acceptor layer. The moment a photon is absorbed, it creates a bound electron-hole pair (also called exciton), mostly in the donor material. It can be separated when the exciton diffuses to the donor-acceptor interface.

The material used for the production of organic solar cells is composed of polymers or, in other words: plastic. The plastic used has low production costs in high volumes, which represents the main advantage of organic solar cells. Also, the optical absorption coefficient of organic molecules is high, so a large amount of light can be absorbed with a small volume of material. The principal disadvantages are low efficiency, low stability, and low strength compared to inorganic photovoltaic cells. Research and development of organic photovoltaic technologies have delivered a device record efficiency of 16% [50]. However, a few years of a lifetime are still required before organic photovoltaic modules can effectively be launched into, undoubtedly, specific market parts.

1.6.3.3 Dye-sensitized solar cells (DSSCs)

O'regan and Grätzel introduced a new class of photovoltaic devices in the early 90s by manufacturing a working solar cell based on dye-sensitized material (DSSC) [51]. A schematic diagram of DSSCs is presented in Fig. 14.

DSSCs are based on a semiconductor formed between a photo-sensitized anode and an electrolyte. The advantages of Grätzel model solar cells can be summarized as follows:

- low cost in manufacturing
- possible roll-to-roll processing allowing high volume (and flexible substrate) production
- energy payback less than one year owing to the low embodied energy in the manufacturing process
- most often composed of non-toxic, earth-abundant materials (except Pt, Ru) that perform well in diverse light conditions such as a high angle of incidence
- lightweight, flexible, and semi-transparency capabilities.

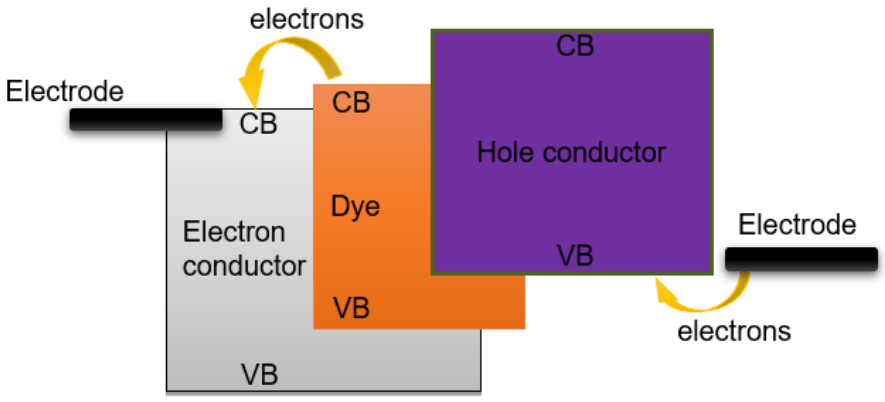

Figure 14: Schematic diagram of DSSCs [52].

1.6.3.4 Quantum Dot Sensitized Solar Cells (QDSSCs)

Let us start by defining first the concept of a Quantum Dot (QD) since one part of my work will be based on it. They are 3D semiconductor nanostructures which diameter is in the

range of 2 to 10 nanometers in which carriers are strongly confined. The number of charges is finite, and they are located in discrete energy levels.

At the beginning of the 1960s, the quantum dot concept has been suggested as a new structure of semiconductor materials. Twenty years later, Ekimove noticed and published about the existence of semiconductor crystallites in a glass matrix [53] and opened the door for corresponding research. A few years later, L. Brus developed a model of spherical quantum dots based on the effective mass model. [54] However, it was until the 90s to have a successful growth of quantum film by depositing 3D silver islands on gallium arsenide substrate [55]. At the beginning of this millennium, a research group at Los Alamos demonstrated a quantum dot capable of producing up to three electrons per photon [56]. Nowadays, quantum dots are promising nanostructured materials in photonics and biomedical applications. The theoretical conversion efficiency for solar cells up to 44% is expected as well as the simplicity in manufacturing and the capacity to realize light harvesting in a broad solar spectrum region. A schematic diagram of QDSSCs is presented in Fig. 15. It only differs from the one of DSSC in the photoactive layer composition.

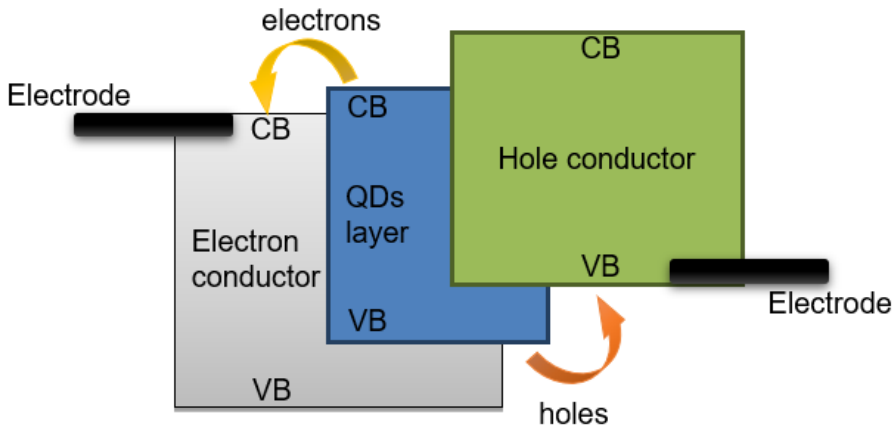

Figure 15: Schematic diagram of a QDSSC [52].

1.7 Solar Cells Comparing Conversion Efficiency

For now, the state of the art conversion efficiency of solar cells is summarized below, as shown in Fig.16:

- 27 % for mono-crystalline Si cells.
- 21 % for multi-crystalline Si cells.
- 22 % for CdTe thin-film cells.
- 23 % for CIGS thin-film cells.
- 29 % for organic-inorganic perovskite cells.
- 47 % for Multijunction cells.

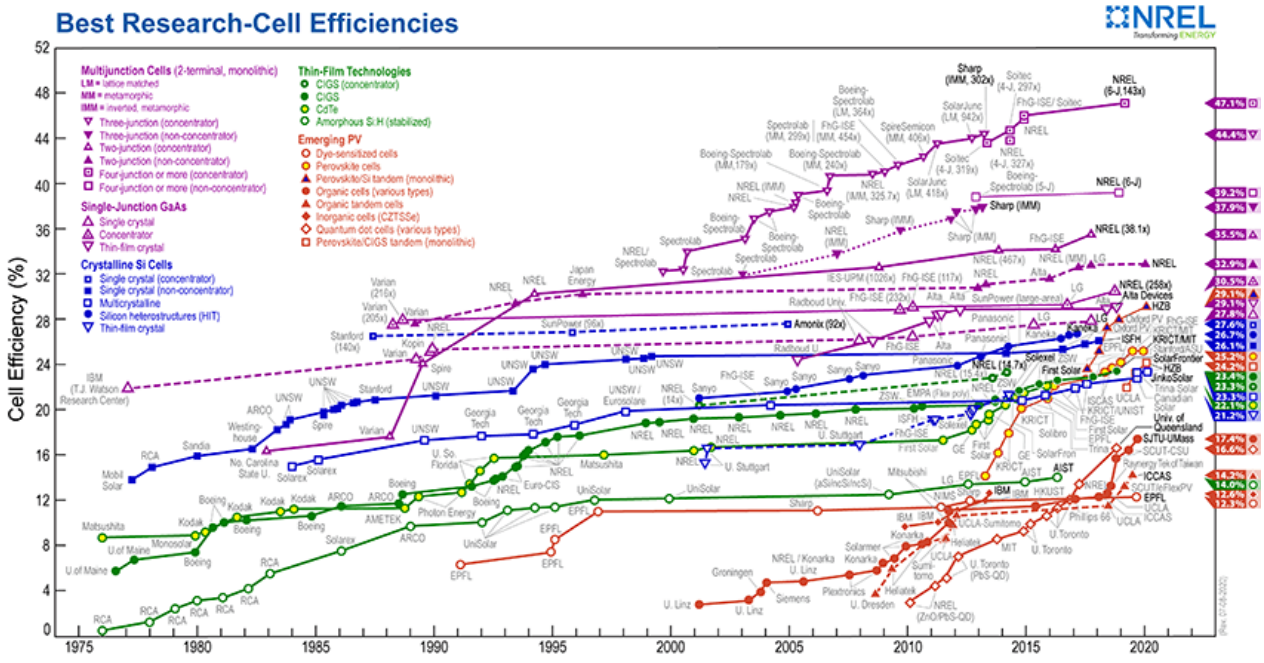

Figure 16: State of the art conversion efficiency of research solar cells (NREL).

The graph (Fig. 17) represents photovoltaic technology status and prospects until 2030. At the time this graph was issued, the contribution from emerging technologies and novel concepts from third-generation photovoltaics was projected to start almost nowadays. Currently, this projection has been shaken due to silicon industry (1st generation) development and technical, even scientific, concerns for 3rd generation industrial deployment.

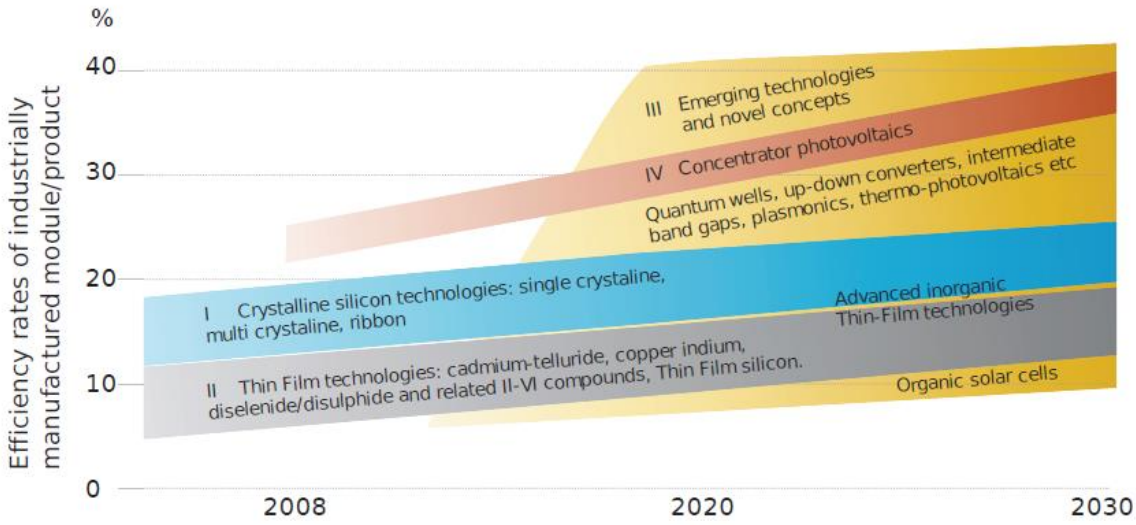

Figure 17: Photovoltaic technology status with time [57].

1.8 Conclusion

In this chapter, we set the scene for this work. My work will be focused on 3rd generation cells, and more particularly, my ultimate objective is to develop a flexible solar cell with a quantum structure that is not primarily dedicated to compete with silicon but to offer some new opportunities, including PV power into applications. Since the scope can be vast, we will impose against ourselves some constraints that are mainly looking forward to develop eco-green and affordable technologies, and they are:

- low-cost raw materials
- nontoxic materials
- nontoxic processes for fabrication
- targeting long life duration under high temperature and humid environment: by working with solid-state solar cells (contrary to organic or hybrid solutions that are alternatively studied)
- bearing in mind that flexible structuration is a real asset towards current bulk Si or thin films even if lower efficiencies are obtained Attempting reaching efficiency around 10 %: by optimizing the synthesis and the properties of quantum dots as an absorber layer

1.9 Structure of this manuscript

After reviewing the basic concepts, operation principles, properties, historical development timeline for solar cells, and the motivation for our targeted quantum dot solar cells (this chapter), chapter 2 will introduce quantum structure solar cells and describe the design of flexible Quantum Dots Sensitized Solar Cells by the planed materials and their functionality.

Then, chapter 3 includes an explanation of all experimental techniques used during this work and continues on the different approaches of material fabrication: first, the production of quantum dot structures, second the deposition of thin-film layers of the same materials. After that, the entire solar cell device fabrication processes will be described as well as an investigation on the effect of QDs layer thickness/absorption on device performance.

Essential characterization techniques such as atomic force microscopy, photoluminescence, and electroluminescence are described in chapter 4. Another device testing/analysis techniques such as I-V characterization, Hall effect measurement are also briefly explained in the same chapter.

At the end of the thesis, are presented the conclusion from whole work and some guidelines for future developments and paths.

References

1. Hallosserie, A., et al., *Biodiversity Issues Should Be Better Taken into Account in the Energy Transition*, in *Handbook of Climate Change and Biodiversity*. 2019, Springer. p. 45-59.
2. Kamran, M., et al., *Solar photovoltaic grid parity: a review of issues, challenges and status of different PV markets.* International Journal of Renewable Energy Research (IJRER), 2019. **9**(1): p. 244-260.
3. Cain, F. *How Long Will Life Survive on Earth?* 23 Dec , 2015 [cited 2016. 07/March]; Available from: http://www.universetoday.com/25367/how-long-will-life-survive-on-earth/.
4. Grätzel, M., *Photoelectrochemical cells.* Nature, 2001. 414(6861): p. 338-344.
5. Bhushan, C., A. Kumarankandath, and N. Goswami, *The state of concentrated solar power in India: A roadmap to developing solar thermal technologies in India.* New Delhi: Centre for Science and Environment, 2015.
6. Green, M.A., *Photovoltaic principles.* Physica E: Low-dimensional Systems and Nanostructures, 2002. 14(1): p. 11-17.
7. Adams, W.G. and R. Day, *The Action of Light on Selenium.* Proceedings of the Royal Society of London, 1876. 25(171-178): p. 113-117.
8. Fritts, C.E., *On a new form of selenium cell, and some electrical discoveries made by its use.* American Journal of Science, 1883(156): p. 465-472.
9. Grondahl, L.O., *The copper-cuprous-oxide rectifier and photoelectric cell.* Reviews of Modern Physics, 1933. 5(2): p. 141.
10. Green, M.A. *Photovoltaics: coming of age*. in *Photovoltaic Specialists Conference, 1990., Conference Record of the Twenty First IEEE*. 1990. IEEE.
11. Ohl, R.S., *Light-sensitive electric device including silicon*. 1948, Google Patents.
12. Palz, W., *Photovoltaic power generation: a 1987 review.* International journal of solar energy, 1987. 5(5-6): p. 289-310.
13. Sproul, A., *Understanding the pn Junction.* Solar Cells: Resources for the Secondary Science Teacher, 2003: p. 13-24.
14. Prince, M. and M. Wolf, *New developments in silicon photovoltaic devices.* Journal of the British Institution of Radio Engineers, 1958. 18(10): p. 583-594.
15. Lindholm, F.A., J.G. Fossum, and E.L. Burgess, *Application of the superposition principle to solar-cell analysis.* IEEE Transactions on Electron Devices, 1979. 26(3): p. 165-171.
16. Gledhill, S.E., B. Scott, and B.A. Gregg, *Organic and nano-structured composite photovoltaics: An overview.* Journal of Materials Research, 2005. 20(12): p. 3167-3179.
17. Günes, S., et al., *Hybrid solar cells using PbS nanoparticles.* Solar Energy Materials and Solar Cells, 2007. 91(5): p. 420-423.
18. Thompson, B.C. and J.M. Fréchet, *Polymer–fullerene composite solar cells.* Angewandte chemie international edition, 2008. 47(1): p. 58-77.
19. Photovoltaics, O., *C. Brabec, V. Dyakonov and U. Scherf*. 2008, Wiley-VCH, Weinheim.
20. Sargent, E.H., *Infrared photovoltaics made by solution processing.* Nature Photonics, 2009. 3(6): p. 325.
21. Graetzel, M., et al., *Materials interface engineering for solution-processed photovoltaics.* Nature, 2012. 488(7411): p. 304.
22. Kingsbury, E.F. and R.S. Ohl, *Photoelectric properties of ionically bombarded silicon.* Bell System Technical Journal, 1952. 31(4): p. 802-815.
23. Chapin, D.M., C. Fuller, and G. Pearson, *A new silicon p-n junction photocell for converting solar radiation into electrical power.* Journal of Applied Physics, 1954. 25(5): p. 676-677.
24. Green, M.A., *Third generation photovoltaics: solar cells for 2020 and beyond.* Physica E: Low-dimensional Systems and Nanostructures, 2002. 14(1-2): p. 65-70.

25. Green, M.A., *Silicon solar cells: advanced principles & practice*. 1995: Centre for photovoltaic devices and systems, University of New South Wales.
26. Wolf, M., *Historical development of solar cells*. 1976: IEEE Press, Piscataway.
27. Amin, N., et al., *Solar photovoltaic technologies: from inception toward the most reliable energy resource.* Encyclopedia of sustainable technologies. Elsevier, Amsterdam, 2017: p. 11-26.
28. El Chaar, L. and N. El Zein, *Review of photovoltaic technologies.* Renewable and sustainable energy reviews, 2011. 15(5): p. 2165-2175.
29. Schmidt, J., A.G. Aberle, and R. Hezel. *Investigation of carrier lifetime instabilities in Cz-grown silicon*. in *Photovoltaic Specialists Conference, 1997., Conference Record of the Twenty-Sixth IEEE*. 1997. IEEE.
30. *Evergreen Solar.*
31. Battersby, S., *News Feature: The solar cell of the future.* Proceedings of the National Academy of Sciences, 2019. 116(1): p. 7-10.
32. Spitzer, M., et al. *Ultra high efficiency thin silicon pn junction solar cells using reflecting surfaces*. in *14th Photovoltaic Specialists Conference*. 1980.
33. Mosseri, R., *L'énergie à découvert*. 2017: CNRS Éditions via OpenEdition.
34. Bergmann, R., *Crystalline Si thin-film solar cells: a review.* Applied physics A, 1999. 69(2): p. 187-194.
35. Hebling, C., et al., *The crystalline silicon thin-film solar cell—The high temperature approach*, in *Advances in Solid State Physics 38*. 1999, Springer. p. 607-622.
36. Werner, J.H., S. Kolodinski, and H.J. Queisser, *Novel optimization principles and efficiency limits for semiconductor solar cells.* Physical review letters, 1994. 72(24): p. 3851.
37. Chittick, R., et al., *Thetrahedrally bounded amorphous semiconductors.* Sous la direction de, 1985: p. 1.
38. Spear, W. and P. Le Comber, *Substitutional doping of amorphous silicon.* Solid state communications, 1975. 17(9): p. 1193-1196.
39. Wyrsch, N., et al., *Transport properties of compensated μc-Si: H.* MRS Online Proceedings Library Archive, 1996. 420.
40. Meyers, P.V., *Design of a thin film CdTe solar cell.* Solar cells, 1988. 23(1-2): p. 59-67.
41. Jenny, D.A. and R.H. Bube, *Semiconducting cadmium telluride.* Physical Review, 1954. 96(5): p. 1190.
42. Tyan, Y.-S. and E. Perez-Albuerne. *Efficient thin-film CdS/CdTe solar cells*. in *16th Photovoltaic Specialists Conference*. 1982.
43. Goetzberger, A. and V.U. Hoffmann, *Photovoltaic solar energy generation*. Vol. 112. 2005: Springer Science & Business Media.
44. Wagner, *CuInSe2/CdS heterojunction photovoltaic detectors.* Applied Physics Letters, 1974. 25(8): p. 434-435.
45. Kazmerski, L., F. White, and G. Morgan, *Thin-film CuInSe2/CdS heterojunction solar cells.* Applied Physics Letters, 1976. 29(4): p. 268-270.
46. K.C. Mitchell, E.J.E., D. Pier, *Proceedings of the Conference Record on 20th IEEE Photovoltaic Specialists.* IEEE Press, Piscataway, , 1988(Conference, Las Vegas,): p., p. 1384.
47. Zimmer, T., *6. Photovoltaic cell types.*
48. Green, M.A., *Third generation photovoltaics: advanced solar energy conversion.* Physics Today, 2004. 57(12): p. 71-72.
49. Brown, N., Solar junction breaks concentrated solar world record with 43.5% efficiency. CleanTechnica. com, 2011.
50. Hong, L., et al., *Eco-compatible solvent-processed organic photovoltaic cells with over 16% efficiency.* Advanced materials, 2019. **31**(39): p. 1903441.
51. O'regan, B. and M. Grätzel, *A low-cost, high-efficiency solar cell based on dye-sensitized colloidal TiO2 films.* nature, 1991. 353(6346): p. 737.

52. Serban, B.-C., et al., *Quantum Dots versus Dyes in Sensitized Solar Cells: Synthesis, Optimization, Performance.*
53. Ekimov, A.I. and A.A. Onushchenko, *Quantum size effect in three-dimensional microscopic semiconductor crystals.* Jetp Lett, 1981. 34(6): p. 345-349.
54. Brus, L., *Electronic wave functions in semiconductor clusters: experiment and theory.* The Journal of Physical Chemistry, 1986. 90(12): p. 2555-2560.
55. Smith, A.R., et al., *Formation of atomically flat silver films on GaAs with a" silver mean" quasi periodicity.* Science, 1996. 273(5272): p. 226-228.
56. Schaller, R.D. and V.I. Klimov, *High efficiency carrier multiplication in PbSe nanocrystals: implications for solar energy conversion.* Physical review letters, 2004. 92(18): p. 186601.
57. Frankl, P., et al., *International energy agency technology roadmap: solar photovoltaic energy*. 2010.

Chapter 2

Literature review

2.1 Designing a Quantum Dot-sensitized Solar Cell

Based on what has been introduced in chapter one, it is now established that in designing a solar cell, some constraints and principles should be followed, such as

1. to implement an active layer arrangement as the p-n junction in Si solar cells or a particular element that provide the same functionality in order the photovoltaic effect takes place,
2. to allow the generated photocarriers (electron-hole pairs) to be attracted and transferred before any recombination process happens due to the Coulomb attraction [1],
3. to collect the build-up voltage difference between the two sides of the transfer materials using electrodes, with low resistance and reducing shadow effect from the illuminated electrode,
4. to ensure the right energy scheme to the generated photocarriers in order they transfer to the electrodes with fewest recombination sources as possible; in other words, to design the right energy level (E_C and E_V) that each layer has to present to the next one,
5. to target eco-green materials and processes as well as low prospective cost.

Our suggested design that is based on a Quantum Dot Sensitized Solar Cell (QDSSC) structure can be stated into three layers relative to their assigned duty in the solar cell:

- a charge generation layer (Quantum Dot layer)
- a charge transport layer (Metal Oxide layer)
- charge collection layers (back and top electrodes)

Therefore, this chapter will start with a description of each of those layers starting from the proposed charge generation layer, where the photon absorption happens. Next, we will describe the charge transport layer, where the carriers (electron-hole pairs) are shifted away from each other to prevent recombination. Finally, we will address the last layers, which are the electrodes or collection layers.
The corresponding energy diagram for the whole design will conclude this part.

2.2 Charge generation (QDs) layer

Let us start our design by the charge generation layer since it is the heart of our solar cell. Our design will move away from bulk layers and their limitation by reaching out to nanostructured materials. Such structures, including quantum wells “2D”, nanowires or nanotubes “1D” and quantum dots “0D”. They present a higher potential to improve the efficiencies of solar cells by improving the photon absorption process [2-4].

By reduced material dimension and going to the quantum level of lattice, it has been noted that the density of states (DOS) - the number of different states at a particular energy level that electrons are allowed to occupy - responds by having discrete energy levels and starts to lose its continuous function of energy.

When a material has dimensions small enough (10nm or less) to affect its electronic density of states, as illustrated in (Fig. 18), the material presents a confined density of states. Accordingly, one of the advantages of using such quantum-confined materials is that the electron-hole pairs can be confined in a quantum structure (well, wire, or dot), leading to an increase in carrier density at energies near the band edge and an higher thermal stability.
This scheme is highly considered for high-performance optoelectronic devices, including solar cells, the QDs structure materials have been promising owing to their:

- size-dependent bandgap
- the high molar extinction coefficient
- solution processability
- large dipole moments
- photostability
- high optical absorption coefficients

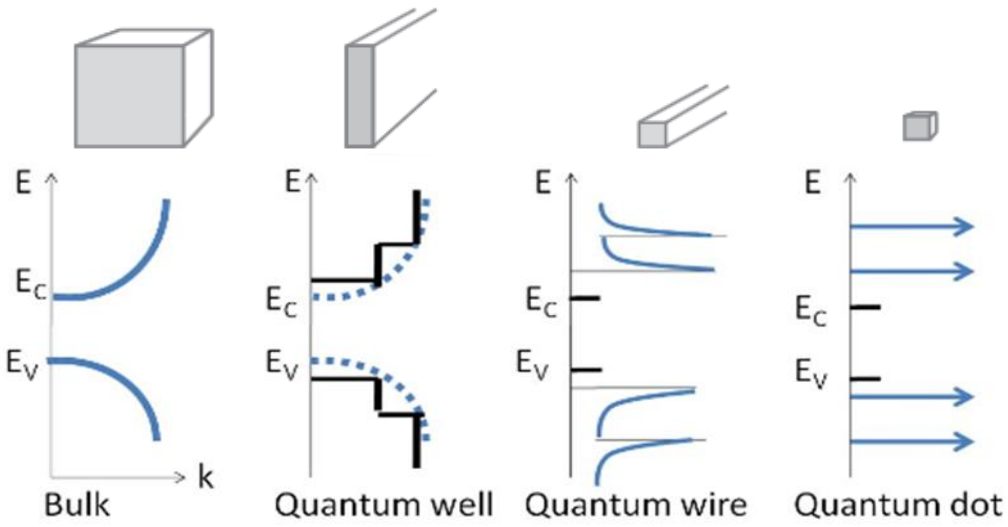

Figure 18: Schematic view of the repartition of the density of states for a semiconductor in different dimensional structures [5].

Moreover, there is a strong relationship between the confined energy and the size of the material quantum dots when this latter is smaller than its Bohr exciton radius, which is defined as the minimum natural separation between electrons in the conduction band and their corresponding holes in the valence band (Table I). On the other hand, weak confinement occurs when the size is 2 to 4 times higher than the Bohr exciton radius.

Table I: Bohr exciton radius to bandgap [6-8].

Material	Bandgap (eV)	Bohr exciton radius (nm)
CdSe	2.87	5.3
ZnSe	2.67	4.5
CdS	2.43	5.8
CdTe	1.5	15
GaAs	1.43	28.0
InP	1.35	15
PbS	0.41	40
InAs	0.354	34
InSb	0.17	65.6

The size-effective bandgap (E_{QD}) for the lowest energy states for QDs confinement is defined by:

$$E_{QD} = E_{bulk} + \frac{\pi^2 \hbar^2}{2d^2}\left(\frac{1}{m_e} - \frac{1}{m_h}\right) - \frac{3.6q_e^2}{\epsilon d}$$

Where ϵ is the dielectric constant, m_e and m_h are the reduced mass of the electron-hole pair respactaly, and d is the nanocrystal diameter. Observing the first term on the right hand side describes the energy bandgap value of the bulk, the second term represents particle in a box quantum confinement model, and the third term details the Coulomb attraction between electron and hole (exciton). As the radius of the quantum dot decreases the Coulomb attraction term could be neglected compared to the second term in calculations. Therefore, the equation indicates that bandgap energy eigenvalues increases as the quantum dot size decreases. [9]

Thus, tuning the size of the quantum dots (QDs) for this stage benefits the design in maximizing the absorption of the incident light upon illumination of the PV cell (Fig. 19).

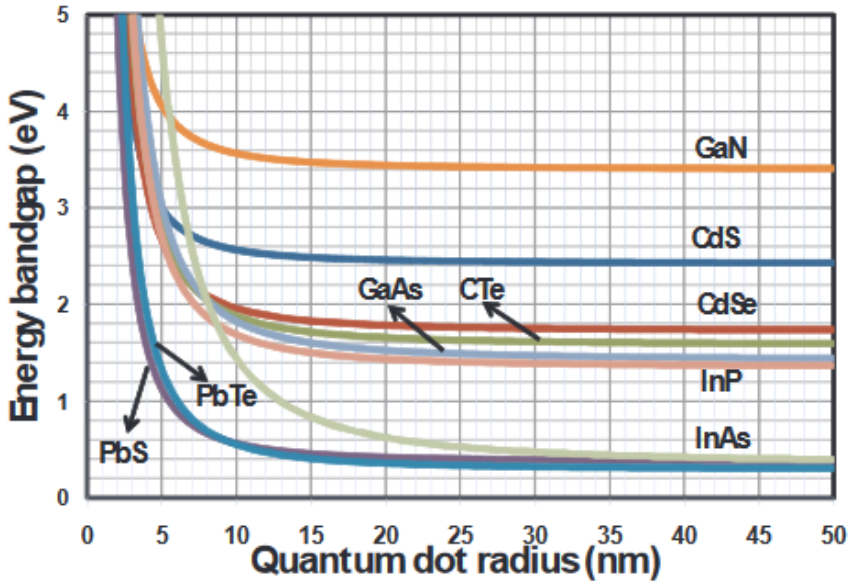

Figure 19: Bandgap to size relationship for different material based quantum dots [10].

In order to make better use of low energy photons of the solar spectrum, low dimensional quantum structures have been introduced into p-i-n structures and different self-assembled quantum dots (QDs) systems [10-11]. In theory, that incorporation of QDs into the intrinsic region of p-i-n solar cells can indeed extend their photoresponse to a broader wavelength range.

2.2.1 *Targeted QDs for the solar cell design*

As seen in (Fig. 19), many materials can be used in the design of QDSSC. However, only a few of them have the properties that match our criteria entirely or almost completely, especially for the nontoxic and non-rare elements; they are declined hereafter.

2.2.1.1 Copper Indium Sulfide (CIS)

Copper Indium Sulfide (CIS) has risen as a new semiconductor material with high potential in photon emitting and absorption applications [12]. Because of its relatively low toxicity (not containing heavy metals in its structure) compared to Cd and Pb, high absorption coefficients with well-matched bandgap (1.5 eV) in bulk material, and widely tunable emission wavelength range [13]. Its only drawback is in its indium content.

Based on several studies, the optical properties of synthesized CIS QDs can be tuned by varying their size. They appear so as yellow (a: 2.5nm), orange (b: 3.0nm), red (c: 3.5nm), dark red (d: 4.5nm), and brown (e: 5.5nm) (Fig. 20) [14].

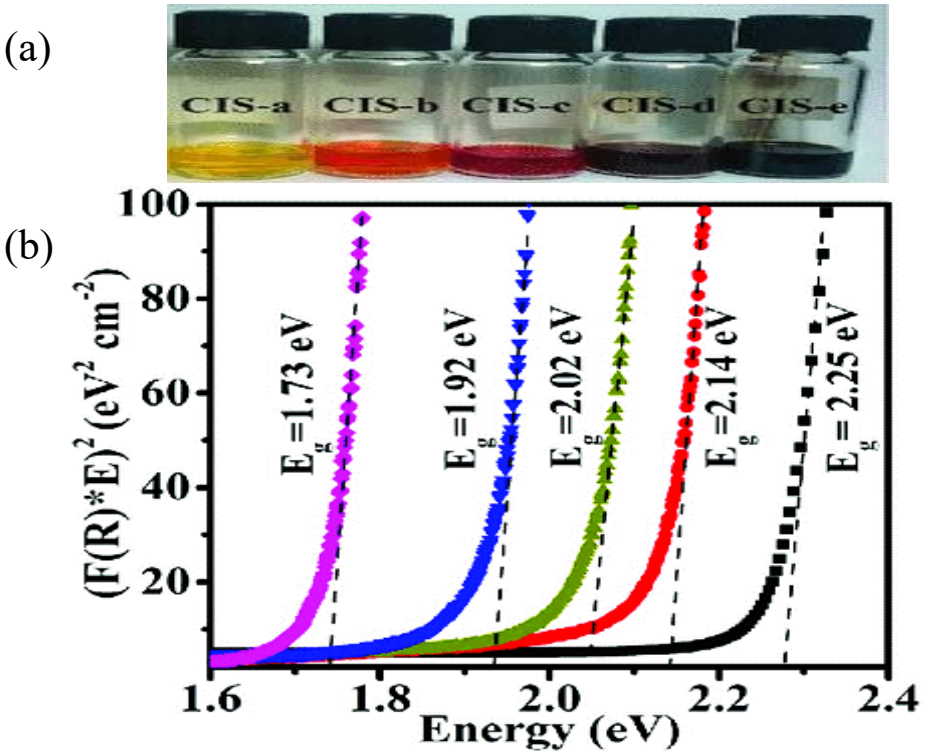

Figure 20: a) color change versus QDs size. b) corresponding Tauc plot [14].

Furthermore, the possibility of changing the Cu:In ratio increases the tunability in bandgap engineering, as seen in Table II. The QDs absorption shown in (Fig. 21) illustrates the possibility of two independent electron transitions, a direct and an indirect one. [15-19]

Table II: Bandgap tunability of CIS QDs upon Cu/In ratio [18].

	[Cu]:[In] precursors	[Cu]:[In] ICP	size by STEM (nm)	sample name
a	1.0	1.26 ± 0.06	2.6 ± 0.4	$Cu_{1.2}InS_2$ (2.6 nm)
b	1.0	1.14 ± 0.12	4.0 ± 0.6	$CuInS_2$ (4.0 nm)
c	0.7	0.77 ± 0.03	2.5 ± 0.3	$Cu_{0.8}InS_2$
d	0.5	0.61 ± 0.02	2.6 ± 0.4	$Cu_{0.6}InS_2$
e	0.25	0.48 ± 0.02	2.5 ± 0.2	$Cu_{0.5}InS_2$

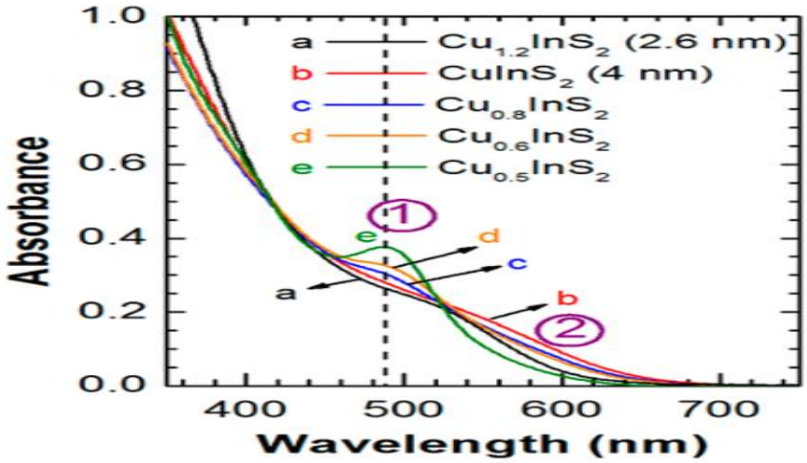

Figure 21: Composition and size-dependent absorption spectra of CIS QDs [18].

2.2.1.2 $ZnSnN_2$

The Zn-IV-N_2 semiconductor family represents a potential earth-abundant element alternative for PV and lighting applications, with a predicted bandgap range of ~0.6 to ~5 eV depending on IV element and composition. It has been experimentally observed that $ZnSnN_2$ has a direct bandgap energy of ~1.7 eV that can fit in multi-energy schemes [20]. In contrast to indium, zinc and tin are already recycled in large amounts globally. They are a magnitude less of demand and less expensive, thus providing both economic and

environmental benefits. Like InGaN, alloys of this family can have bandgaps spanning from the near-infrared to the near UV and hence are well matched to the solar spectrum, making them candidates for photovoltaic applications [21], as well as of interest for solid-state lighting (Fig. 22).

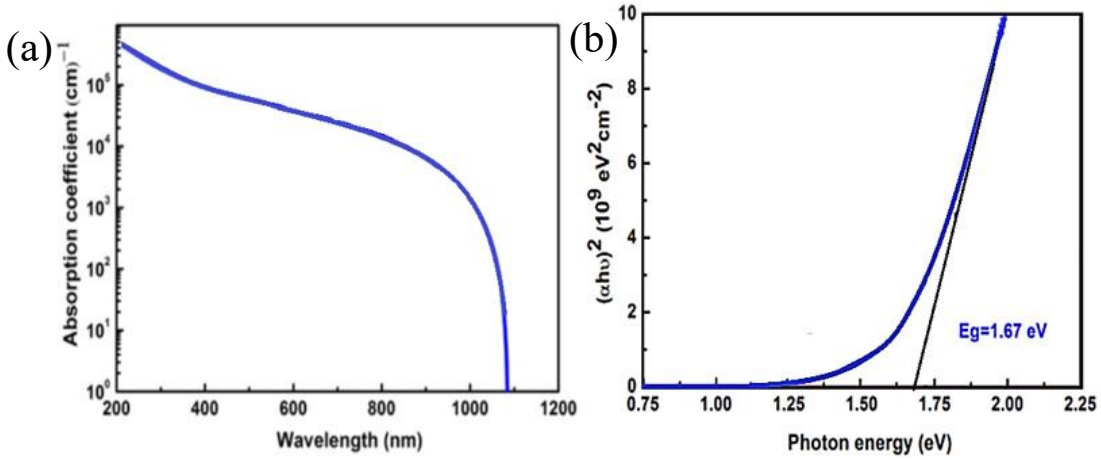

Figure 22: Properties of $ZnSnN_2$ film about 300 nm a) UV–vis absorption spectrum b) bandgap determination using the Tauc model [22].

2.2.1.3 Copper-based Perovskite material

La_2CuO_4 nanoparticles of 40–50 nm have been synthesized [23]. They exhibited a broad absorption band in the UV–vis region (200– 800 nm) (Fig. 23a). It has been concluded that this material has a direct bandgap value of 1.24 eV, which is almost ideally located in the range of effective light absorption (Fig. 23b).

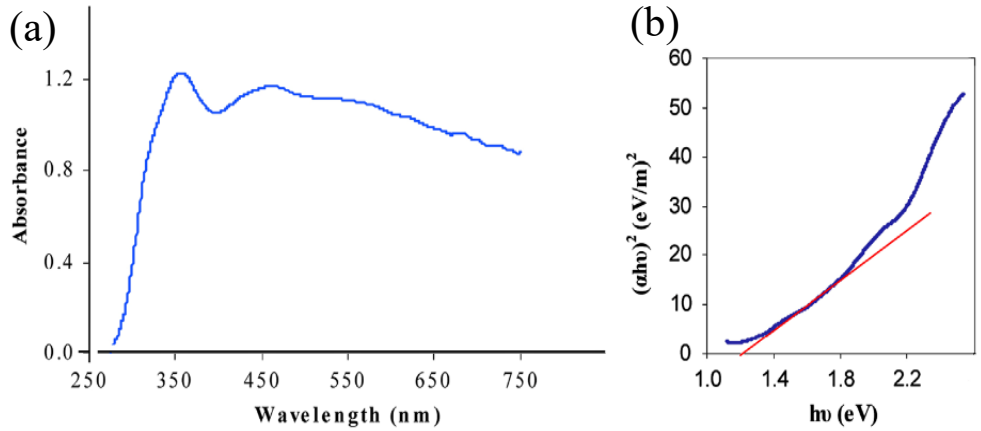

Figure 23: Properties of La_2CuO_4 nanoparticles: a) UV–vis absorption spectrum b) band gap determination [23] (to be noted that absorbance value higher than 1 is a non physical value but it is cited like this by the authors).

2.3 Electron transport layer (MOs)

Different metal oxides materials, such as zinc oxide (ZnO), aluminum doped (3%) zinc oxide (AZO), titanium dioxide (TO_2) and tin(IV) oxide (SnO_2), have been investigated as electron transport layer materials for QDSSCs owing to particular advantages. For example, $SnO_2$and ZnO (Fig. 24a and 24b, respectively), both, have wide electronic bandgap as semiconductor materials (3.2eV and 3.6eV, respectively), and high bulk electron mobility (205–300 cm^2 / V.s). [24, 26]

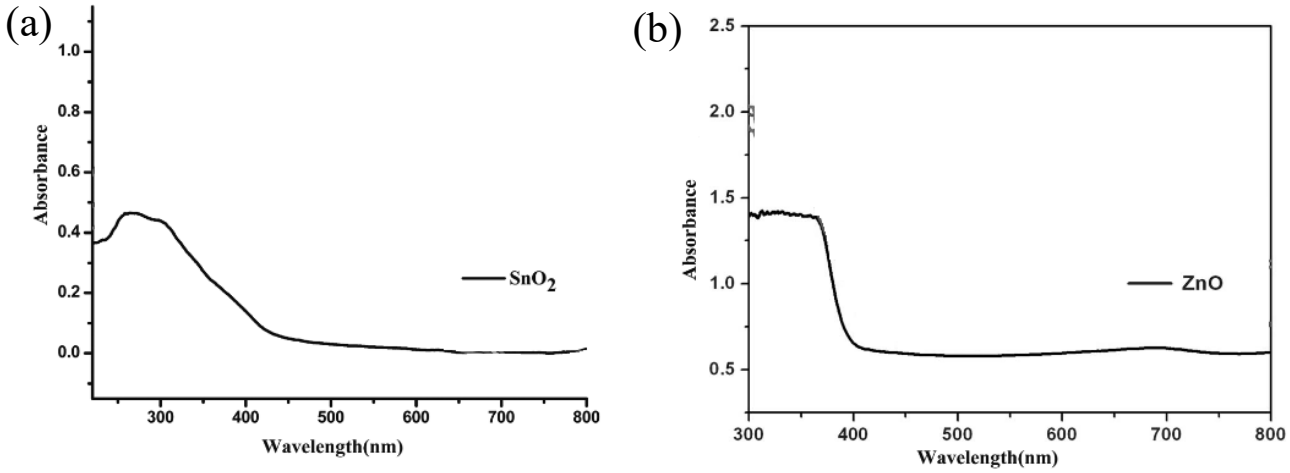

Figure 24: UV-vis spectroscopy of a) SnO_2, b) ZnO [23-26].

Based on that, such layers of MO have already provided optical and electrical properties, strain relaxation effects, charge separation mechanisms, and cost-effectiveness [27]. In this work, we lean on the knowledge acquired from a previous project that allowed determining optimized deposition parameters for the MOs fabrication.

2.4 Charge collection layer (electrodes)

Electrode layer materials shall be capable of collecting the charges and passing them to an outer load. Materials like TCOs (Transparent Conductive Oxides) are used as electrode layers for new solar cells designs, an example for such groups the ITO (Indium Tin Oxide) and FTO (Fluorine doped Tin Oxide) [28]. Their drawbacks are the availability of indium (rare element), instability in the presence of acid or base, limited transparency in the near-infrared region, as well as reduction of electrons mobility caused by FTO structure defects

[29]. Those defects (cracks) are formed whenever a physical pressure applied to the TCOs.In order to target device flexibility, graphene layers seem promising for such functionality.

2.4.1 *Kapton as a substrate*

The Kapton (Fig. 25) has more than 40 years of demonstrated performance as the material of choice in applications involving flexibility and operating under high temperature (maximum 450ºC), high pressure, and a variety of chemicals resistance. [46,47]

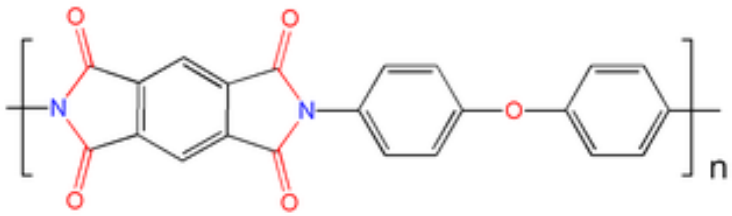

Figure 25: DuPont™ Kapton® polyimide film (***PV9100 SERIES***)

Prevailing with low coefficient of thermal expansion, high glass transition temperature, and low shrinkage of Kapton, such films help minimize stress at the interface with other materials, both during processing and during end-use in temperature extremes. The thermal stability of Kapton films is excellent and allows processing temperatures more than 400°C.

2.4.2 *Graphene as Electrodes*

The advantages of using graphene as an electrode are in its environmental, thermal, and photostability properties that are of great concern for long-term stability. Graphene, single-layer graphite, is then an attractive candidate for flexible transparent conductive electrodes (TCE) for solar cells since it meets all prerequisites concerning electrical and optical properties. [30]

Table III summarizes and compares standard solar cell properties for different electrode materials used for QDSSCs. Since all cells are different in nature, it is difficult to draw a

quantitative study. Nevertheless, a qualitative comparison on FF value shows the advantages of graphene decreasing the access resistance (and so increasing the FF).

Table III: Electrodes survey showing the different parameters (Jsc, Voc, FF and efficiency).

Electrode	Jsc ($mA.cm^{-2}$)	Voc (V)	FF	η	Ref
Graphene	7.70	0.68	0.54	2.82	[31]
Graphene	16.99	0.747	0.536	6.81	[32]
Graphene	6.12	0.64	0.56	2.19	[33]
Graphene	5.60	0.70	0.6	2.3	[34]
Graphene	14.3	0.54	0.653	5.69	[34]
Graphene	8.11	0.72	0.46	2.64	[35]
Graphene	6.42	0.70	0.16	0.74	[36]
Pt	10	0.74	0.58	5	[37]
Pt	6.09	0.46	0.38	1.06	[38]
MoO/ Al	17.9	0.52	0.48	4.46	[39]
MoO/Ag	18.7	0.53	0.48	4.53	[39]
MoO/Au	17.4	0.54	0.47	4.41	[39]

However, different deposition techniques exist and are still under investigation. Many studies nowadays are investigating the deposition of graphene as bottom and top electrodes for solar cell devices. Although considerable progress has been achieved, the research is still in its primary stages, and many challenges still have to be addressed and resolved in terms of improving the interfacial contact with the active layer, the deposition method, and the conductivity properties.[48]

2.5 Energy scheme of the design

The introduced nanomaterials and nanostructures such as QDs will allow to use an energy configuration known as the “intermediate band-gap solar cell” for our design.

The intermediate band-gap (IB) solar cell energy configuration has multiple sub-bandgap energy levels involved in the absorption of light waves (photons) and not only a fixed single bandgap like what is known in a conventional semiconductor (classical p-n junction(. The multiple photons that are absorbed in those sub-bandgaps would generally mean an higher efficiency. Although this concept (IB) was gradually researched to be a possibility in solar cell performance enhancement since the 60s [40], more recent theoretical studies of an electron band transition have predicted, in ideal conditions, potential efficiency as high as 63% [41]. Therefore, applying this concept will help in passing through the Shockley-Queisser limit of the conventional bulk materials under the same conditions of illumination. In (Fig. 26), the illustration shows the energy band diagram of the ideal intermediate band in the solar cell. It can be seen the usual bands: conduction band (CB) and valence band (VB) and the intermediate band (IB) in the middle. Apart the usual electron transition between VB and CB corresponding to an energy level (E_G), two additional energy absorption transitions exist then: from VB to IB and from IB to CB corresponding to E_L and E_H energy levels, respectively. [42]

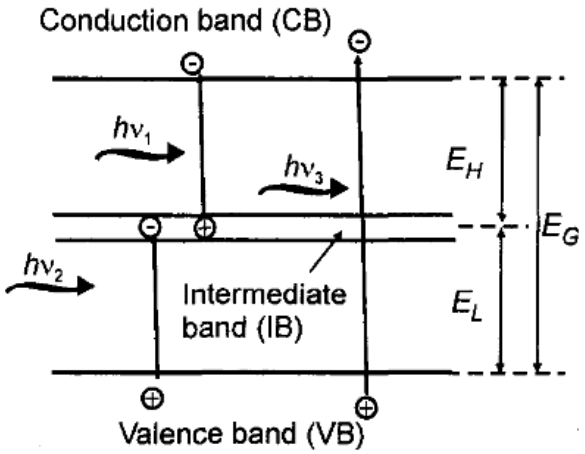

Figure 26: Schematic of the intermediate band material [42].

Fig. 27 sketches the structure of the active layer in the solar cell, with the QD material between the necessary layers needed to extract the photocurrent.

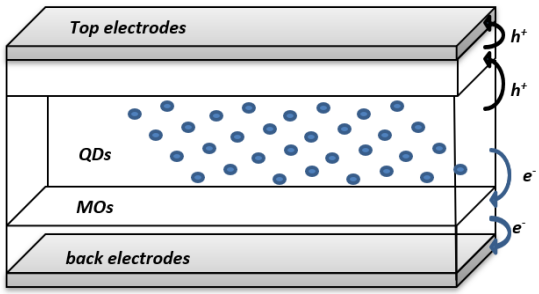

Figure 27: Sketch of the QD intermediate band solar cell.

The conversion of the solar energy to electrical power can be summarized in a sequence of events that must take place inside the cell. This sequence is presented in Fig. 28.

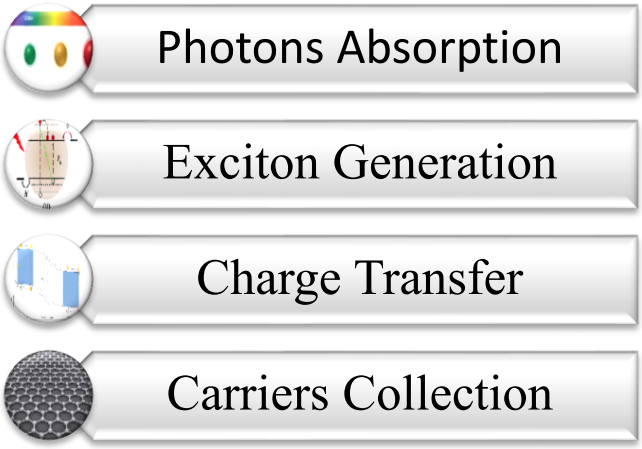

Figure 28: Solar energy conversion scheme.

It starts with the absorption of light that generates charge carriers (electrons and holes), then the separation of the electrons from holes happen to end up with their transport to and collection by the electrodes.

2.5.1 *Photon Absorption*

The energy obtained from the solar spectrum photons will be proportionally increased to the increasing wavelength range being absorbed. Never forget that the photon energy that is greater than the one requested to free an electron would be released out in the material as thermal energy, reducing so the efficiency.

2.5.2 *Generation of charge carriers*

The light absorption causes the excitation of an electron from the valence band to the conduction band. In order to harvest the potential energy of this electron-hole pair over an external load, the pairs must be separated spatially using the semiconducting oxide layer (TiO_2, ZnO, SnO_2, etc.) with QDs attached to it. The design would have a wide bandgap and intermediate one to direct the electrons and the holes in the right shift and work at the same time as a barrier for reverse movement. Fig. 29 illustrates such behavior and shows an example of the energy levels and sub-levels of the absorption layer.

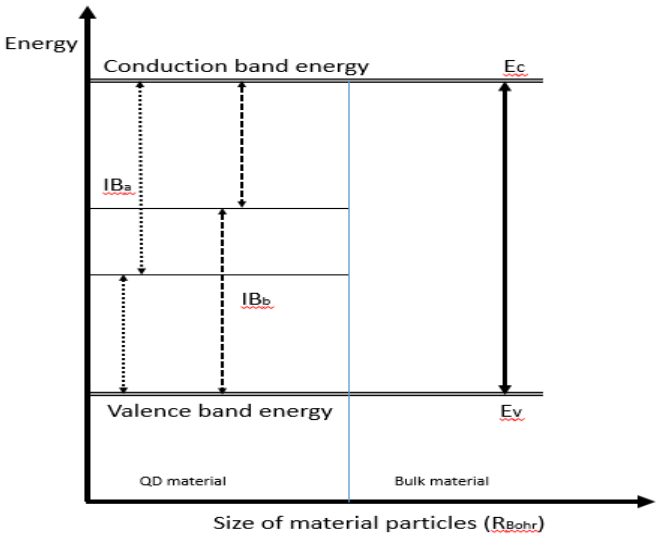

Figure 29: Energetic electron transfer alignment in QD material (IB) and bulk materials direct bandgap in semiconductors.

The excited electrons in the conduction band are transferred from the absorption layer to the thin film MO. This transfer occurs by the difference in work functions between the two materials [43, 44].

2.5.3 *Carrier collection*

Once electrons are transferred to the MOs, the unique geometry properties of the MOs will capture the photo-generated charges and transport them to electrodes. Furthermore, the injected electrons are transported directly and very shortly to the electrodes.

In this way, one cycle is completed: photons are absorbed by semiconductor nanoparticles and photogenerated charge carriers are transferred to the electrodes by wide bandgap metal oxide structures. At each step, the recombination of electron and hole can occur, preventing their contribution to the external current. In addition to the fundamental restrictions of the device, such as how much light can be absorbed, these recombination losses limit the overall maximum efficiency of the device and hence need to be minimized by all possible means. Furthermore, the charge transfer is essential, especially in the case of using a linker, where a ligand exchange process must be executed to improve the charge transfer. In our design, ligand would be a problem for the duration of the solar cell thought they would not be used.

The need for sustainable, highly efficient, lightweight, and flexible solar cells can be achieved by selecting an eco-green material with appropriate nanostructures in the designed solar cell.

As electrodes present one of the main building blocks in solar cells, it is very crucial to work on improving their electrical, chemical, mechanical, and optical properties to improve the performance of solar cells.

2.6 Conclusion: the plan of fabrication

The construction of the solar cell starts at the bottom electrode, which is made of a thin conducting layer deposited on a flexible substrate. A donor (absorber of light/electron generation) - acceptor (electron picker and transporter to the electrodes) material has then to be deposited on top of it as an active photovoltaic component, as shown in Fig. 30.

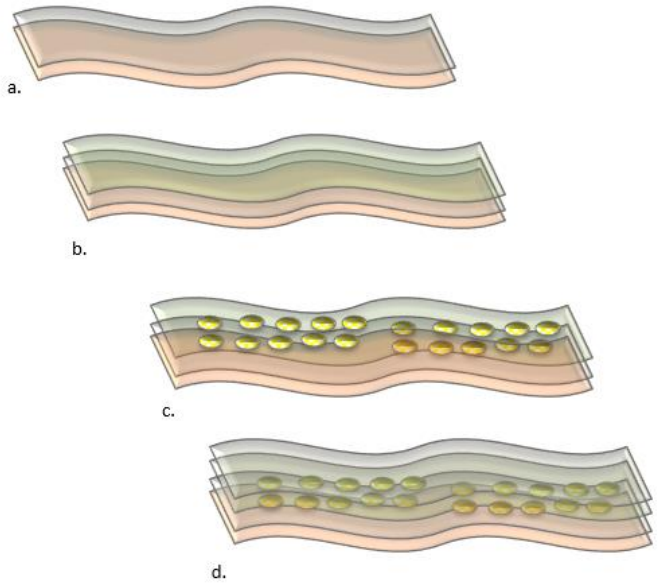

Figure 30: Schematic of the solar cell fabrication process:
a) bottom electrode deposition on a flexible substrate,
b) metal oxide deposition, c) quantum dots synthesis, d) top electrode deposition.

The active layer is composed of two different groups of materials, each being dedicated to a specific functionality. The conversion process starts when QDs first absorb photons, placing them in an electronically excited state $QD + Photon\ energy \rightarrow QD_{exited}$. Shortly after the absorption, the electrons and holes relax to their most excited energetically auspicious states, namely the conduction and valence band edges, correspondingly, creating an electron-hole pair:

$$QD_{exited} \rightarrow QD(e^- + h^+)$$

In order to harvest the potential energy of those pairs through an external load, the electrons and holes must be separated spatially; This is achieved through the electron transfer depicted by:

$$\mathrm{QDs}(e^- + h^+) + \mathrm{MO} \rightarrow \mathrm{QDs}(h^+) + \mathrm{MO}(e^-)$$

Through which an electron moves from the QD conduction band to the MO conduction band. As soon as spatially separated from the photo-generated hole, the electron must then cross to the MO layer:

$$\mathrm{MO}(e^-) \rightarrow \mathrm{MO}(e^-)_{\text{nearest neighbor}}$$

The electrons transfer to the circuit at the working electrode

$$\mathrm{MO}(e^-) + \mathrm{electrode} \rightarrow \mathrm{MO} + \mathrm{electrode}(e^-)$$

For the meantime, the photo-generated hole remaining in the QD valence band is shifted by the hole transport layer:

$$\mathrm{QDs}(h^+) + \mathrm{electrode} \rightarrow \mathrm{QDs} + \mathrm{electrode}(h^+)$$

which then needs to diffuse spatially away from the QD layer to the electrode [44]. This principle is schematically shown in Fig. 31.

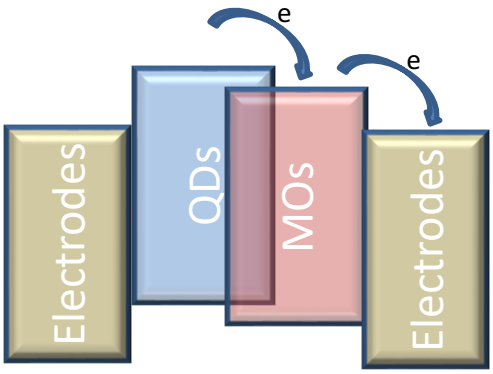

Figure 31: Schematic view of carrier transport within the absorbing layer composed of QDs and MO layer.

These possible effects will be studied in detail in this thesis to investigate the operation of intermediate band solar cells based on quantum dot structures with MOs and graphene layers.

References

1. Ayers, J.E., *Digital integrated circuits: analysis and design*. 2011: CRC Press.
2. Adler, F., et al., *Optical transitions and carrier relaxation in self assembled InAs/GaAs quantum dots.* Journal of Applied Physics, 1996. **80**(7): p. 4019-4026.
3. Ohnesorge, B., et al., *Rapid carrier relaxation in self-assembled In x Ga 1− x As/GaAs quantum dots.* Physical Review B, 1996. **54**(16): p. 11532.
4. Fu, L., et al., *Effects of rapid thermal annealing on device characteristics of In Ga As/ Ga As quantum dot infrared photodetectors.* Journal of applied physics, 2006. **99**(11): p. 114517.
5. Alivisatos, A.P., *Semiconductor clusters, nanocrystals, and quantum dots.* science, 1996. **271**(5251): p. 933-937.
6. Yong, K.-T., et al., *Imaging pancreatic cancer using bioconjugated InP quantum dots.* ACS nano, 2009. **3**(3): p. 502-510.
7. Bharali, D.J., et al., *Folate-receptor-mediated delivery of InP quantum dots for bioimaging using confocal and two-photon microscopy.* Journal of the American Chemical Society, 2005. **127**(32): p. 11364-11371.
8. Langof, L., et al., *Continuous-wave and time-resolved optically detected magnetic resonance studies of nonetched/etched InP nanocrystals.* The Journal of Physical Chemistry B, 2002. **106**(7): p. 1606-1612.
9. Yoffe, A.D., *Semiconductor quantum dots and related systems: electronic, optical, luminescence and related properties of low dimensional systems.* Advances in physics, 2001. **50**(1): p. 1-208.
10. Jasim, K.E., *Quantum dots solar cells.* Solar Cells-New Approaches and Reviews, 2015: p. 303-331.
11. Jasim, K.E., *Dye sensitized solar cells-working principles, challenges and opportunities*, in *Solar Cells-Dye-Sensitized Devices*. 2011, InTechOpen.
12. Chen, B., et al., *Highly emissive and color-tunable CuInS2-based colloidal semiconductor nanocrystals: off-stoichiometry effects and improved electroluminescence performance.* Advanced Functional Materials, 2012. **22**(10): p. 2081-2088.
13. McDaniel, H., et al., *Engineered CuInSe x S2–x Quantum Dots for Sensitized Solar Cells.* The journal of physical chemistry letters, 2013. **4**(3): p. 355-361.
14. Ilaiyaraja, P., et al., *CuInS2 quantum dot sensitized solar cells with high VOC≈ 0.9 V achieved using microsphere-nanoparticulate TiO2 composite photoanode.* Solar Energy Materials and Solar Cells, 2018. **178**: p. 208-222.
15. Song, W.-S. and H. Yang, *Efficient white-light-emitting diodes fabricated from highly fluorescent copper indium sulfide core/shell quantum dots.* Chemistry of Materials, 2012. **24**(10): p. 1961-1967.
16. Chang, C.-C., et al., Synthesis of eco-friendly CuInS2 quantum dot-sensitized solar cells by a combined ex situ/in situ growth approach. ACS applied materials & interfaces, 2013. 5(21): p. 11296-11306.
17. Guijarro, N., et al., *Quantum dot-sensitized solar cells based on directly adsorbed zinc copper indium sulfide colloids.* Physical Chemistry Chemical Physics, 2014. **16**(19): p. 9115-9122.

18. Jara, D.H., et al., *Size-dependent photovoltaic performance of CuInS2 quantum dot-sensitized solar cells.* Chemistry of Materials, 2014. **26**(24): p. 7221-7228.
19. Jara, D.H., K.G. Stamplecoskie, and P.V. Kamat, *Two Distinct Transitions in Cu x InS2 Quantum Dots. Bandgap versus Sub-Bandgap Excitations in Copper-Deficient Structures.* The journal of physical chemistry letters, 2016. **7**(8): p. 1452-1459.
20. Feldberg, N., et al. *ZnSnN2: A new earth-abundant element semiconductor for solar cells*. in *Photovoltaic Specialists Conference (PVSC), 2012 38th IEEE*. 2012. IEEE.
21. Punya, A., W.R. Lambrecht, and M. van Schilfgaarde, *Quasiparticle band structure of Zn-IV-N 2 compounds.* Physical Review B, 2011. **84**(16): p. 165204.
22. Javaid, K., et al., *Thin film solar cell based on ZnSnN2/SnO heterojunction.* physica status solidi (RRL)–Rapid Research Letters, 2018. **12**(1): p. 1700332.
23. Enhessari, M., et al., *Synthesis, characterization and optical band gap of La2CuO4 nanoparticles.* Materials Science in Semiconductor Processing, 2013. **16**(6): p. 1517-1520.
24. Ranjit, K. and B. Viswanathan, *Synthesis, characterization and photocatalytic properties of iron-doped TiO2 catalysts.* Journal of Photochemistry and Photobiology A: Chemistry, 1997. **108**(1): p. 79-84.
25. Devi, L.G. and R. Shyamala, *Photocatalytic activity of SnO 2–α-Fe 2 O 3 composite mixtures: exploration of number of active sites, turnover number and turnover frequency.* Materials Chemistry Frontiers, 2018. **2**(4): p. 796-806.
26. Liu, Z.-Q., et al., *ZnO/SnO 2 hierarchical and flower-like nanostructures: facile synthesis, formation mechanism, and optical and magnetic properties.* CrystEngComm, 2012. **14**(6): p. 2289-2295.
27. Gerischer, H., *Electrochemical techniques for the study of photosensitization.* Photochemistry and Photobiology, 1972. **16**(4): p. 243-260.
28. Schmidt-Mende, L., et al., *Self-organized discotic liquid crystals for high-efficiency organic photovoltaics.* Science, 2001. **293**(5532): p. 1119-1122.
29. Wang, L., et al., *Near-infrared transparent electrodes for precision Teng–Man electro-optic measurements: In 2 O 3 thin-film electrodes with tunable near-infrared transparency.* Applied Physics Letters, 2005. **87**(16): p. 161107.
30. Wang, Z., et al., *Technology ready use of single layer graphene as a transparent electrode for hybrid photovoltaic devices.* Physica E: Low-dimensional Systems and Nanostructures, 2011. **44**(2): p. 521-524.
31. Kaniyoor, A. and S. Ramaprabhu, *Thermally exfoliated graphene based counter electrode for low cost dye sensitized solar cells.* Journal of Applied Physics, 2011. **109**(12): p. 124308.
32. Zhang, D., et al., *Graphene-based counter electrode for dye-sensitized solar cells.* Carbon, 2011. **49**(15): p. 5382-5388.
33. Hsieh, C.-T., B.-H. Yang, and J.-Y. Lin, *One-and two-dimensional carbon nanomaterials as counter electrodes for dye-sensitized solar cells.* carbon, 2011. **49**(9): p. 3092-3097.
34. Choi, H., et al., *Electrophoretic graphene for transparent counter electrodes in dye-sensitised solar cells.* Electronics letters, 2011. **47**(4): p. 281-283.
35. Cruz, R., D.A.P. Tanaka, and A. Mendes, *Reduced graphene oxide films as transparent counter-electrodes for dye-sensitized solar cells.* Solar Energy, 2012. **86**(2): p. 716-724.
36. Choi, H., et al., *Graphene counter electrodes for dye-sensitized solar cells prepared by electrophoretic deposition.* Journal of Materials Chemistry, 2011. **21**(21): p. 7548-7551.

37. Battumur, T., et al., *Graphene/carbon nanotubes composites as a counter electrode for dye-sensitized solar cells.* Current Applied Physics, 2012. **12**: p. e49-e53.
38. Yu, F., et al., *A new breakthrough for graphene/carbon nanotubes as counter electrodes of dye-sensitized solar cells with up to a 10.69% power conversion efficiency.* Journal of Power Sources, 2019. **412**: p. 366-373.
39. Gao, J., et al., *n-Type transition metal oxide as a hole extraction layer in PbS quantum dot solar cells.* Nano letters, 2011. **11**(8): p. 3263-3266.
40. Wolf, M., *Limitations and possibilities for improvement of photovoltaic solar energy converters: Part I: Considerations for earth's surface operation.* Proceedings of the IRE, 1960. **48**(7): p. 1246-1263.
41. Ley, M., J. Boudaden, and Z. Kuznicki, *Thermodynamic efficiency of an intermediate band photovoltaic cell with low threshold Auger generation.* Journal of applied physics, 2005. **98**(4): p. 044905.
42. Martí, A., L. Cuadra, and A. Luque. *Quantum dot intermediate band solar cell*. in *Conference Record of the Twenty-Eighth IEEE Photovoltaic Specialists Conference-2000 (Cat. No. 00CH37036)*. 2000. IEEE.
43. Ginger, D. and N. Greenham, *Photoinduced electron transfer from conjugated polymers to CdSe nanocrystals.* Physical Review B, 1999. **59**(16): p. 10622.
44. Sariciftci, N. and A. Hebger, *Reversible, metastable, ultrafast photoinduced electron transfer from semiconducting polymers to buckminsterfullerene and in the corresponding donor/acceptor heterojunctions.* International Journal of Modern Physics B, 1994. **8**(03): p. 237-274.
45. Kamat, P.V., *Boosting the efficiency of quantum dot sensitized solar cells through modulation of interfacial charge transfer.* Accounts of chemical research, 2012. **45**(11): p. 1906-1915.
46. Znajdek, K., et al., Polymer substrates for flexible photovoltaic cells application in personal electronic system. Opto-Electronics Review, 2016. 24(1): p. 20-24.
47. Glascock, N., et al., *MAFSA: Mars Autonomous and Foldable Solar Array.* New Space, 2018. **6**(4): p. 308-319.
48. Ishikawa, R., et al., *Perovskite/graphene solar cells without a hole-transport layer.* ACS Applied Energy Materials, 2019. **2**(1): p. 171-175.

Chapter 3

Developing the Layers

3.1 Introduction to the development of solar cell

In this chapter, we will go through the two main approaches for the fabrication of the designed solar cell:

1. A 3D structure targeting ultimate device design.
2. A 2D thin-film structure as a proof of concept for material fabrication.

In the fabrication process of each layer, different technologies and processes were used. Some of those technologies gave suitable layers for their role in the solar cell and have been used to build the design. Some others gave fair or even enhanced results but could not be used, due to several reasons such as:

- growth mismatch between layers,
- high defect density at the interface,
- deposition process altering previous layer(s) in the way of damaging, peeling, or changing some of its (their) characteristics.

On the other hand, experimental results are not so good as expected from the literature reported theoretical projections, due to the lack of high purity base material, contamination that could not be avoided in a step of the process and finally few harsh calibrations on fabrication equipment that could not be solved.

3.2 Fabrication technology

The general classification of deposition techniques can be divided into two large families:

1. Physical Vapor Deposition (PVD): it refers to processes where solid materials - metallic or metal compounds - are physically passed into the vapor phase within a controlled and reduced pressure chamber. Material is then transported from the source to the substrate, at which creation of seeds, islands, or thin layers initializes and, with time, proceeds to growth.

The physical deposition can be divided into four key technologies that are thermal evaporation, (magnetron) sputtering, ion-beam evaporation, and pulsed laser deposition (Fig. 32).

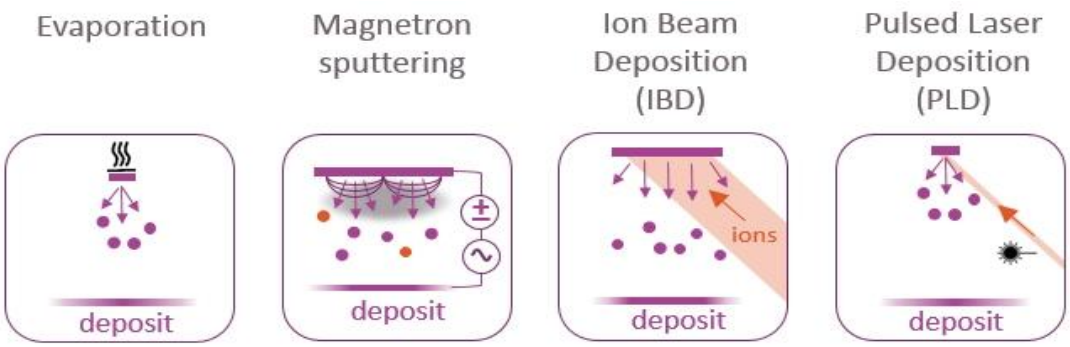

Figure 32: PVD technologies [1].

2. Chemical Deposition: gathers the deposition techniques that depend on a chemical reaction. Two main branches can be discerned:
    a. Chemical Vapor Deposition (CVD): the chemical reaction can happen under different conditions such as Atmospheric-Pressure (APCVD), Low-Pressure (LPCVD), Metal-Organic (MOCVD), Plasma-Enhanced (PECVD), Atomic Layer Deposition (ALD) or Laser-Induced (LCVD).
    b. Liquid or Wet phase chemical Deposition: also, several techniques exist there such as Chemical Bath Deposition (CBD), spray pyrolysis, electroplating, or sol-gel deposition. An enhanced CBD process, called successive ionic layer adsorption and reaction (SILAR), has been set up by cycling the reaction to deposit thicker films. It can be also be included as a subbranch of this type of deposition technique.

One can notice that the chemical techniques of group 2a) above, similarly to physical techniques of group 1, require heavy equipment deposition tools. On the contrary, the chemical techniques of group 2b) require simple, less expensive, and less sophisticated deposition tools.

The synthesis of QDs and thin films using those technologies is based on three main phases:

1) formation of the suitable atomic, molecular, or ionic deposition material,
2) transport of the material from the source to the substrate,
3) condensation of the material on the substrate directly or by a chemical reaction with reactive constituents and forming a small deposit.

In those processes, the solid film is formed by condensation of the atoms in the vapor phase onto a substrate and migration to nucleation and growth locations. The adsorbed atoms, called adatoms, require enough energy to occupy their lowest probable energy configurations avoiding structural deficiencies. The structure and morphology of the growing film is also a result of the deposition process and its respective parameters. The deposition processes that are presently being employed for the deposition of transparent inorganic barrier films will be from now on described.

In the following, we will quickly describe the different deposition techniques that have been used in this work.

3.2.1 *Magnetron sputtering (used in IEMN)*

In this work, the development of the first approach, i.e., PVD technology, will mainly be based on the sputtering deposition.

This technology involves ejecting material from a source, called the target, of the desired material to be deposited onto the sample top surface. In this work, the materials that were deposited such a technique are the AZO (Aluminum doped zinc oxide) for the metal oxide layer and La_2CuO_4 for the active layer.

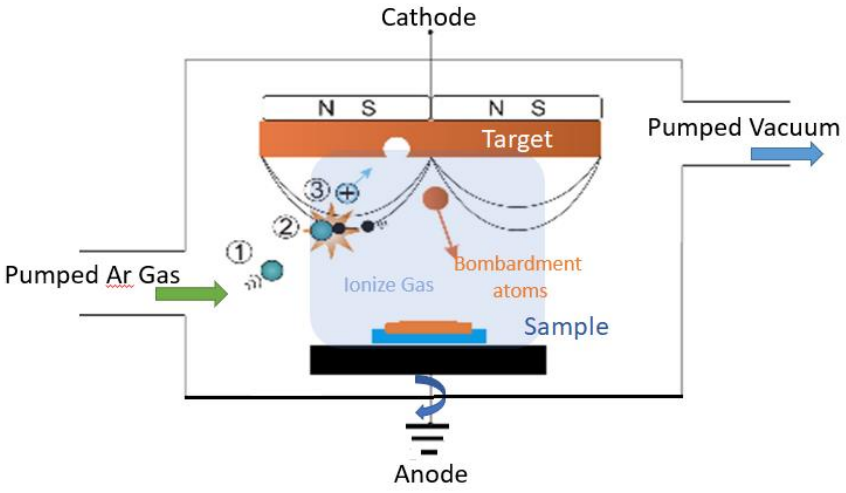

Figure 33: Schematic illustration of magnetron sputtering: 1. Argon gas is pumped into the chamber 2. existing electrons inside the chamber ionize Argon gas atom. 3. Argon gas ions hit the target and sputter it. 4. bombardment atoms cover the sample substrate.

The sputtering deposition process consists of an atom or ion bombardment of the target within an inert or even reactive gas atmosphere that has been ionized into a plasma created between the sample and the target by electrically exciting the cathode (target). The target is then sputtered by the positive ions that are accelerated towards the inbuilt plasma electric field. In order to increase the deposition velocity, species confinement by using a magnetic field (Fig. 33) is usually employed, leading to the so-called magnetron sputtering deposition process.

The main parameters of the Magnetron sputtering process can be seen in Fig. 34.

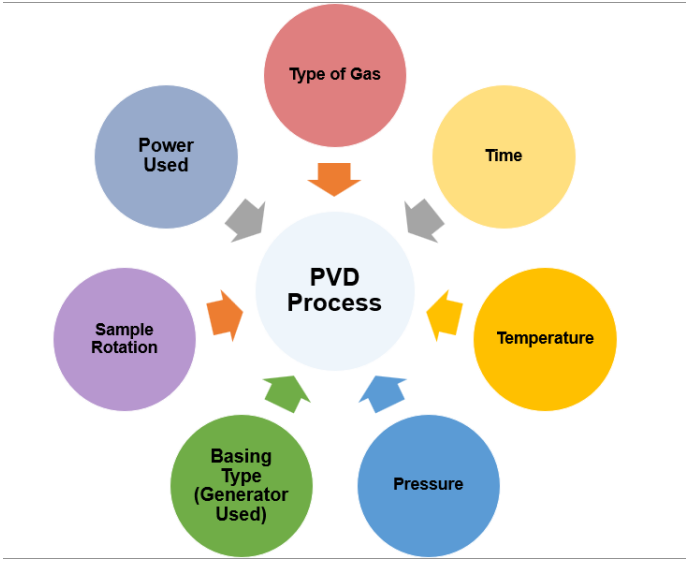

Figure 34: Control parameters of a magnetron sputtering chamber.

Those parameters manipulate the deposited thin film in terms of thickness, structure, and surface topology. Thornton model, shown in (Fig. 35), can help in estimating the right parameter set to obtain the desired layer structuration [2].

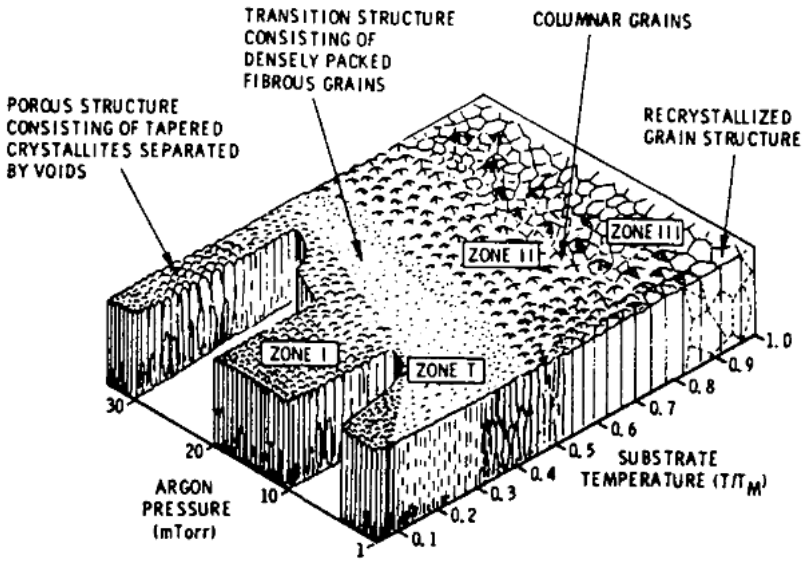

Figure 35: Thornton model zones [3].

This generic operation model is nevertheless material (and also equipment) dependent, and it has been noticed that the different zones are formed with a slight shift depending on whether material is metal or metal-oxide (Fig. 36).

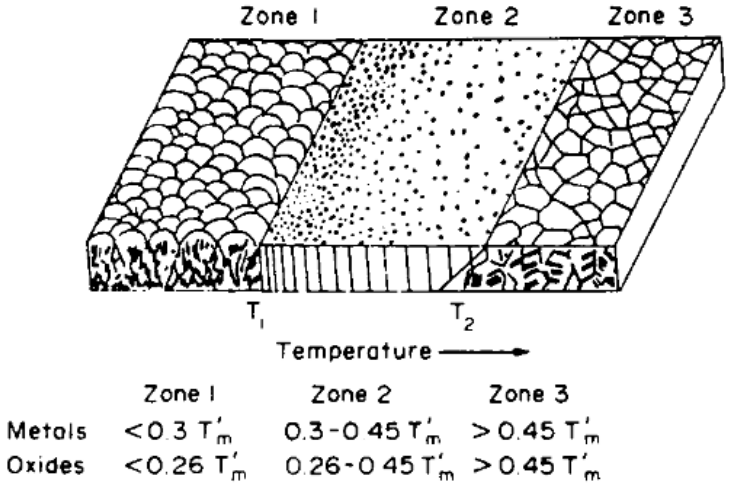

Figure 36: Thornton model shows variation depending on the deposited material [3].

Additionally, the sputtering technique can be used in different modes of biasing the cathode (target) and anode (sample). Depending on the used deposition mode, the deposition velocity can be changed. To summarize them, there is Direct Current sputtering (DC-S), the Radio Frequency sputtering (RF-S), the pulsed DC sputtering (PDC-S) the dual magnetron sputtering (DM-S), the bipolar pulsed dual magnetron sputtering (BPDM-

S), the modulated pulsed power magnetron sputtering (MPPM-S) and the dual anode sputtering (DA-S).

The DC-S and RF-S modes are the most commend used in research because of the number of references they have for numerous materials. The DC-S mode only applies when the targets are made of conductive materials. On the other hand, the RF-S mode is applicable for nonconductive or low conductivity targets.

The significant advantage of magnetron sputtering is its ability to deposit a wide range of films on a complex topography of samples, making the process quite flexible. However, it is flawed in the low rate of ionization; only about 1% of the target species is sprayed ionized [4].

The equipment I worked on uses 4 inches targets. Different sets of parameters including pressure (0.1 - 0.001 mtorr), temperature (22 - 300°C), target power (RF mode) (30 - 80 watts) and time (10 min - 2.5 hours) have been investigated to optimize the layer properties. The substrate is first prepared on the holder plate. This part includes adding a physical mask to localize the area where the material has to be deposited: as the behavior of some materials, i.e., La_2CuO_4, is almost not known, a physical mask has been preferred to a lithography mask in order to avoid any complementary chemistry link to photoresist handling. The holder plate is then inserted into the transfer chamber. Automation transfers the plate into the deposition chamber under the right target position since there are different targets in the chamber.

For the fabrication recipe, it initializes by conditioning the pressure of the fabrication chamber with an Ar (10 sccm) flow through it. When chamber pressure is stabilized, the plasma ignition can take place under a closed shutter condition (this part is essential to check the ignition of the plasma and then to clean the surface of the target from any contamination that could have been caused by deposition of other materials in the same chamber). Finally, the sputtering starts by opening the shutter. A rotational movement of the sample holder is done to ensure homogeneous deposition (Fig. 37).

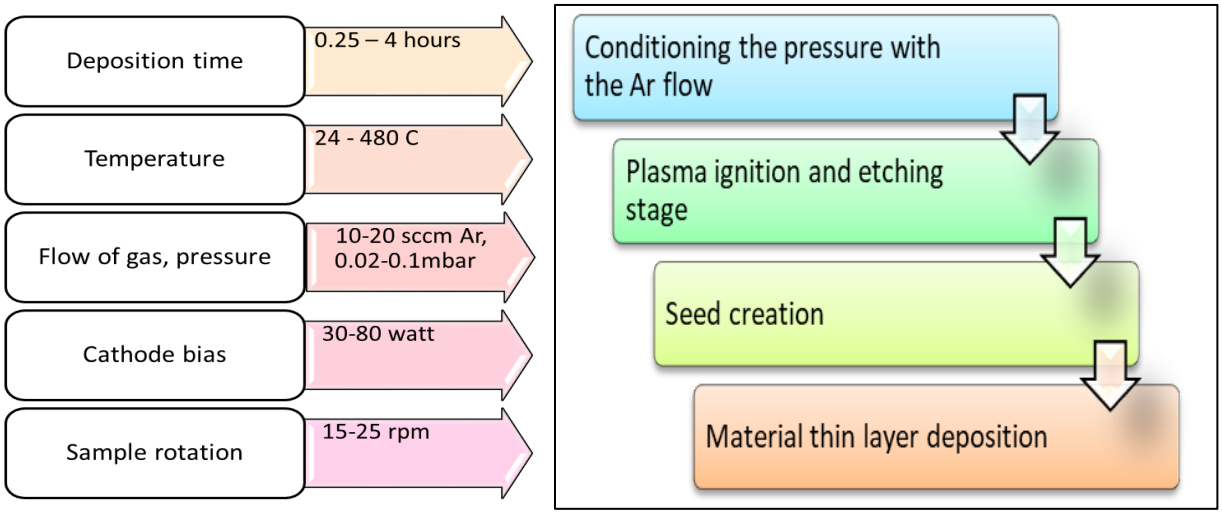

Figure 37: used parameters and the main steps of the sputtering deposition process.

For, respectively, La_2CuO_4 and AZO, RF-S, and DC-S modes were used with noticing the considerable variation in deposition velocity between the two modes. Also, we add a step to create seeds of the same material to reach more crystallized layers.

3.2.2 *Plasma laser deposition (PLD) (used in KAUST)*

Pulsed laser deposition (PLD) has been used in the second approach since it can create the intended quantum dots for the designed solar cell on the contrary to the previous technique that is more suitable for creating thin films.

The basic phenomenon of PLD is almost the same as the one used in sputtering in terms of extracting atoms from a target and depositing them onto a sample. Nevertheless, in this technology, atoms are extracted using energy issued from laser pulses, as shown in Fig. 38. Consequently, the target material is detached on an atomic or molecular level, depending on the material absorption properties.

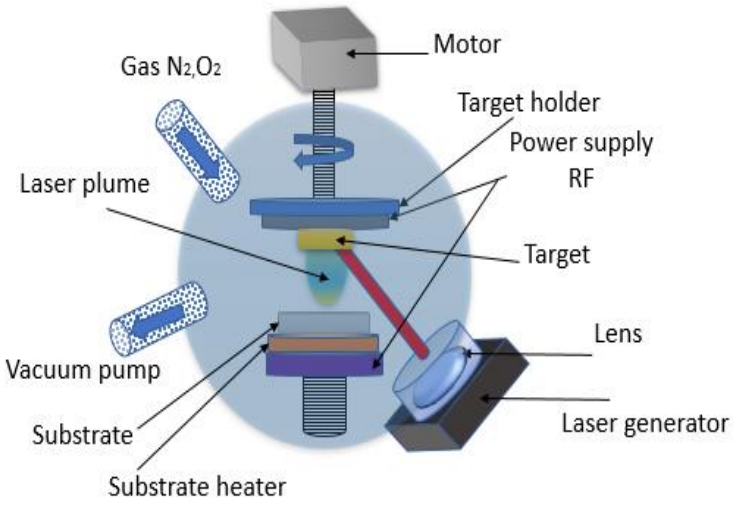

Figure 38: Pulsed laser deposition with substrate heating.

Thus, a laser pulse controlled in duration, repetition frequency, and power is focused onto the surface of a rotating target using lens and mirror configuration to ensure equal thermal distribution and a higher lifetime of the target. The focused beam vaporizes the surface of the target material and forms the ablation plume by the partially ionized ejected material, which is directed towards the substrate. The process occurs in a vacuum chamber with an introduced gas such as nitrogen or oxygen that enhances the deposition. Correspondingly, the threshold power required to create such a plasma depends on a few things, such as the absorption properties of the target material, the laser wavelength, and pulse interval.

Emblematic for excimer laser is a pulse of 10 ns; for femtosecond excimer lasers, it is around 500 fs. The detached material re-condenses on the sample to form a film and its growth kinetics depend on the material flux, repetition rate, growth temperature, substrate material, pressure, and background gas (vacuum, reactive) [5].

The targets used were the AZO (Aluminum doped zinc oxide) for the metal oxide layer and La_2CuO_4 for the active layer, so the same as for the sputtering method. That will allow a comparison of film structure and topography between those two deposition techniques that will be presented later.

The fabrication starts by preparing the substrate on the holder plate (the size and shape of the substrate must be arranged to meet the holder dimension since it needs to be clamped into it to ensure optimal temperature transfer); this operation is more delicate than for the sputtering machine. The process follows almost the same steps as sputtering deposition, i.e., installation of the sample in the transfer chamber, implementation of the desired deposition parameters in the system software, and positioning the sample holder plate into the main chamber under the target to be used. When the right conditions have met, the laser with the chosen frequency will start but with the shutter closed (until reaching the assigned power). The process flow is shown in Fig. 39.

The recipe starts by applying the conditioning pressure into the fabrication chamber and waits until the right temperature is reached (this is the primary time-consuming process). Next, a rotational movement of the target begins to make sure the laser hits as much as possible of the surface area of the target, giving more duration of use and proper deposition. After that, the laser pulses impact the target building the plum and material starts to be deposited. The sample is also rotating to homogenize deposition. In the end, when the process finished after sample temperature drops, it is retrieved out of the deposition chamber.

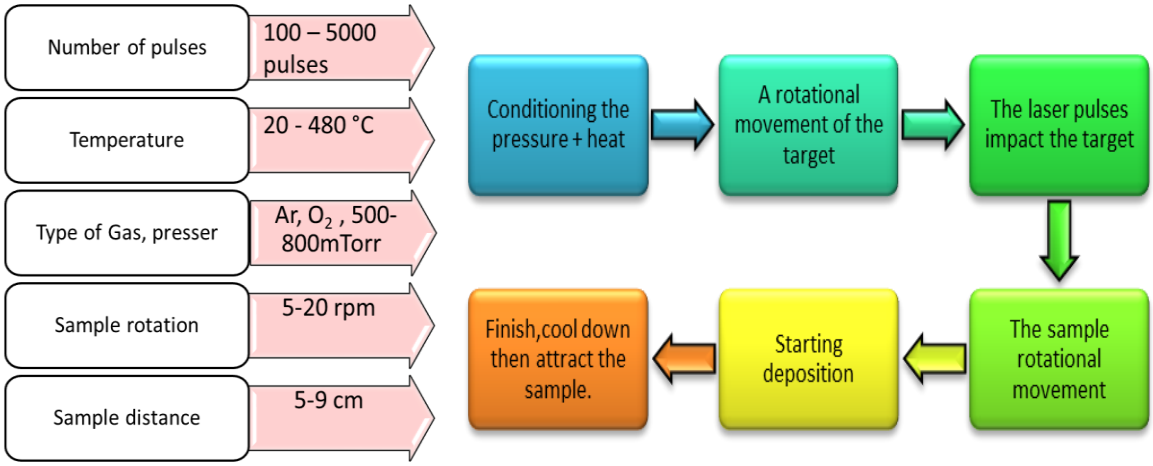

Figure 39: Main steps of the PLD deposition process and used parameters.

3.2.3 *Laser writing technique (used in KAUST and IEMN)*

The laser writing process is used to fabricate the so-called laser-induced graphene (LIG). This technique that does not require either high temperature that raises the entire cost of

the fabrication process or generate toxic chemicals as waste in the recycling stage appears to be a perfect method for our eco-green concerns.

In this method, the graphene is obtained by engraving the surface of polymers like Kapton (oxydiphenylene-pyromellitimide) by multiple laser pulses. The controlled irradiation induces the etching phenomena from a femtosecond laser beam that tailors materials properties and releases different gazes (Hydrogen, Oxygen, and Nitrogen) from the surface to convert it into laser-induced graphene (LIG).

One of the most successful applications of this technique is the ability to fabricate three-dimensional micro-devices integrating optical, mechanical, or fluid handling functions in a single substrate. [6]

The laser-induced method is easy and straightforward for obtaining graphene under ambient conditions on the surface of Kapton. The method of using multiple pulsed-laser scribing to convert a wide range of substrates into laser-induced graphene (LIG) is shown in Fig. 40. [7]

The LIG process starts with placing the Kapton sheet of a specific thickness (1 - 5 mm) on a holder plate within the laser machine and flattening it as much as possible since the focusing on the Kapton surface is critical for the resulting properties. When that has been done, a CO_2 laser beam is used for engraving. The different parameters that can be used in the optimization are the speed of beam sweeping (0.5 - 2 cm/s), the focal point size (0.1 - 0.5 mm^2), the Z-axis distance (1 - 3 cm), the pulse duration (10 – 40 microseconds) and its repetition frequency (0.1 - 10 kHz).

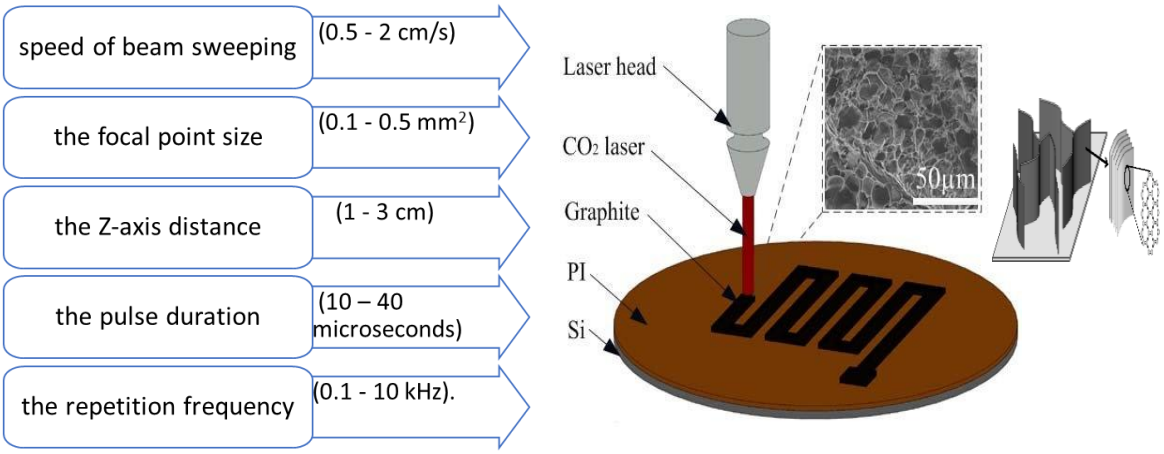

Figure 40: Serpentine graphite patterns as induced by the direct-write laser patterning process [7, 8].

3.2.4 *SILAR technique QDs of copper-indium-sulfur (CIS) (used in KAUST)*

The successive ionic layer adsorption and reaction (SILAR) technique is one of the chemical methods to deposit thin films and QDs using liquid baths on substrates.
It is schematically represented in (Fig. 41), employed for achieving copper-indium-sulfur (CIS) QDs.

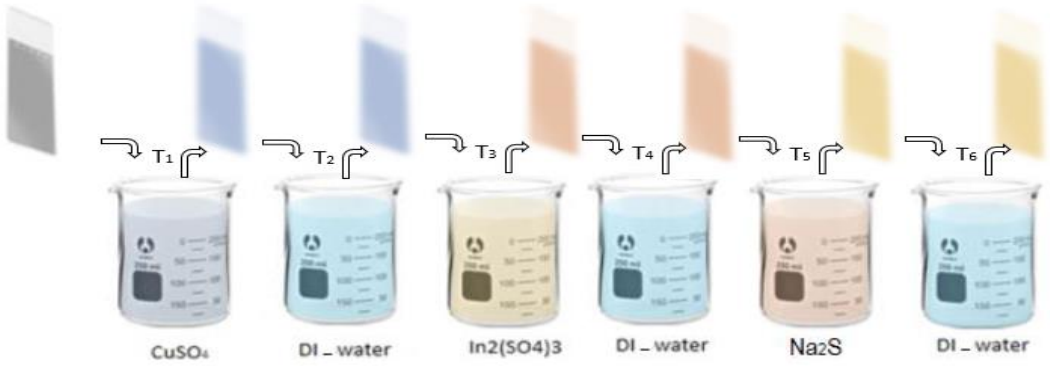

Figure 41: SILAR process to create QDs of copper-indium-sulfur (CIS).

CIS nanoparticle growth was carried out by the SILAR method using cupric sulphate "$CuSO_4$ " and indium(III) sulfate "$In_2(SO_4)_3$" as a cationic precursor and sodium sulfide "Na_2S" as an anionic precursor. The first cationic solution (solution A) was composed of **10.63 mg** of $CuSO_4$ dissolved in **10ml** deionized water and the second one (solution B) was composed of **34.49 mg** of $In_2(SO_4)_3$ dissolved in 10ml deionized water. On the other hand, the anionic solution (solution C) has a **5.20 mg** of Na_2S dissolved in 10ml deionized water.

solution A. $\mathrm{CuSO_4 + H_2O \rightarrow H_2O + (SO_4)^{-2} + Cu^{+2}}$

solution B. $\mathrm{In_2(SO_4)_3 + H_2O \rightarrow H_2O + 3(SO_4)^{-2} + 2\,In^{+3}}$

solution C. $\mathrm{Na_2S + H_2O \rightarrow H_2O + 2Na^{+1} + S^{-2}}$

For the CIS growth on the graphene substrate, it was immersed sequentially "all solutions are in room tempruture", into:
- solution A for **70** seconds
- deionized water for the **20s** (removal of non-attached or exceeded ions (Cu^{+2})),
- solution B for **70** seconds

- deionized water for another **20s** (removal of non-attached or exceeded ions (In^{+3})),
- solution C for another **70s**,
- deionized water for another **20s** (removal of non-attached or exceeded ions (S^{-2}))

Due to immersion in cationic solution ($CuSO_4$+$In(SO_4)$) a Cu^{+2} and In^{+3} ions are formed, and then react on the substrate with the S^{-2} ions of Na_2S and form the compounds of CuS and In_2S_3. With the process been repeated and characterized for **(1 - 5)** cycles to forme the CIS nanoparticles.

The reaction mechanism observed was:

$$2\ CuS + In_2S_3 \rightarrow 2\ CuInS_2 + S$$

Using SILAR has the advantages of low deposition temperature, which avoids high-temperature effects such as interdiffusion, contamination, and dopant redistribution. [11, 12]

3.2.5 *Chemical bath technique (used in KAUST)*

The ZnO layer has been synthesized using a solution of zinc nitrate "$Zn(NO_3)_2$" and hexamethylenetetramine "$C_2H_{12}N_4$" at the same molar ratios (**0.02** mol) diluted in (200mL) deionized water.

$$0.2\ \text{mol}\ Zn(NO_3)_2 \rightarrow 5.949\text{g of}\ Zn(NO_3)_2$$
$$0.2\ \text{mol}\ C_2H_{12}N_4 \rightarrow 2.804\text{g of}\ C_2H_{12}N_4$$

Those solutions are put within a beaker that has been placed into a thermo-regulated bath to maintain the temperature of the solution during it was mixed with a magnetic stirrer. Once the temperature reaches **95ºC**, the steering was stoped and the substrate was placed inside the solution for a period of deposition of **4**, **5**, and **6** hours. The process is illustrated in Fig.42. The active surface of the substrate was placed top-down in the solution.

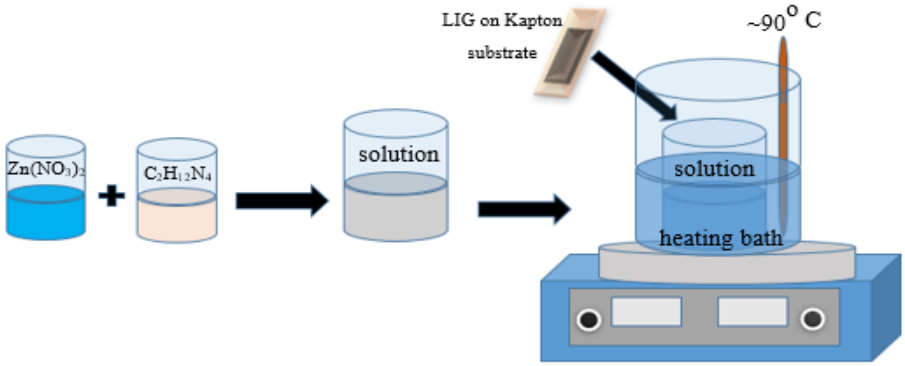

Figure 42: Schematic set up of chemical bath deposition method.

3.2.6 *Chemical Vapour Deposition (CVD) (used in KAUST)*

The development and improvement in the CVD process have been more rapid when for other thin film deposition technologies that have proved problematic or inadequate, for instance, in the production of multiple thin films, as in modern semiconductor devices, or when the coating of large surface areas is required, as in large-scale functional coatings on glass. The historical development of CVD processes and the published literature about started from the earliest 60s [9].

For this technology, the schematic of the growth chamber is shown in Fig. 43.

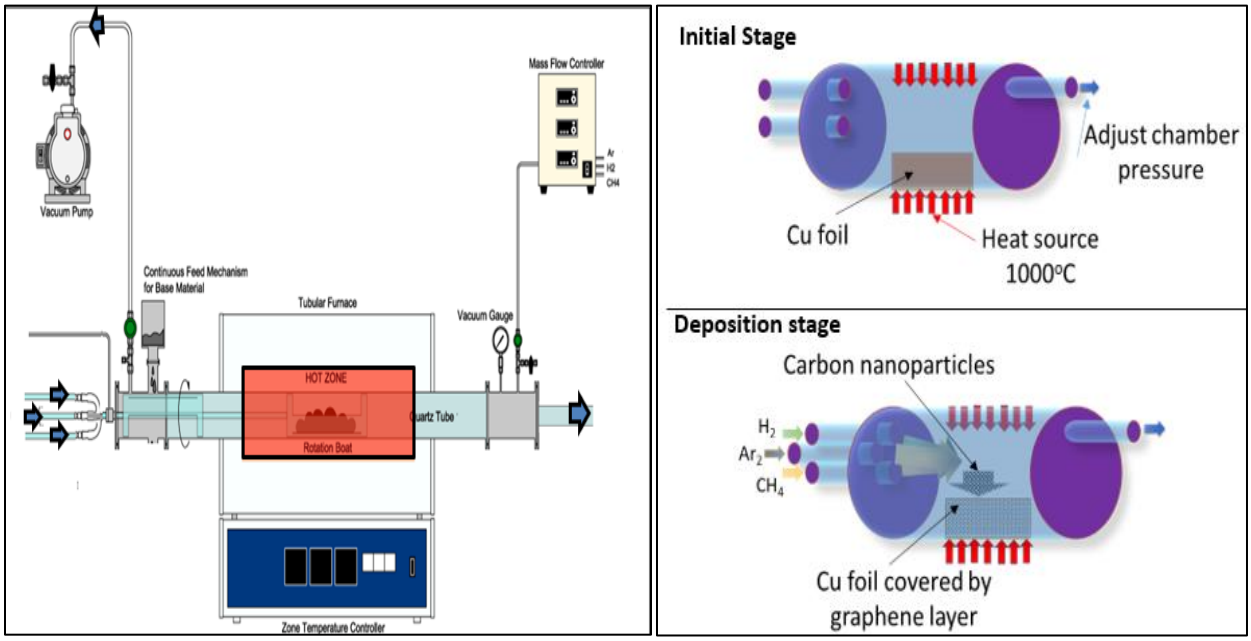

Figure 43: CVD process to produce a thin layer of graphene.

The CVD process initializes by placing and preparing the Cu foil in the quartz tube, then pumping down to 10^{-6} mbar pressure. When that pressure is reached, Ar gas is introduced into the chamber, which is followed by H_2 gas within minutes.

First, the process starts with an increase in the temperature of the deposition chamber once Ar and H_2 are introduced. Once the temperature is stabilized around 1000˚C, the Cu is annealed for around 10 min. Then at the same temperature, the growth of the graphene layer phase started by injecting CH_4 gas into the tube for 10 min continuously and jointly with Ar and H_2. The final phase consists of shutting down, in chronological order, the flows of CH_4, H_2, and last Ar and then turning off the heating to cool down gradually (the deposition chamber is kept closed during this step ensuring no fast cooling). Finally, when both pressure and temperature get to room values in the growth tube, the sample is removed.

After growth, the graphene sheets are exfoliated and transferred from Cu foil onto a Kapton or glass substrate in the following steps:

1. Adding a methyl methacrylate (PMMA) layer (thickness 200/300nm) on top of the graphene-coated Cu foil. PMMA is an acid-resistant polymer that is spin-coated over the graphene sheet in a uniform thickness. This layer will protect the graphene layer from etching later on and help in handling the transparent, fragile graphene layer during its transfer.
2. Drying the PMMA in the oven in a sequence of
    a. Rising from 30°C to 90°C in 30 minutes.
    b. Holding temperature to 90°C for 30 minutes.
    c. Cooldown from 90°C to 30°C in 30 minutes.
3. In most cases, the CVD process creates a backside graphene sheet with poorer quality than the one on the topside. This sheet would prevent the etching of the Cu foil or damage the top one in the future steps, so a plasma etching (1min, O_2 25sccm, 50W, 100mTorr) is made on the backside of the Cu sheet to remove it.
4. At this step, the Cu foil has so the graphene sheet protected by PMMA on one side. In order to retrieve the graphene sheet (imbedded in the PMMA layer), the

Cu foil has now to be etched. That is achieved using an ammonium persulfate ($(NH_4)_2S_2O_8$) solution, an acid solution that is made of 4.56g $(NH_4)_2S_2O_8$ salt diluted in 100ml deionized water. The Cu foil is then gently deposited on the solution surface where it should be floating, graphene/PMMA side up. Care is taken that no solution comes over the foil on the PMMA side. It is left for 18 hours.

5. Fig. 44 illustrates the end of the Cu foil etching process. It is clear that the Cu foil is completely gone. Also, great care shall be taken grabbing the PMMA sheet and transferring it to deionized water picker to remove the traces of the acid.

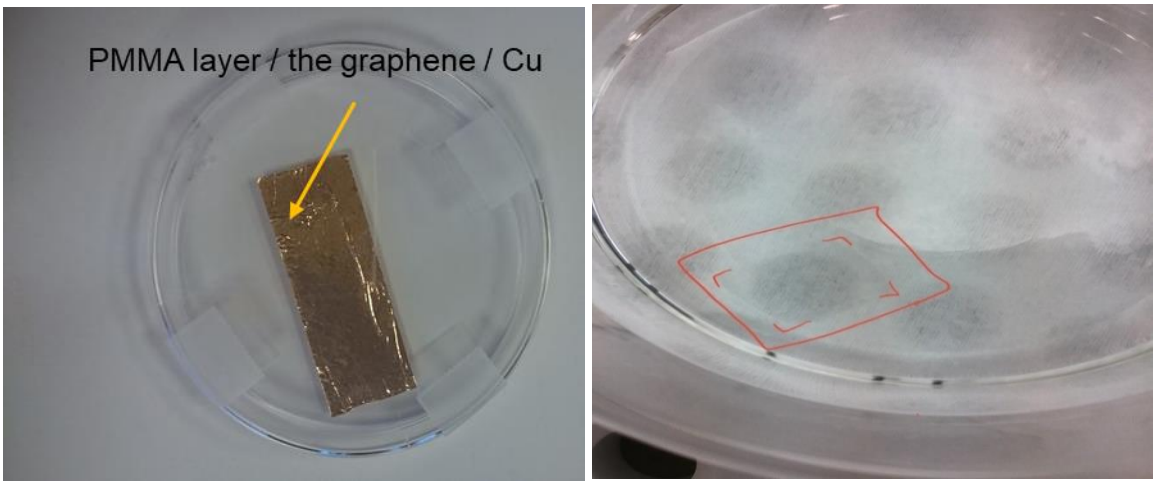

*Figure 44:*Graphene sheet embedded in the PMMA layer on top of etching solution before and after complete dissolution of the supporting Cu foil.

6. Then the PMMA sheet is very slowly transferred to the holding substrate, for example, Kapton, and placed to the right location.
7. The same drying process as in step 2 is made to dry and get all bubbles out between the graphene and the Kapton.
8. PMMA is then deep UV exposed at 500 J/cm^2 and for at least 30 minutes.
9. Then an acetone bath at 30°C during 30min, avoiding direct acetone flow, is used to remove the insulated PMMA. A very gentle N_2 drying is finally done.

3.3 1st approach: 3D structure

The 1st approach, as mentioned earlier, will test the capability of fabricating the design on a flexible material like Kapton (in light orange color) using two sequences. The first one using PLD is illustrated by steps B to D on Fig. 45. The second one using wet techniques is illustrated by steps B2 to D2 on the same figure.

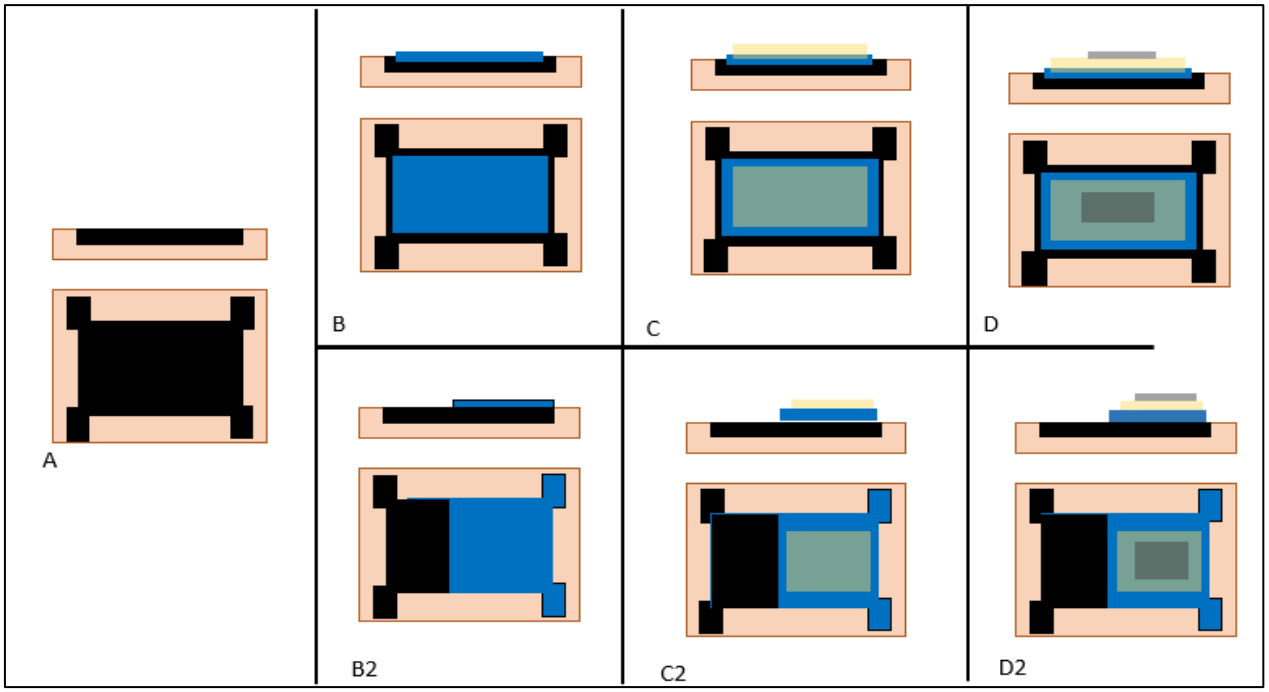

Figure 45: Side and top view of the two fabrication schemes that have been used; B to D using PLD and B2 to D2 using a chemical deposition.

The starting step in both sequences is the use of the LIG (represented by black color in Fig. 45.A) as the back electrode, the shape and design of the engraving on Kapton were chosen for later measurements and characterizations such as Hall effect. Keeping in mind that the Kapton substrate can handle temperature no more than 450 °C will imply a limitation to the deposition of MO or active layers materials that come later.

For the PLD based process (steps B-D), the sample and the first physical mask are clamped together in a metallic framework to deposit a thin layer (300 nm) of AZO (represented by the blue color in Fig. 45.B) by PLD. Moreover, the first physical mask preserves the four corners of LIG from the deposition as they would be used as a contact back electrodes. After that, a second physical mask is placed with a narrower opening window for the deposition of the La_2CuO_4 material (represented by the light yellow color)

shown in Fig. 45.C. Multi samples were made to have QDs with a diameter of 10 - 20 nm. Finally, the transparent graphene sheet (1-3 carbon layer) is placed as a top electrode (represented by the gray color) shown in Fig. 45.D.

For the chemical deposition based process (steps B2-D2), the Kapton substrate with the LIG electrode undergoes a chemical bath step for the deposition of a layer of ZnO nanorods (represented by the blue color in Fig. 45.B2). For the same reason, a part of the LIG electrode would be shielded from the deposition. After adding a physical mask to the sample, another wet technique would follow the SILAR to synthesize the QDs of CIS creating the active layer (represented by the light yellow color Fig. 45.C2). In the last step, a transparent graphene sheet is transferred on the QDs as a top electrode (represented by the gray color) shown in Fig. 45.D2.

3.4 2nd approach: Thin Film (2D) structure

The subsequent thin film layers are deposited in a sequence (A – F) (Fig. 46).

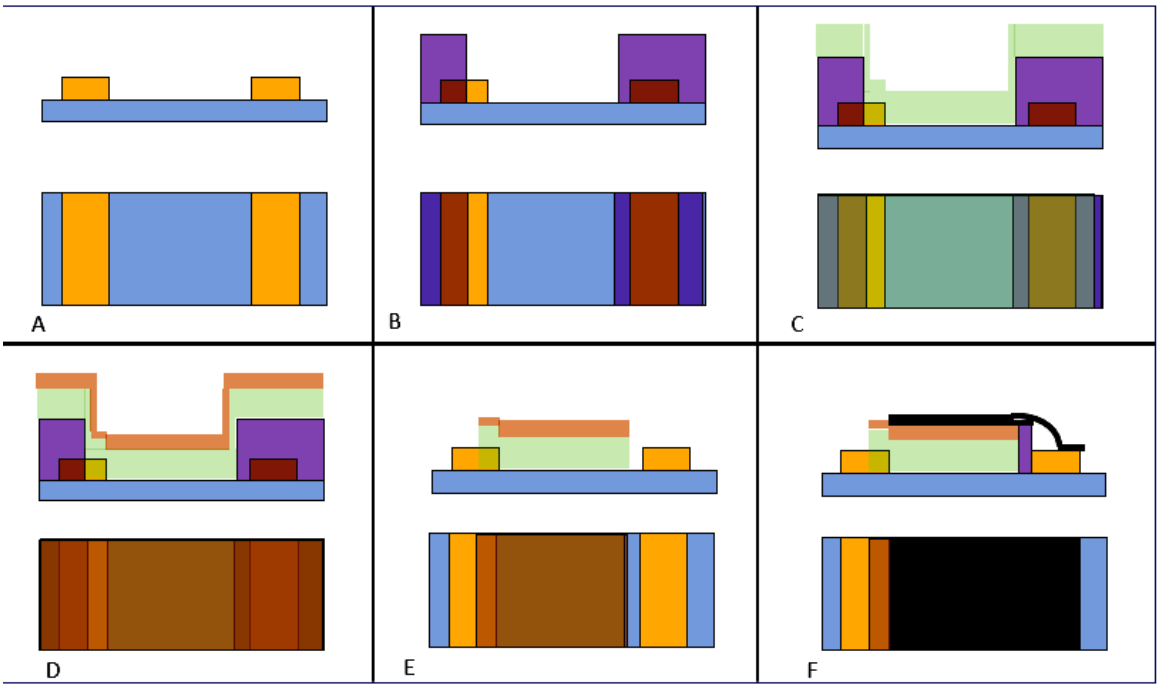

Figure 46: Side and top view of the sequence of second approach side / top views.

Starting from (Fig. 46A) by depositing a thin layer (300nm) of highly conductive, good attaching and chemical resilient metal (Au) (represented by the yellow color Fig. 46.A) on

a glass substrate (represented by the blue color Fig. 46.A). Patterns define two coplanar pads that will be used afterward as connecting pads. (Note that the glass substrate was the reference for the absorption measurements.) The second step (Fig. 46.B) consists in defining the surface area where the MO will be deposited. Resist (PMMA) has been used as well as a physical mask that was introduced later on in order to avoid the chemicals used in lithography (represented by the purple color). Next (Fig. 46.C), a layer of MO (Aluminum doped Zinc Oxide “AZO”) with a thickness of 200nm is deposited using sputtering technique (represented by the light green color) [10]. Sputtering was used at this stage because of its broad coverage of the surface of the sample. After that, the active absorbing layer (La_2CuO_4) is deposited using the same technique, with a thickness of (10 - 50 nm) (represented by the light orange color in Fig. 46.D). The final treatment of the sample consists of removing the unwanted parts using a lift-off technique (Fig. 46.E) and realizing the top electrode as well as its connection to one the pad deposited during the first step by transferring a graphene layer (represented by the black color Fig. 46.F).

3.5 Conclusion

In this chapter, we presented different deposition techniques. They are based either on physical or on chemical processing, and they are shared in between the two institutions I worked in. I also presented the different processes that are linked to those techniques and that I used to fabricate the demonstrators that are presented in the next chapters. Those demonstrators have been split into two categories, 2D and 3D structures, whose process has been schematically described.

References

1. polygonphysics. 2016 Nov 7]; Available from: https://www.polygonphysics.com/applications/ion-beam-sputter-deposition/.
2. Anders, A., *A structure zone diagram including plasma-based deposition and ion etching.* Thin Solid Films, 2010. **518**(15): p. 4087-4090.
3. Bunshah, R., *3.1 mechanical properties of PVD films.* Vacuum, 1977. **27**(4): p. 353-362.
4. Mattox, D.M., *Handbook of physical vapor deposition (PVD) processing*. 2010: William Andrew.
5. Schneider, C.W. and T. Lippert, *Laser ablation and thin film deposition*, in *Laser Processing of Materials*. 2010, Springer. p. 89-112.
6. Pépin, C.M., et al., *Silicon formation in bulk silica through femtosecond laser engraving.* arXiv preprint arXiv:1806.10802, 2018.
7. Wu, Y., et al., *Piezoresistive stretchable strain sensors with human machine interface demonstrations.* Sensors and Actuators A: Physical, 2018. **279**: p. 46-52.
8. Chuang, A.T., et al., *Three-dimensional carbon nanowall structures.* Applied physics letters, 2007. **90**(12): p. 123107.
9. Jones, A.C. and M.L. Hitchman, *Overview of chemical vapour deposition.* Chemical Vapour Deposition: Precursors, Processes and Applications, 2009: p. 1-36.
10. Ayachi, B., et al., *Rapid thermal annealing effect on the spatial resistivity distribution of AZO thin films deposited by pulsed-direct-current sputtering for solar cells applications.* Applied Surface Science, 2016. **366**: p. 53-58.
11. Cahen, D., et al., Ternary Chalcogenide-Based Photoelectrochemical Cells: IV. Further Characterization of the Polysulfide Systems. Journal of the Electrochemical Society, 1985. 132(5): p. 1062.
12. Xiao, J., et al., Synthesis and characterization of ternary CuInS2 nanorods via a hydrothermal route. Journal of Solid State Chemistry, 2001. 161(2): p. 179-183.

Chapter 4

Characterizations and Results

4.1 Introduction

This chapter is going through the characterization techniques used to examine and identify the experimental work presented in the previous chapter. Subsequently, we will report on the results of the growth of QDs materials, MOs and graphene layers by different processes or techniques. The results on those layers will be studied in a combination base on their arrangement in the design of a solar cell to have a full perception of the effect of each layer on its surroundings. Indeed, as previously mentioned, each layer growth process can act like a physical or chemical etching for the preceding layers and the crystallographic state of a deposited film can be linked to the substrate or the prior layer that can lead to the growth of unwanted or defected structure.

During the fabrication and the characterization processes, I did most of the experiments after the required training had been done. Some of the characterizations were achieved under the help of permanent staff in IEMN or KAUST since the required equipment was used only a few times or its use limited to specific engineers or technicians.

4.2 Characterization tools and techniques

4.2.1 *Optical characterization*

The identification of the optical properties of the deposited films is a significant factor in understanding the material and device behaviors. In this thesis, optical characterization is applied to seize data about atomic and molecular energy levels, structural geometries, chemical bonds, interactions of layers and spectrum absorption. Furthermore, spectrum absorption is used to identify and compare the properties of synthesized layers in a sample (qualitative analysis) or it may as well be used to measure the thickness of material in a sample (quantitative analysis).

Ultraviolet-Visible (UV-Vis) spectroscopy is beneficial to characterize materials. The absorption, transmission, and reflectivity properties obtained on materials, such as dyes and coatings are of prime interest for solar materials.

Absorbance spectroscopy, commonly referred to as spectrophotometry, is the analytical technique based on determining the amount of light absorbed by a sample at a given wavelength. Spectrophotometry, mainly in the visible and UV parts of the electromagnetic spectrum, is one of the most versatile and widely used techniques in chemistry and life sciences. Molecular absorption spectroscopy is concerned with the measured absorption of radiation in its passage through a gas, a liquid or a solid. The wavelength region generally used is from 190 to about 1000nm and the absorbing medium is at room temperature. [1]

The tested sample can possess one of a set of discrete amounts (quanta) of energy defined by the laws of quantum mechanics. These quantities are called the "energy levels" of that material. Moreover, the significant energy levels are determined mainly by the possible spatial distributions of the electrons and are called electronic energy levels, and to a lesser extent, by vibrational energy levels, which arise from the various modes of vibration of the material. [2, 3]

The energy and wavelength of absorption are defined by the difference between energy levels of an electronic transition. The following equation can express this relation:

$$\lambda = \mathrm{h\,C}/\Delta\mathrm{E}$$

where ΔE is the difference in the energy levels in the material (usually known as bandgap energy),

h (Planck's constant) = 6.626×10^{-34} Joules.sec,

C (velocity of light) = 2.99×10^{8} meter/sec.

If all transitions were between only the lowest vibrational levels of the ground state and the first excited state, then an absorption spectrum would consist of a narrow, discrete peak. However, the transition from one electronic level to the next level can occur between many vibrational levels. [4]

Since energy between vibrational levels within an electronic level is slightly small compared to the minimum energy between electronic levels, the electronic transition consists of a cluster of very closely spaced spectral peaks. Every peak has a significant

width, comparable to the spacing between the peaks. Consequently, all those peaks overlap together within a single broad peak, called an electronic absorption band. [4]

(Fig. 47) illustrates the connection between the energy transitions in the energy level diagram (Fig. 47.a) and the corresponding absorbance spectrum (Fig. 47.b). Low energy transitions are also possible between vibrational levels within a single electronic level. These transitions produce radiation in the infrared range.

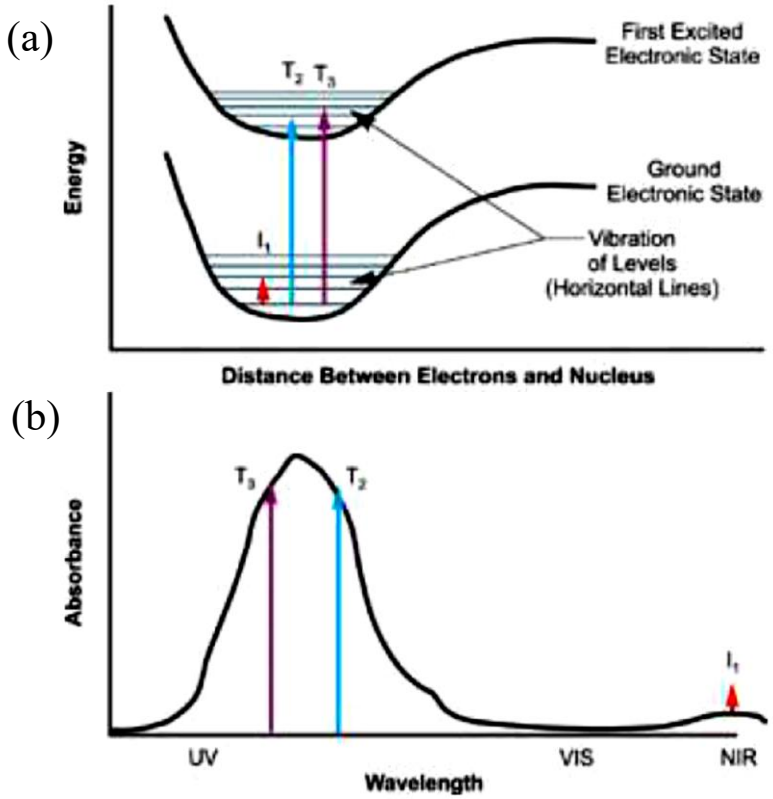

Figure 47: a) energy transitions in the energy level diagram, b) corresponding absorbance spectrum [5].

Lambert-Beer's law can describe the absorption of light in a suitable concentration range,

$$\boldsymbol{A} = -\log \boldsymbol{T}\%$$

Simplifying the equation by assuming that I_0, the initial incident spectrum intensity, is equal to 100%:

$$\boldsymbol{A} = -\log\left(\frac{\boldsymbol{I_T}}{\boldsymbol{I_o}}\right) \rightarrow -\log\left(\frac{\boldsymbol{I_T}}{\mathbf{100}}\right) \rightarrow = -\left(\log(\boldsymbol{I_T}) - \log(\mathbf{100})\right)$$

$$\boldsymbol{A} = \mathbf{2} - \log(\boldsymbol{I_T})$$

Using the absorption graph to get the value of E_g using the Tauc relation which is given by the equation:

$$\alpha h\nu = A\,(h\nu - E_g)^n$$

where α is the absorption coefficient given by:

$$\alpha = A/thickness$$

$$h\nu(eV) = 1240 / (incident\ wavelength\ (nm))$$

On the graph (Tauc plot) representing $(\alpha h\nu)^{1/n}$ versus $(h\nu)$, the intersect of the tangent to the curve with the X axis gives an evaluation of the value of E_g.

The value of n is dependent on the electronic transition type:

- n=1/2 for direct allowed transition (as exemple shown in Fig. 48),
- n= 2 for indirect allowed transition,
- n=3/2 for direct forbidden transition,
- finally n=3 indirect forbidden transition.

Note that the selection of the suitable n is according to the samples and their preparations. [6-8]

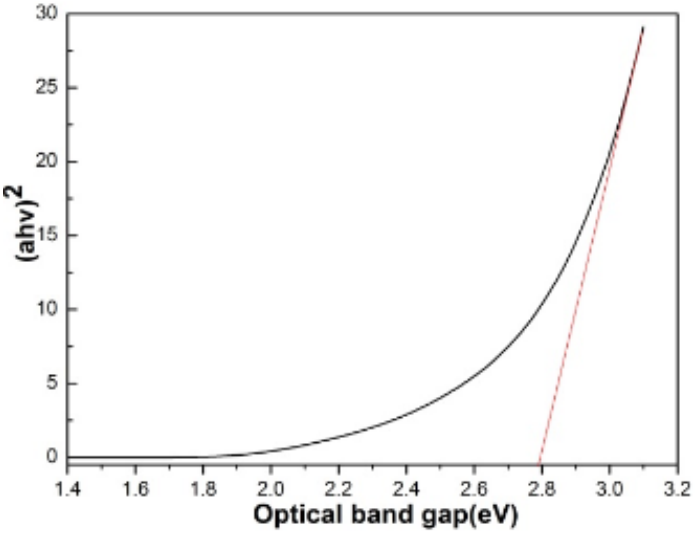

Figure 48: Example of Tauc plot for determination of optical bandgap [6].

4.2.2 *Electrical characterization*

The electrical characterization is one of the difficult tasks that is needed in judging how efficient the energy conversion process is for a given cell. The essential technique is the measurement of current-voltage curves under illumination (usually AM1.5G solar spectrum is used for that). Although the measurement itself is relatively simple, the conditions on how measurements should be carried out are not as simple and will be discussed. Other essential parameters are external and internal quantum efficiency values. Those provide information on how efficient is the conversion of light into electrical current is for photons of a specific wavelength. Spectrally resolved quantum efficiency measurements can help therefore providing information on the contribution of the materials in the solar cell to the energy conversion process. [9]

4.2.2.1 I-V curve

The measurements of the electrical current versus voltage (I-V) curves of a solar cell provide an essential piece of data. Initial with the existing of solar cell functionality, a junction has to be realized. If a solar cell is indeed achieved then collecting parameters such as the short circuit current (I_{sc}), the open-circuit voltage (V_{oc}), the maximum current (I_{max}) and voltage (V_{max}) at the maximum power P_{max}, the Fill Factor (FF), and the energy conversion efficiency of the cell (η) would be possible, they have been explained in chapter two (see Fig. 4 in §.1).

Performing the I-V test on the designed solar cell, a Kelvin configuration is used that includes a four-wire connection. These connections are referred to as source leads, and sense leads. [10]

The current flows through the source leads and the cell under test, and the voltage across the device is measured by sense leads. Since the input impedance of the sense leads is very high, the source current will not flow through the sense leads and, therefore, only the voltage across the device is measured. By comparison, if a simple two-wire connection was used to take the I-V data, the current flowing through the leads will cause a voltage drop in the leads in addition to the potential drop across the device; hence, the voltage

measurement across the circuit will not be that of the voltage across the cell. This effect can be particularly significant for larger area solar cells where a large photocurrent is generated in the cell under illumination. With this large current, the voltage drop due to lead resistance will be more significant, hence pointedly altering the shape of the I-V curve.

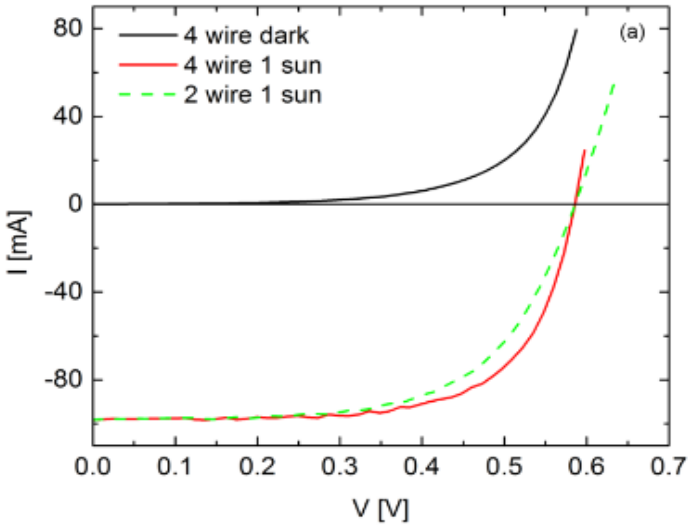

Figure 49: Comparison between two-wire and four-wire I-V measurements on a small 4 cm^2 solar cell [10].

The curve (Fig.49) shows the four vs. two-wire I-V curve data for a 4 cm^2 Si solar cell under 1 sun illumination intensity. In a 2-wire test configuration, the parameter that is more noticeably affected is the FF, showing a slight reduction. This reduction impacts the measured power conversion efficiency of the device, although the I_{sc} and the V_{oc} are relatively unaffected. [10]

4.2.2.2 Hall Effect

The Hall Effect was discovered in 1879 and is considered as one of the essential sources of the determination of conduction properties of semiconductor materials and thin films. When a conducting material with current passing through is placed into a magnetic field, an electric field will be induced. The direction of this electric field is normal to both the magnetic field and current directions. [11]

The Hall measurement is valuable since it gives the resistivity, mobility, carrier concentration of the measured semiconductor as well as its polarity. Different sources as

the impurity content, quality and homogeneity of the epitaxial layer affect the mobility. Resistivity is the proportional relation between the electric field and the current density.

The basic theory of the Hall Effect rises from the nature of conduction where current consists of the flow of charged particles (electrons) drifting under the influence of an applied electric field. The velocity at which these carriers will flow is called the drift velocity and is denoted as (v). Carriers will flow in the direction of the applied electric field (holes) or the opposite direction of the applied electric field (electrons). The magnitude of the drift velocity depends on the applied electric field strength (E) versus the respective carrier type mobility and tends to saturation at high electric fields.

There are many configurations to conduct the Hall Effect test; the most efficient arrangement is known as the Van Der Pauw protocol. In Van Der Pauw measurements, the hypothesis is that the samples are flat, homogeneous, isotropic and of uniform thickness. This will insure to give accurate readings, like the ones we made on the PVD or PLD deposited films. Making the measurements, a simple way contacting the different materials consists in making point-like contacts by small indium balls that are melted on the samples. One can note that it would be right as a tactic not to let the size of the contact exceed 10% of the size of the smallest sample dimension. [12]

To comprehend how the Hall Effect is measured, see Fig. 50.

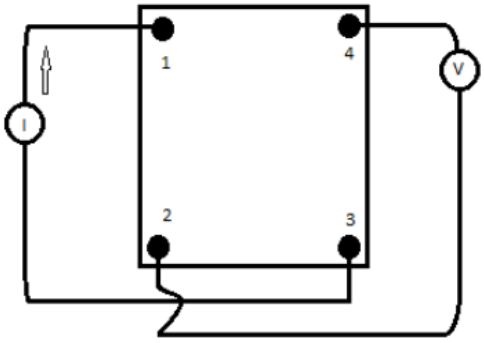

Figure 50: Contact configuration for Hall measurements using a square sample [13].

4.2.3 *Structural characterization*

Particularly investigating materials of nanometric scale, Scanning Electron Microscopy (SEM) and Atomic Force Microscopy (AFM) are both fascinating tools to visualize and

give feedback about the grain size and the deposition mechanism. As it has been mentioned in previous chapters, there is a relationship between the QD_S size and their light absorption properties.

4.2.3.1 Scanning electron microscopy

Invented by Manfred von Ardenne in 1937, the scanning electron microscope (SEM) utilizes electrons instead of photons to form an image. This microscope consists of an electron gun and a set of electromagnetic lenses to guide the electron beam toward the sample surface (Fig. 51). [14]

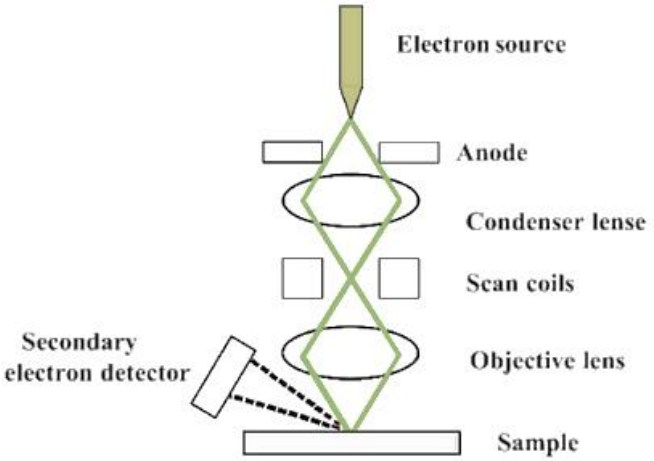

Figure 51: Scanning electron microscope (SEM) schematic [15].

Backscattered and secondary electrons received from the surface are collected by detectors and converted into a signal to produce the final image. Currently, the surface morphology of a thin film sample can be studied by the SEM because it has a much higher resolution and has a significant depth infield than a traditional microscope. On the other hand, in addition to the backscattered and secondary electrons from the sample surface, there are other types of signals produced during this process (Auger electrons, X-ray fluorescence photons, and others photons with various energies) that could be used for chemical analysis. [16]

During this thesis, we were using two SEM, the first one Zeiss Supra 55VP Field Emission Scanning Electron Microscope at IEMN and the second one FEI Magellan scanning electron microscope in KAUST.

4.2.3.2 Energy dispersive x-ray spectroscopy

Energy dispersive x-ray spectroscopy (EDX) can be used to show the local element composition and provide quantity compositional information over the sample. Here, it is implemented within the SEM equipment. This technique detects x-rays emitted from the sample during its bombardment by electrons to characterize the elemental composition of the examined volume. Features or phases as small as 1 μm or less can be analyzed.
In this work, the EDX spectra were used to identify the distribution of the composite materials after deposition using various technologies and make sure that the deposition took place where it should be.

4.2.3.3 Atomic force microscopy

The atomic force microscope (AFM) is often called the "Eye of Nanotechnology." as well referred to as SPM or Scanning Probe Microscopy was invented in 1986 by Gerd Binnig, Calvin Quate, and Christophe Gerber, they were awarded Nobel Prize in Physics for their invention. The AFM is made up of a flexible force-sensing cantilever scanning the top surface of the sample. [14] The force acting between the cantilever and the sample surface causes minute deflections of the cantilever, which are detected by an optical beam deflection detector (Fig. 52).

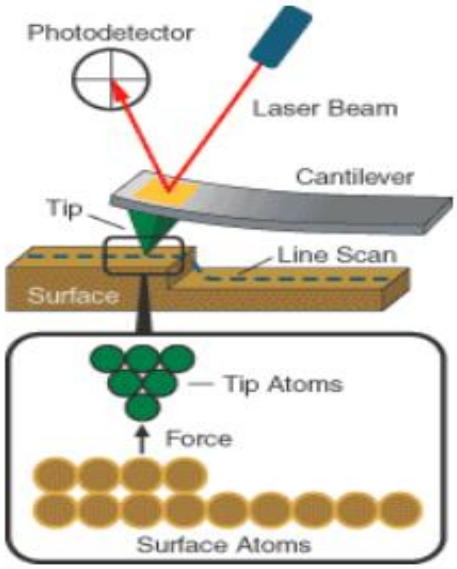

Figure 52: Atomic Force Microscopy schematic [17].

The efficiency of AFM images depends on the physical characteristics of the cantilever and the tip. At present, cantilever-tip assemblies are micro-machined from monolithic silicon with a tiny tip, ideally, with a single atom at the apex. The sample is positioned on a piezoelectric device that moves the sample along the three-axis under the tip. The signal from the laser beam detector is then fed back into the sample piezoelectric transducer, which causes the sample to move up and down, maintaining a constant force between the tip and the sample. There are three working modes in AFM:

- Contact mode

The tip and the sample could be damaged when the surface morphology of a solid sample is scanned, leading to scratches and may be injuries, especially if thin films or nanometric structures are involved.

- Tapping mode

The cantilever oscillates (few hundred kilohertz), in the way that the tip and the surface are in contact for a brief time, safer for the sample, not the tip.

- Non-contact mode

The tip floats a few nanometers above the sample surface, and the attractive van Der Waals forces flanked by the tip and the sample are detected. The safest mode, but the resolution is lower than those detected in contact-mode.

As shown in table IV below, AFM has several advantages over other techniques that make it a favorite among leading researchers. It provides readily available high-resolution and three-dimensional information in real space with little sample preparation for low-cost. In-situ observations, imaging in fluids, temperature, and environmental controls are all available.

Table IV: Comparison of Atomic Force Microscopy and other techniques [17].

	AFM	TEM	SEM	Optical
Max resolution	Atomic	Atomic	1's nm	100's nm
Typical cost (x $1,000)	100-200	500 or higher	200-400	10-50
Imaging Environment	air, fluid, vacuum, special gas	vacuum	vacuum	air, fluid
In-situ	Yes	No	No	Yes
In fluid	Yes	No	No	Yes
Sample preparation	Easy	Difficult	Easy	Easy

4.3 Electrode: Laser Induced Graphene/Graphite

Different types of laser scribing have been used to optimize (reduce) the LIG resistance and to study the effect of changing process parameters such as laser frequency, speed of engraving, focal length and energy. All of those changes have been made according to a matrix structure such as depicted in Fig. 53.a and detailed afterwards. Fig. 53.b shows a view of an interdigitated electrode structure. Fig. 53.c shows a Scanning Electrode Microscope view of the treated surface.

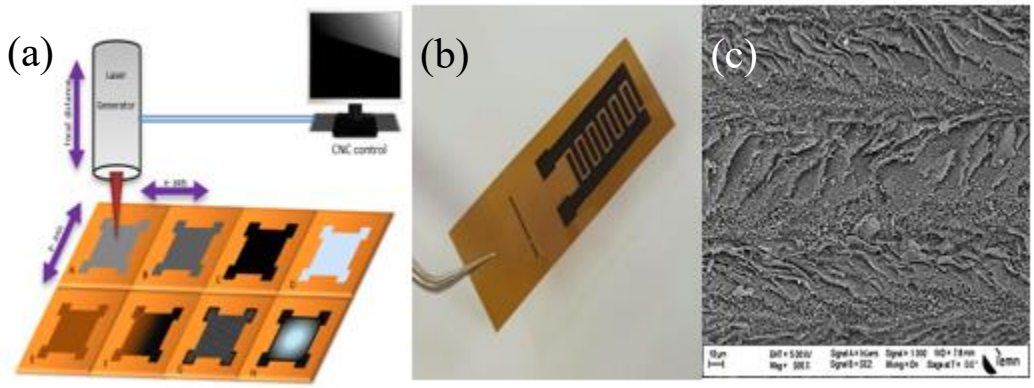

Figure 53: Laser-Induced Graphene: a) process with different results by changing the parameters, b) global pattern on the substrate" DuPont™ Kapton® polyimide film (***PV9100 SERIES***)", c) SEM image of the LIG substrate.

The process has been optimized to reduce LIG film resistance. It is obtained for the graphene sheets configuration shown in the next few figures. The technique has been used in both IEMN and KAUST.

The SEM picture (Fig. 54.a) reveals high symmetry in what appears to be sheets of graphene parallel to each other. The low charging effect that is observed under SEM that tends to indicate an excellent conductivity of the LIG.

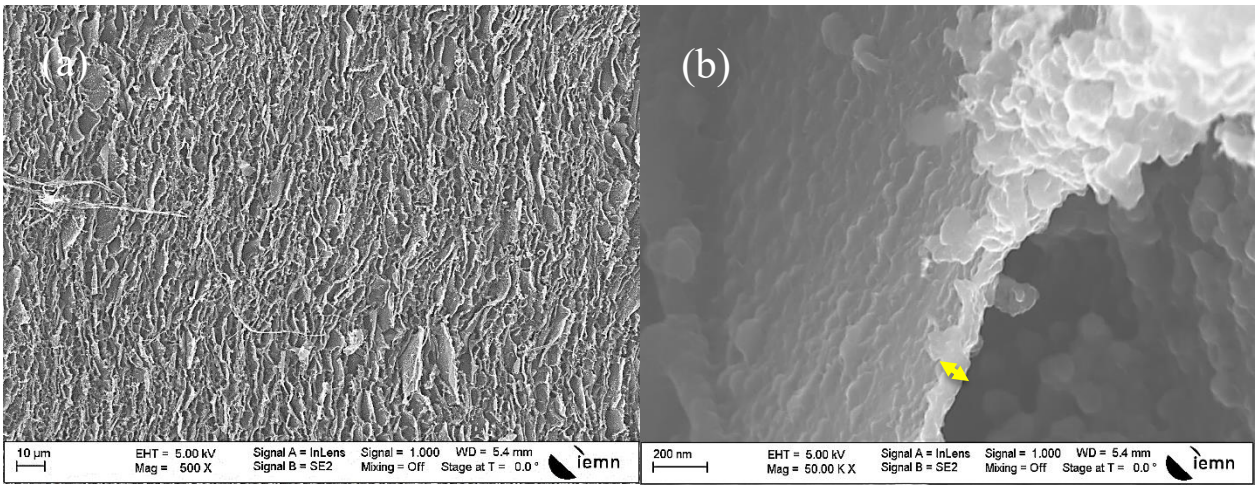

Figure 54: SEM images of Laser-Induced Graphene made in IEMN: a) top view 10 µm scale, b) one sheet in 200 nm scale.

Going to higher (Fig. 54.b) magnification (50K), the sheet thickness is estimated around 60nm. The charging effect is still very low.

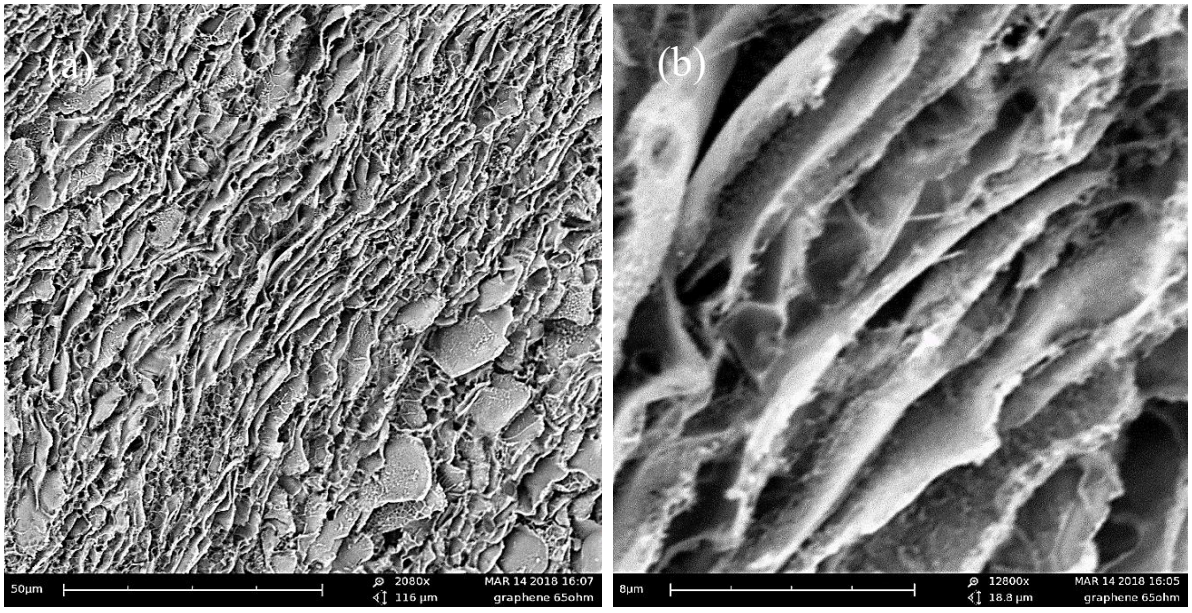

Figure 55: SEM images of the Laser-Induced Graphene made in KAUST: a) top view with a 50 µm scale, b) top view with an 8 µm scale.

The first trial to fabricate LIG was using the KAUST equipment. The SEM image (Fig. 55) illustrates the surface of the LIG on the Kapton substrate; it shows a randomly oriented aggregation of carbon sheets.

Comparing the two fabrication processes, in IEMN and KAUST, the sheet estimated thickness is almost the same using the same parameters.

A parametric study has been launched to optimize the LIG layer using different deposition parameters: type of laser used, UV or IR, power, and frequency of pulses.

The starting parameters used in the CNC machine (KAUST) are summarized in Table V, low power and UV laser are used. The corresponding sample is shown in Fig. 56.

Table V: First set of parameters using the UV-femtosecond laser system, maximum power = 2.6 Watt, frequency: 200 kHz.

Sample	Frequency (kHz)	Power (%)	Speed (mm/s)
1A	4	5	1
1B	4	15	1
1C	4	5	2
1D	4	15	2
1E	4	15	4
2A	10	5	6
2B	10	5	8
2C	10	10	8
2D	10	5	10
2E	10	15	10
3A	25	5	15
3B	25	5	20
3C	25	15	20
3D	25	5	25
3E	25	15	25
4A	50	5	15
4B	50	15	15
4C	50	5	20
4D	50	15	20
4E	50	5	30
5A	50	15	30
5B	50	5	40
5C	50	15	40
5D	50	5	50
5E	50	15	50

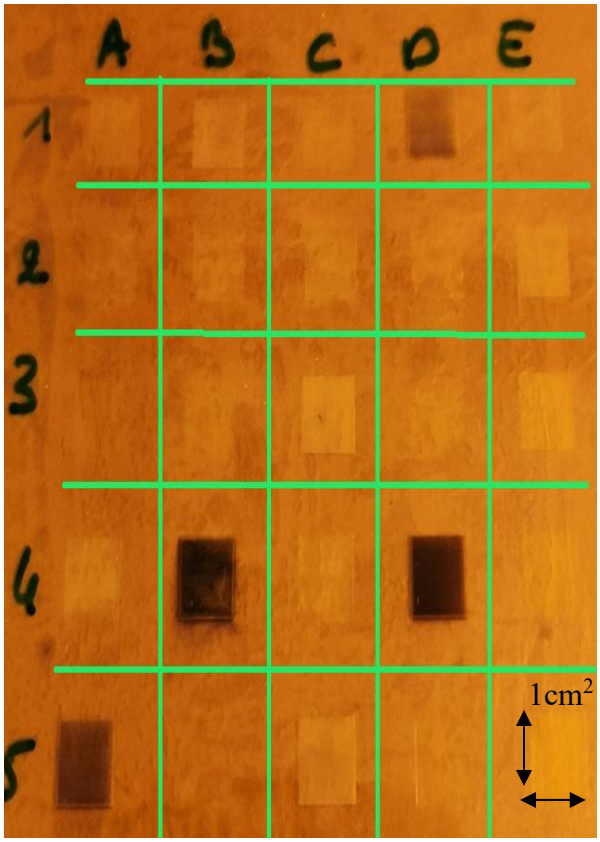

Figure 56: First set of LIG on Kapton substrate" (***PV9100 SERIES***)" fabricated using a UV femtosecond laser system Parameters are shown in Table V.

It has been noticed that only the "sample 4D" reveals a graphite structure on its surface, confirmed by the SEM image (Fig. 57). On the other hand, all remaining samples did not reflect any significant result in terms of graphite formation on the surface of the Kapton substrate.

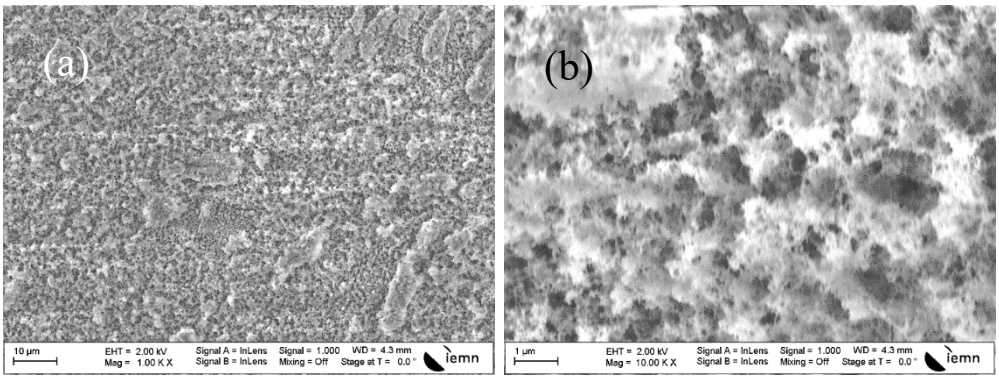

Figure 57: SEM images (IEMN) of Laser-Induced Graphene with UV femtosecond system: sample "4D" top view: a) 10µm scale, b) 1µm scale.

Based on this result, reflecting the best results for a power of 15%, a parametric study has been conducted changing the power and varying the frequency and the speed (Table VI).

Table VI: Second set of parameters using the UV-femtosecond laser system, maximum power = 2.6 Watt, frequency: 200 kHz.

Sample	Frequency (kHz)	Power (%)	Speed (mm/s)
1A	1	30	1
1B	1	50	1
1C	4	30	2
1D	4	50	2
1E	4	50	4
2A	10	30	6
2B	10	30	8
2C	10	50	8
2D	10	30	10
2E	10	50	10
3A	25	30	15
3B	25	30	20
3C	25	50	20
3D	25	30	25
3E	25	50	25
4A	50	30	15
4B	50	50	15
4C	50	30	20
4D	50	50	20
4E	50	30	30
5A	50	50	30
5B	50	30	40
5C	50	50	40
5D	50	30	50
5E	50	50	50

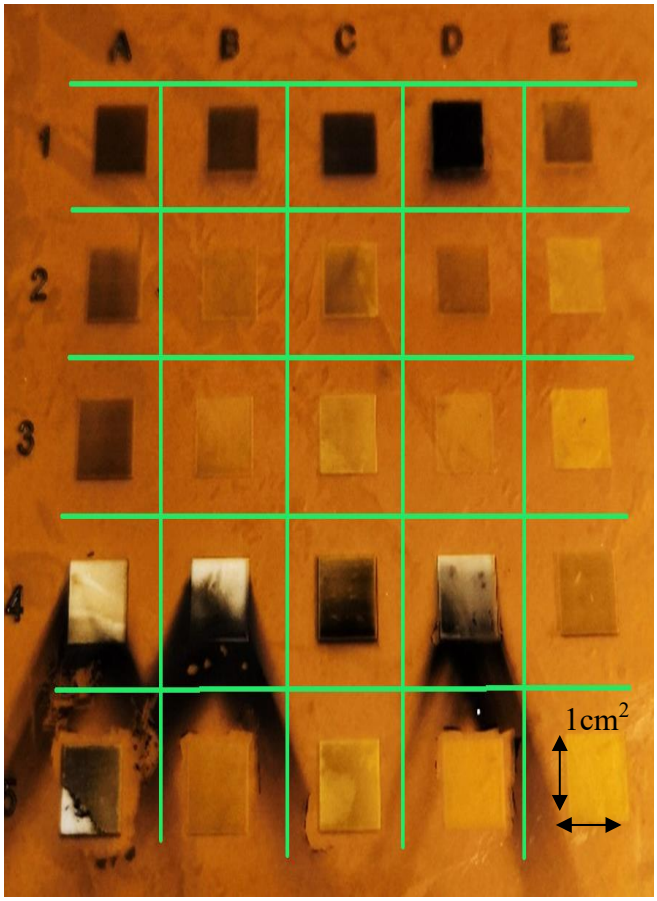

Figure 58: Second set of LIG on Kapton substrate" (***PV9100 SERIES***)" fabricated using a UV femtosecond laser system. Parameters are shown in Table VI.

As it can be noticed on the picture in Fig. 58 showing the Kapton film after writing, it was a failure to create graphite or graphene by these settings (no graphene were detected by SEM or conductivity measurement); an other parametric study has been launched using an IR laser source instead of the UV laser source.

The new set of parameters using now an IR laser in the CNC machine (KAUST) is summarized in Table VII.

Table VII: First set of parameters using the IR-femtosecond laser system, maximum power = 13.6 Watt, frequency: 200 kHz.

Sample	Frequency (kHz)	Power (%)	Speed (mm/s)
1A	200	5	20
1B	200	5	40
1C	200	5	60
1D	200	5	80
1E	200	5	100
2A	300	10	20
2B	300	10	40
2C	300	10	60
2D	300	10	80
2E	300	10	100
3A	400	100	20
3B	400	100	40
3C	400	100	60
3D	400	100	80
3E	400	100	100
4A	600	100	20
4B	600	100	40
4C	600	100	60
4D	600	100	80
4E	600	100	100
5A	800	100	20
5B	800	100	40
5C	800	100	60
5D	800	100	80
5E	800	100	100

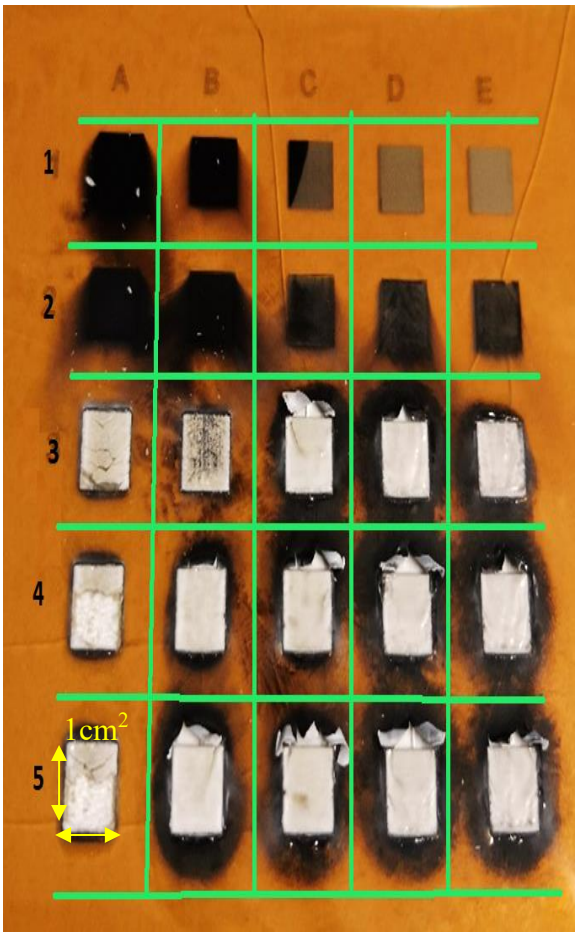

Figure 59: First set of LIG on Kapton substrate " (***PV9100 SERIES***)"fabricated by an IR femtosecond laser system. Parameters are in Table VII.

The use of IR femtosecond laser with those parameters allows creating graphite on samples (1A, 1B, 1C, and 1D) also with high resistivity. The rest of the samples, as shown in Fig. 59, was almost burned.

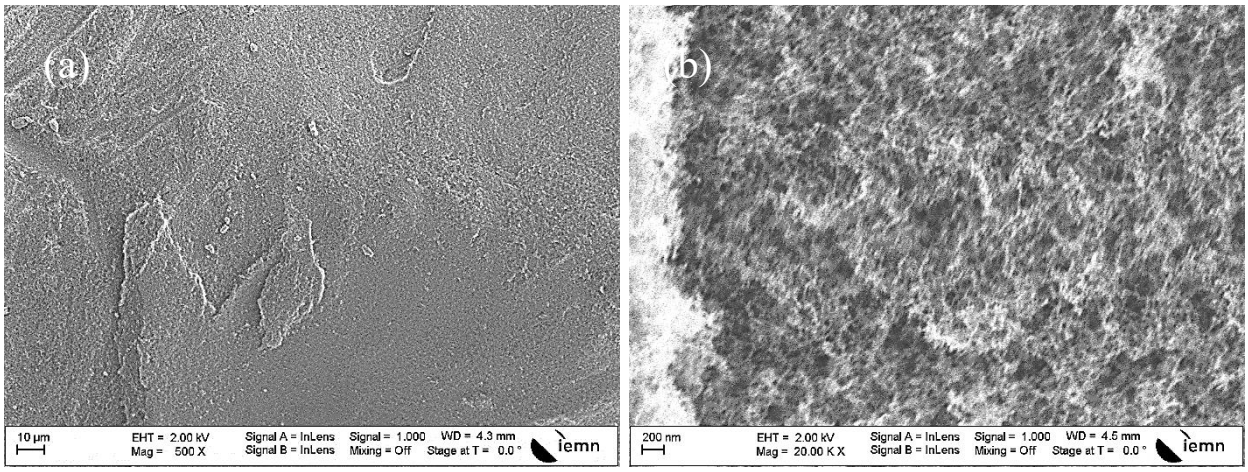

Figure 60: SEM images of Laser-Induced Graphene sample (1A) top view a) 10 µm scale, b) 200nm.

In Fig. 60, the surface topography of sample (1A) show randomly oriented nano-walls and some carbons nanoparticles.

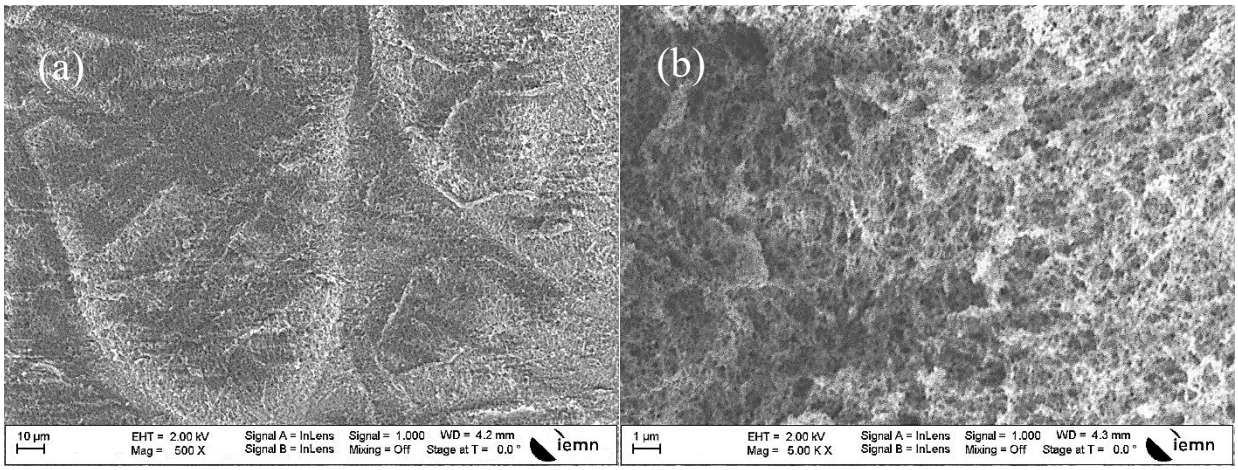

Figure 61: SEM images of Laser-Induced Graphene sample (1B) top view: a) 10 µm scale, b) 1 µm scale.

In Fig. 61, the surface topography of sample (1B) show more complex random oriented nanowalls, but a smaller quantity of carbon nanoparticles.

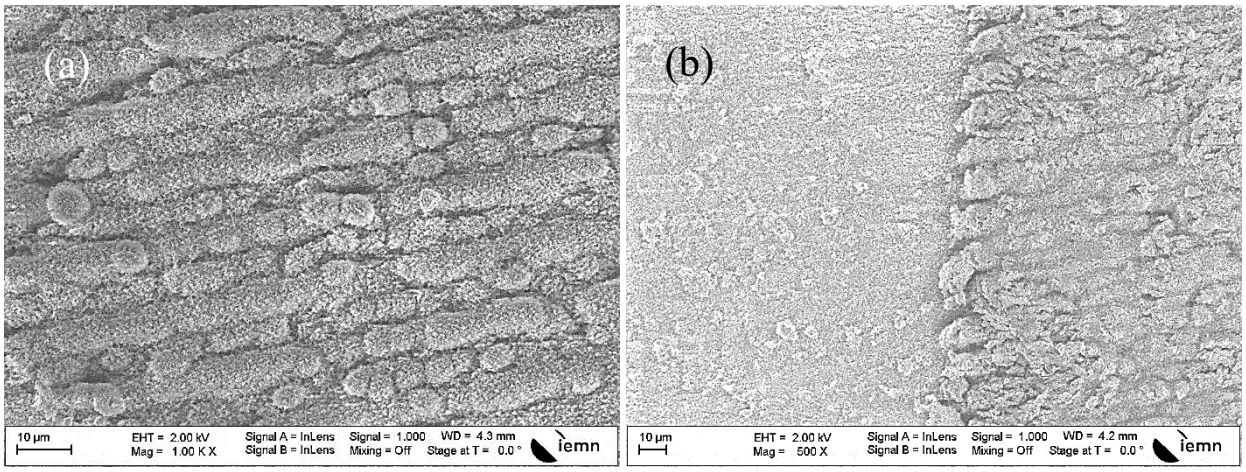

Figure 62: SEM images of Laser-Induced Graphene sample (1C) top view: a) center of the sample 10 µm scale, b) edge of the peeled part in a 10 µm scale.

In Fig. 62, most of the sample (1C) is peeled, but the remaining part shows micro-islands in different shapes and sizes as well as carbons nanoparticles.

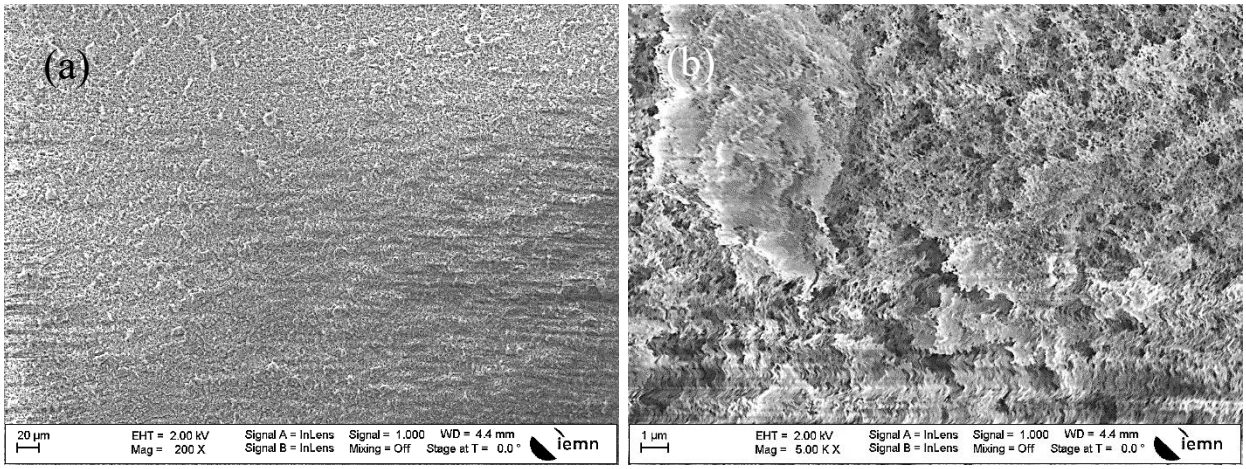

Figure 63: SEM images of Laser-Induced Graphene sample (1D) top view: a) center of the sample 20 µm scale, b) 1µm scale.

In Fig. 63, the samples (1D-1E) had no graphene layer, only sponge carbons aggregated nanoparticles after the original layer of graphene was peeled.

Based on the previous results reflecting the use of IR laser in a higher power (more than 10%), it was shown that the Kapton substrate was almost always destroyed. So the parametric study has been continued by diminishing to lower power values, from (1% to 8%) and varying the frequency and the speed of the engraving process.

The new parameters used in the CNC machine are summarized in Table VIII and the corresponding results are shown in Fig. 64.

Table VIII: Second set of parameters using the IR-femtosecond laser system, maximum power = 13.6 Watt, frequency: 200 kHz.

Sample	Frequency (kHz)	Power (%)	Speed (mm/s)
1A	200	1	10
1B	200	1	20
1C	200	1	30
1D	200	1	40
1E	200	1	50
2A	200	2	10
2B	200	2	20
2C	200	2	30
2D	200	2	40
2E	200	2	50
3A	200	5	10
3B	200	5	20
3C	200	5	30
3D	200	5	40
3E	200	5	50
4A	200	8	10
4B	200	8	20
4C	200	8	30
4D	200	8	40
4E	200	8	50
5A	200	10	10
5B	200	10	20
5C	200	10	30
5D	200	10	40
5E	200	10	50

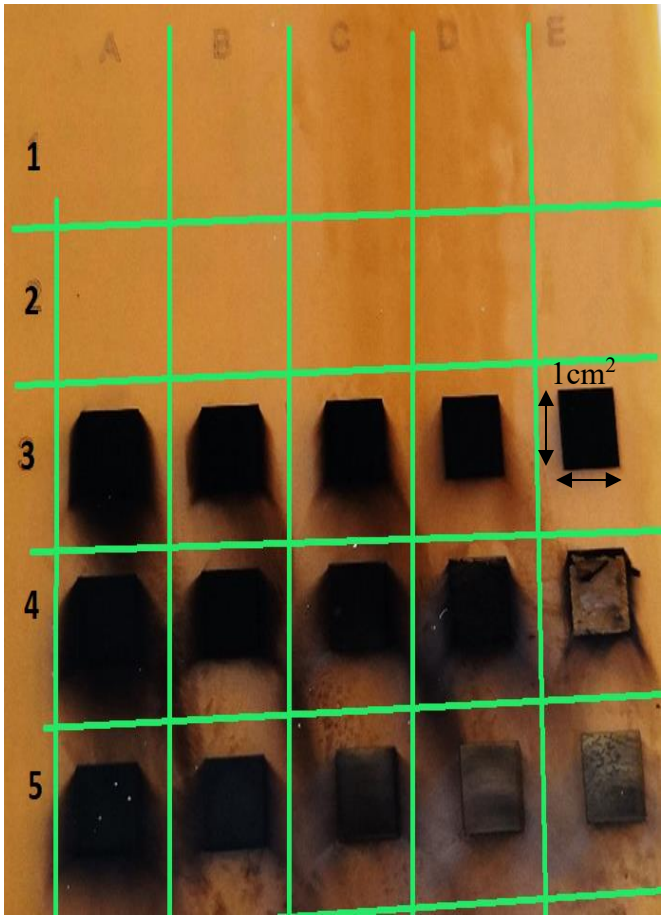

Figure 64: Second set of LIG on Kapton substrate " (***PV9100 SERIES***)" fabricated using an IR femtosecond laser system. Parameters are shown in Table VIII.

From this last parametric study, only samples (3B, 3C, 3D, and 3E) furnished graphite material. The low value of resistivity has then been obtained. Table IX summarizes those results and Fig. 65 to 68 give their respective views under SEM.

Table IX: Best LIG results using IR-femtosecond laser engraving of Kapton film.

Sample	Frequency (kHz)	Power (%)	Speed (mm/s)	Resistivity (Ω.cm)
3B	**200**	**5**	**20**	**65.1**
3C	**200**	**5**	**30**	**76.7**
3D	**200**	**5**	**40**	**95.7**
3E	**200**	**5**	**50**	**93.3**

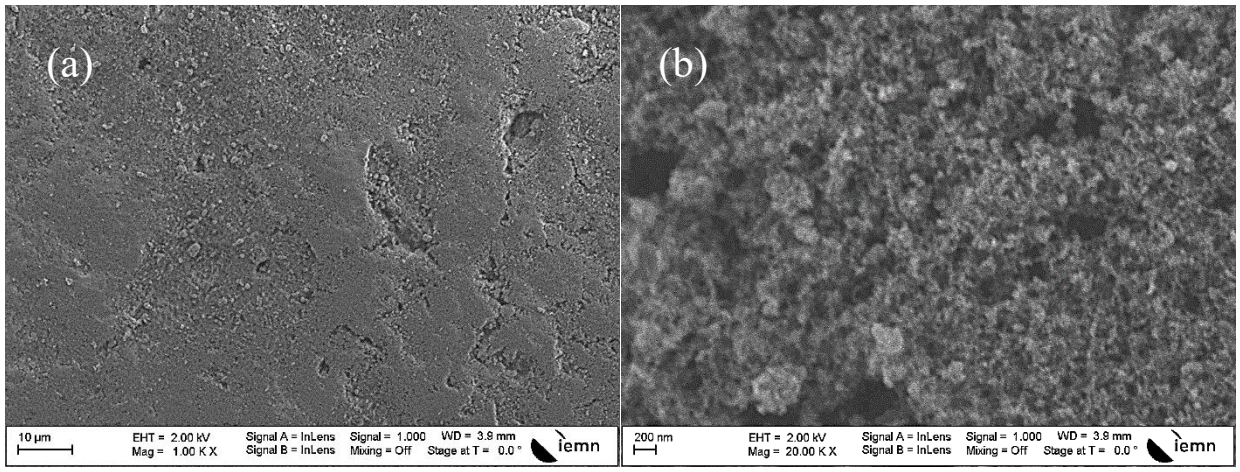

Figure 65: Laser-Induced Graphene: "3B" sample top view: a) 10 µm scale, b) 200 nm scale.

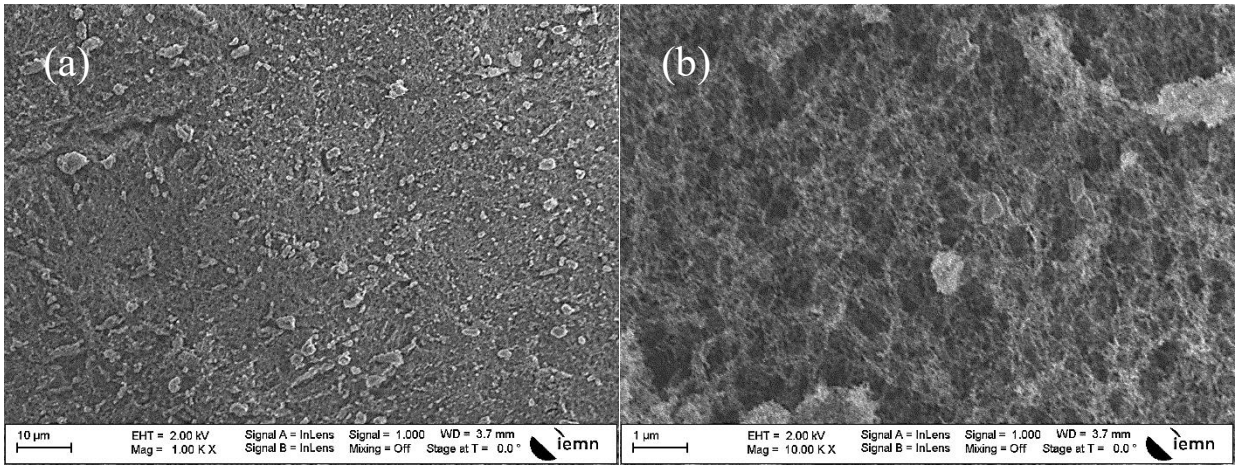

Figure 66: Laser-Induced Graphene "3C" sample top view a) 10 µm, b) 1 µm scale.

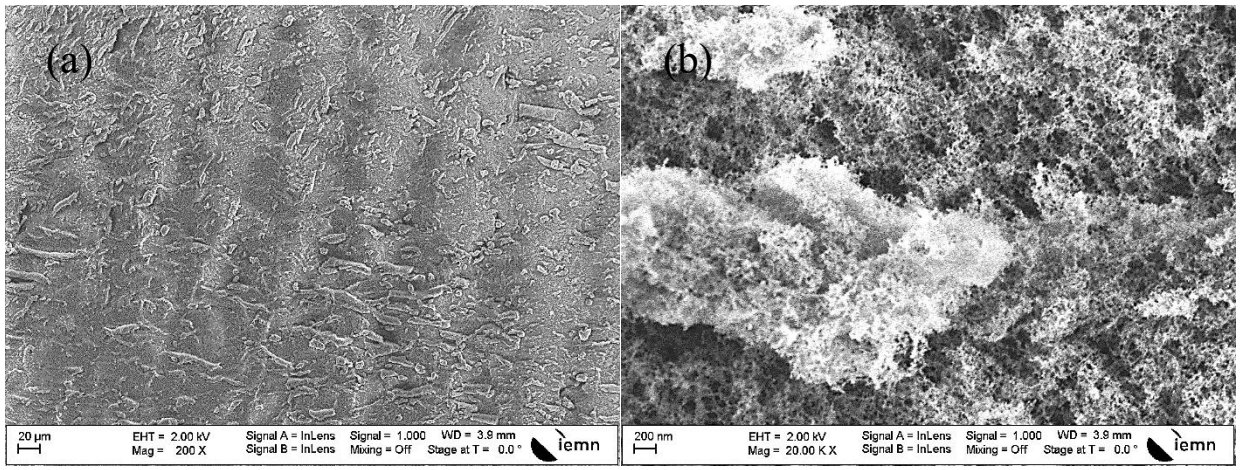

Figure 67: Laser-Induced Graphene "3D" sample top view: a) 20 µm scale, b) 200 nm scale

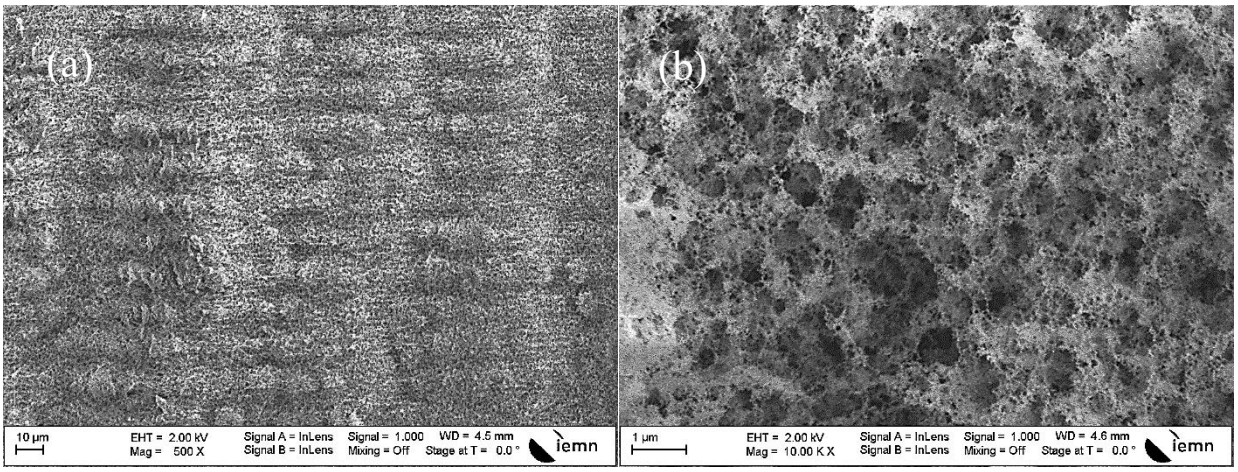

Figure 68: Laser-Induced Graphene "3E" sample top view: a) 10 µm scale, b) 1 µm scale.

Based on the above results and in order to confirm the presence of graphene on the surface of the Kapton substrate, an XRD analysis was performed. The result (Fig. 69) shows a peak of graphite (multi-layers of graphene) that is in good agreement with all the previous SEM images illustrating the carbon sheets.

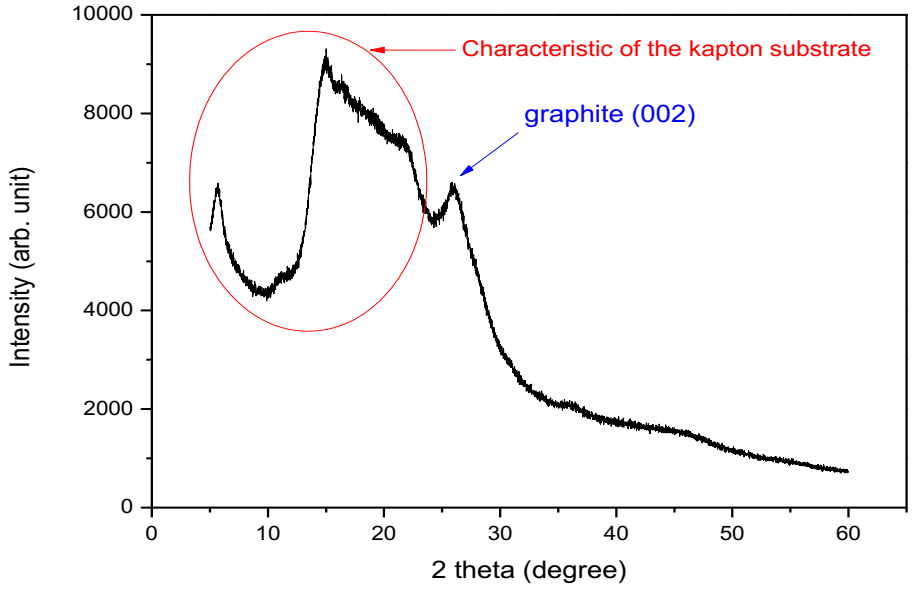

Figure 69: XRD pattern of graphite on Kapton.

The best LIG layer has roughly a 60 Ω.cm resistivity that can be compared to the one of graphite, which is around 1kΩ.cm. The films are composed of nano-walls with a thickness of 60-80 nm (measured using AFM). Some discontinuities between nano-walls can be seen by SEM that may reduce the conductivity. The film is flexible, but cracks start to

appear around a (60° – 70° degree) of bending (manually tested). Such a film can be used as a back-contact layer since it is not transparent.

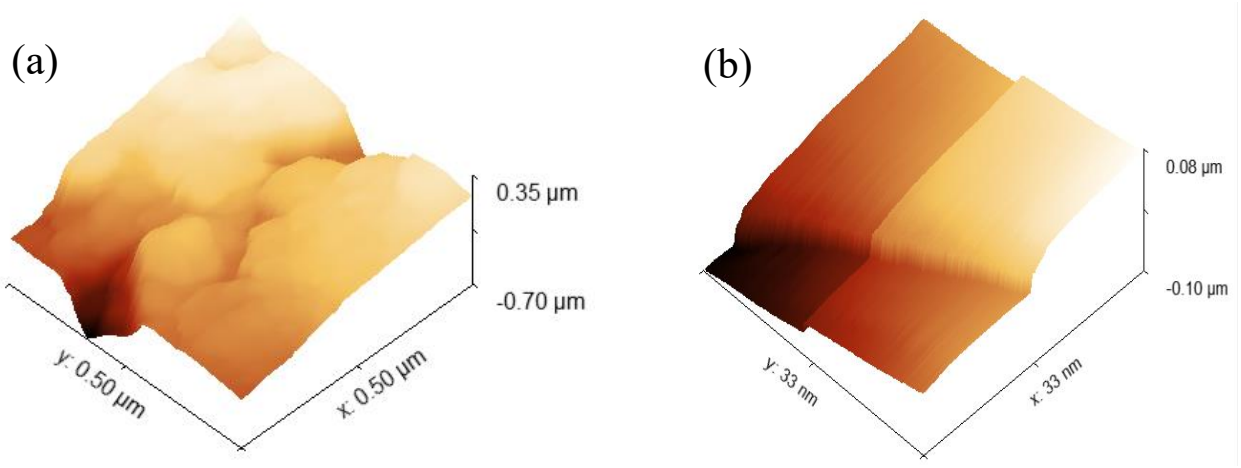

Figure 70: AFM analysis for the LIG surface shown in Fig. 54 for two different surface areas: a) 0.25 µm^2, b) 1000 nm^2.

Using the AFM results (Fig. 70), it appears that the graphene sheets have an average height-depth of 1 µm and thickness around 80 nm, on the other hand, the change in their parallel sheets configuration may increase the surface resistivity.

4.4 Metal oxide layer

In this part, we will explain the deposition results of the Metal Oxide layer using the different technologies on glass, Si, Au, ITO, and graphene as substrates.

4.4.1 *Al-doped ZnO "AZO" using sputtering*

Using the sputtering technique, a 20 nm-thick AZO film has been deposited on Si substrates. In order to increase base conductivity, a gold layer of 5 nm has been firstly deposited to serve as a back electrode (Fig. 71-72). Nevertheless, the resistivity of such a thin film is still rather high as to be used as an electrode. Film thickness has so been increased up to 300nm, which is almost a rather common value for such material.

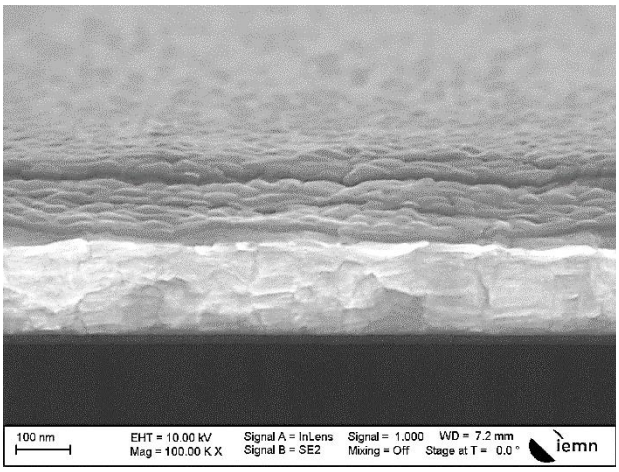

Figure 71: Cross-section of AZO deposited on 5 nm of Au /Si substrate.

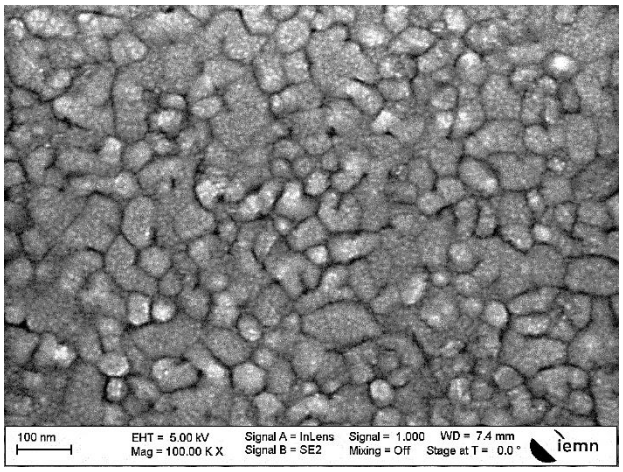

Figure 72: Top view of 20nm-thick AZO film deposited on 5 nm of Au /Si substrate.

The cross-section image (Fig. 73) reveals a dense film with a columnar structure such it can be awaited from a sputtering deposition process. The column size as it can be evaluated from the top view (Fig. 74) is ~ (10 - 40 nm).

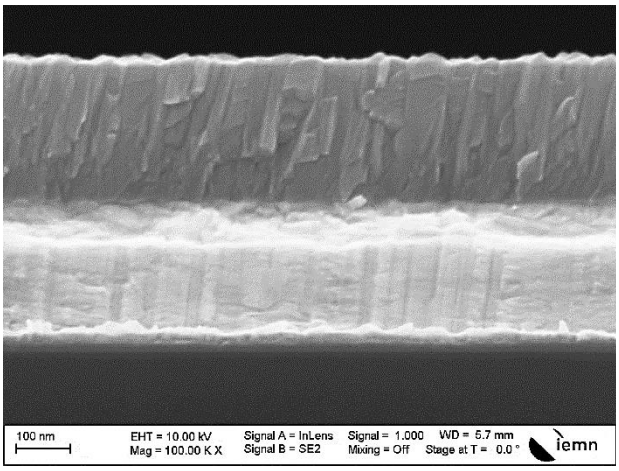

Figure 73: Cross-section of 300nm-thick AZO deposited on 5 nm of Au /Si substrate.

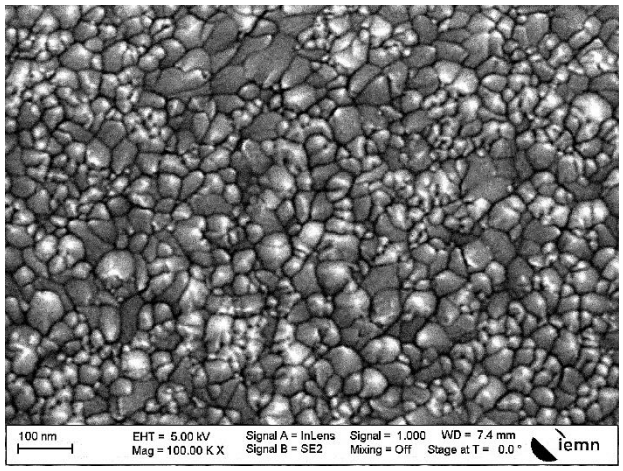

Figure 74: Top view of 20nm-thick AZO film deposited on 5 nm of Au /Si substrate.

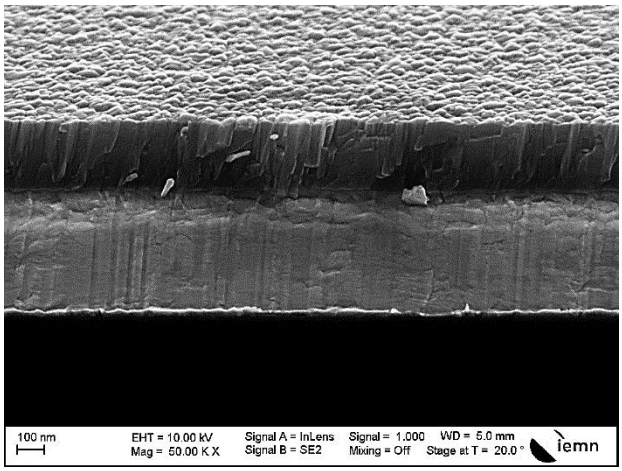

Figure 75: Tilted view of 300nm-thick AZO film deposited on 5 nm of Au /Si substrate.

By tilting the substrate of 20 degrees, the SEM image reveals the strong attachment between the AZO/Au and Au/Si (Fig. 75).

In parallel, the optical transmittance of the same 300 nm-thick AZO layer deposited on a glass substrate (without the base gold layer) has been measured using UV-vis spectroscopy (Fig.76). Its optical band gap, deduced from Tauc protocol, ranges from (3.3 - 3.8 eV) and is so slightly higher than those of pure ZnO thin films (3.2 -3.3 eV).

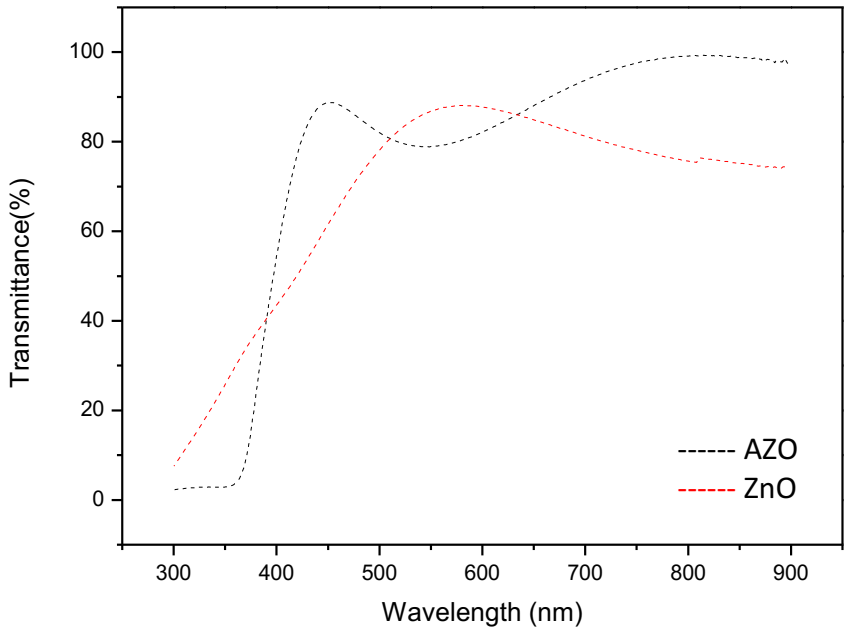

Figure 76: UV-Vis transmittance spectra of 300nm-thick AZO and undoped ZnO films.

4.4.2 *Al-Doped ZnO "AZO" using PLD*

PLD technique using a 248 nm KrF laser, 15 ns pulse width and a repetition rate of 10 Hz was also used to fabricate AZO layers. It was estimated that the laser pulse fluence on the surface of the target was 500 mJ/pulse and the lens focused the laser beam on the AZO target for around 8 J mm^{-2}. Due to the time limitation I faced in booking and using the equipment, the deposition was directly done on a LIG engraved layer on a Kapton substrate. While using a 2 inches target, the number of laser pulses was tested in a range of (500, 1000, 2000, 3000 and 5000 pulses) (Table X).

Table X: Process parameters for different AZO deposited films using PLD.

Pressure	Number of laser pulses	Observations
50mTorr	500	No depostion
	1000	Large islands and very low distribution ~10nm
	3000	Thin layer and full distribution~90nm
	5000	Thicker layer and full distribution~250nm

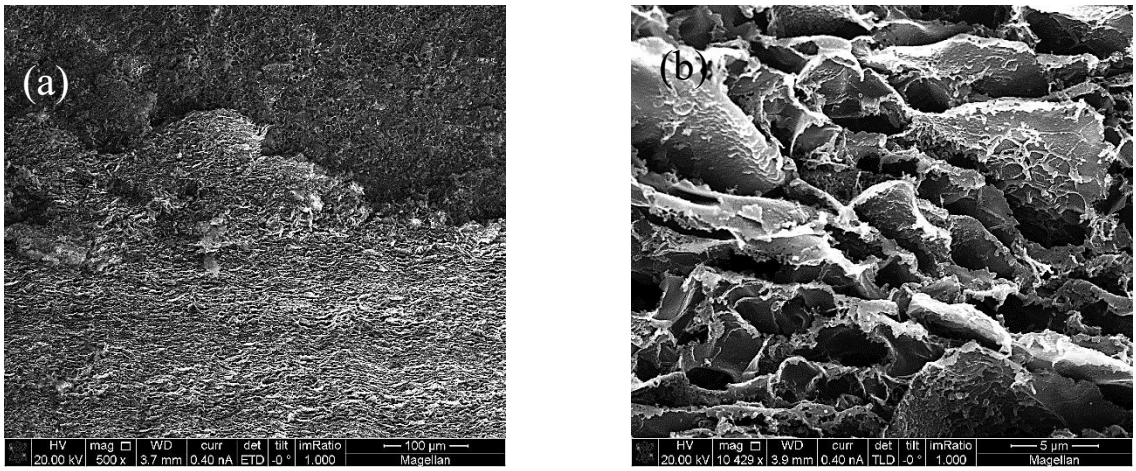

Figure 77: AZO deposited by PLD (1000 pulses) on LIG substrate top view: a) 100 µm scale, b) 5 µm scale.

When using only 1000 laser pulses at a temperature of 480°C in a 500 mTorr background pressure of high purity oxygen, the LIG is by far not fully coated by the AZO film (Fig. 77.a & b) due to the shadowing effect, which can produce nanostructures tilted toward the incident deposition flux. This effect can be reduced by rotating the substrate under the deposition of flux with the right speed obtained by a parametric study. [18]

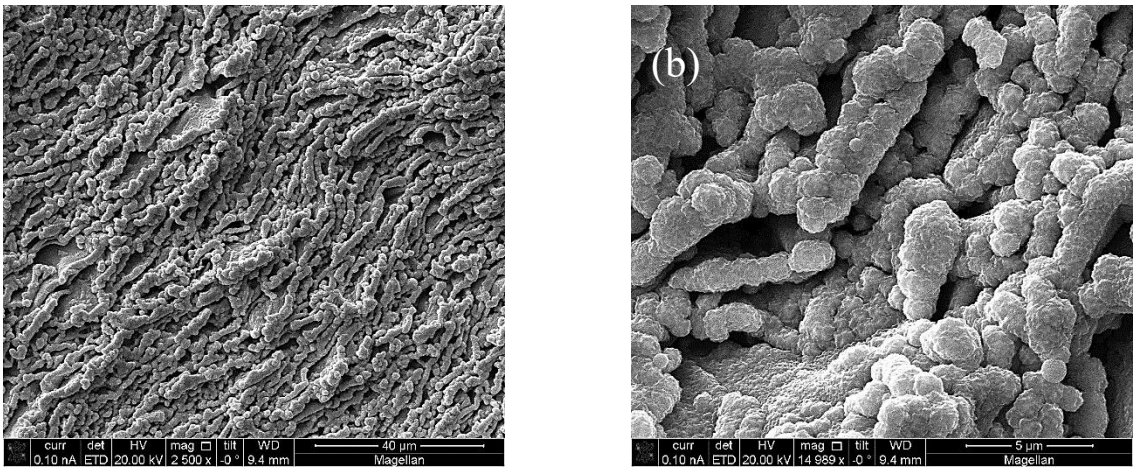

Figure 78: SEM images of AZO deposited by PLD (3000 pulses) on LIG substrate top view: a) 40 µm scale, b) 5 µm scale

Then, the number of pulses was gradually increased to fully cover the sheets keeping in mind the diverse orientation they have. The full coverage has been obtained for 3000 pulses. The corresponding morphology is illustrated in (Fig. 78, 79)

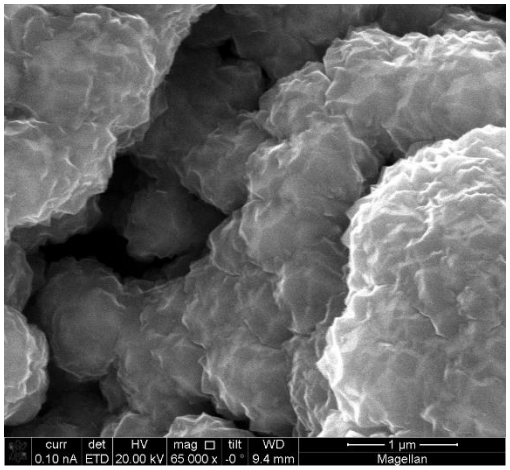

Figure 79: SEM image of AZO deposited by PLD (3000 pulses) on LIG substrate top view 1 µm scale.

4.4.3 *ZnO using hydrothermal process*

The ZnO layer has been synthesized by the hydrothermal technique using a solution of zinc nitrate "$Zn(NO_3)_2$" and hexamethylenetetramine "$C_2H_{12}N_4$", both having the same molar ratios (0.02mol) diluted in (200mL) deionized water. The deposition time was 4 hours. The SEM images of the film show that the resulting surface exhibits different flower-shaped wurtzite zinc oxide microstructure (Fig. 80.a). The flower-like structures result from the clustering of hexagonal nanorods of ZnO (0.3µm diameter and 1µm length) and are

distributed all over the LIG surface (Fig. 80.b). It has been noticed that the distribution of ZnO was not uniform on the surface. The nonuniform distribution was also obtained even when the deposition time was increased up to 6 hours (Fig. 80.c, d).

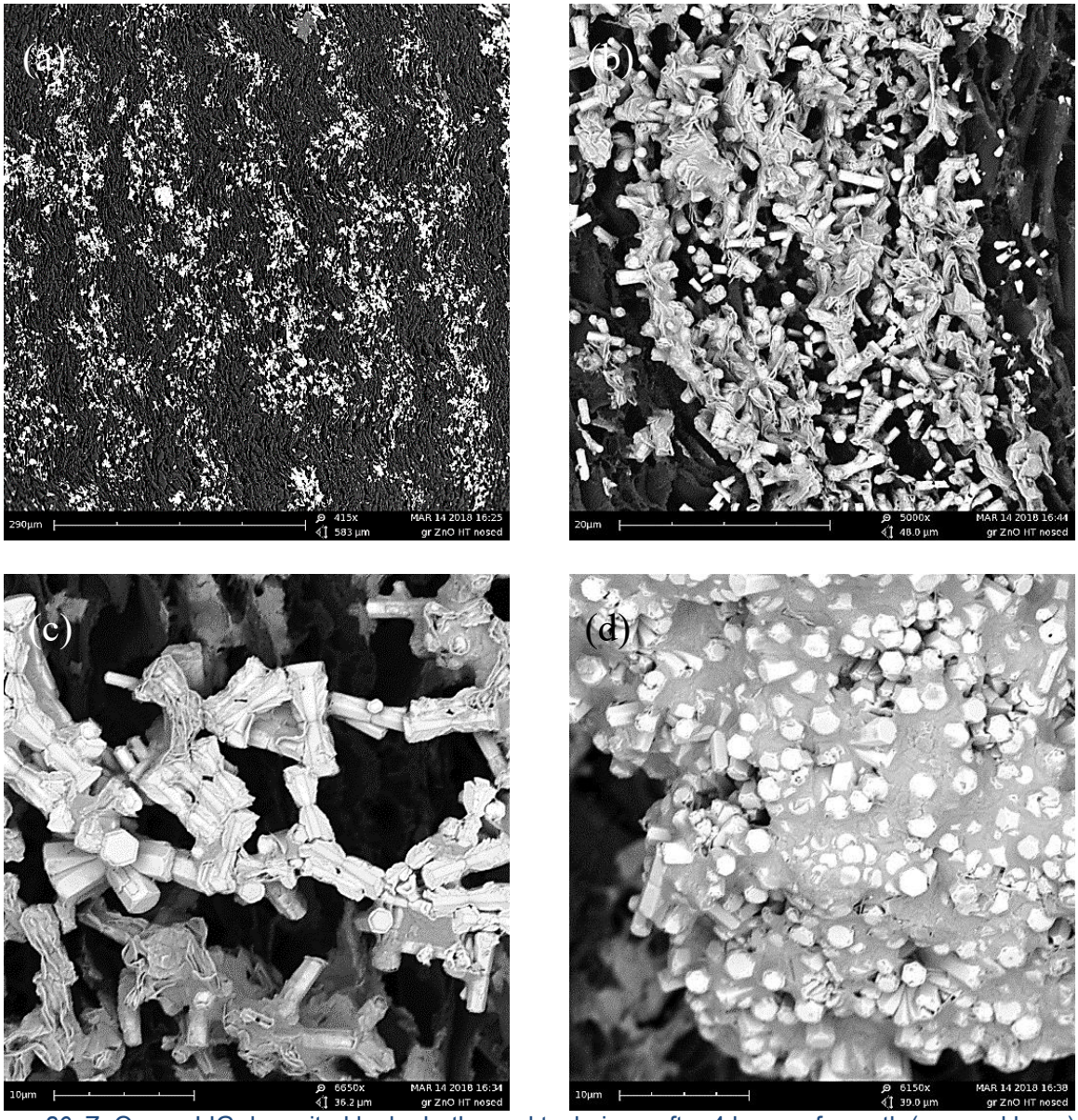

Figure 80: ZnO over LIG deposited by hydrothermal technique after 4 hours of growth (no seed layer): a) Uneven low rate of distribution in a 300 µm scale, b) Collection of ZnO nano hexagonal rods in 20 µm scale, c) Collection of ZnO nano hexagonal rods in a 10 µm scale, d) significant clustering of ZnO nano hexagonal rods in 10 µm scale

The uniform distribution of ZnO on the surface of LIG was resolved by changing the substrate to a LIG graphene on Kapton substrate with a ZnO seed layer (~10nm) deposited by PLD using 1000 pulses. By adding the seed layer and using a deposition

time of 4 hours (Fig. 81.a, b) and 6 hours, the results reflect the growth of nanosheets of ZnO all over the surface (Fig. 81.c, d)

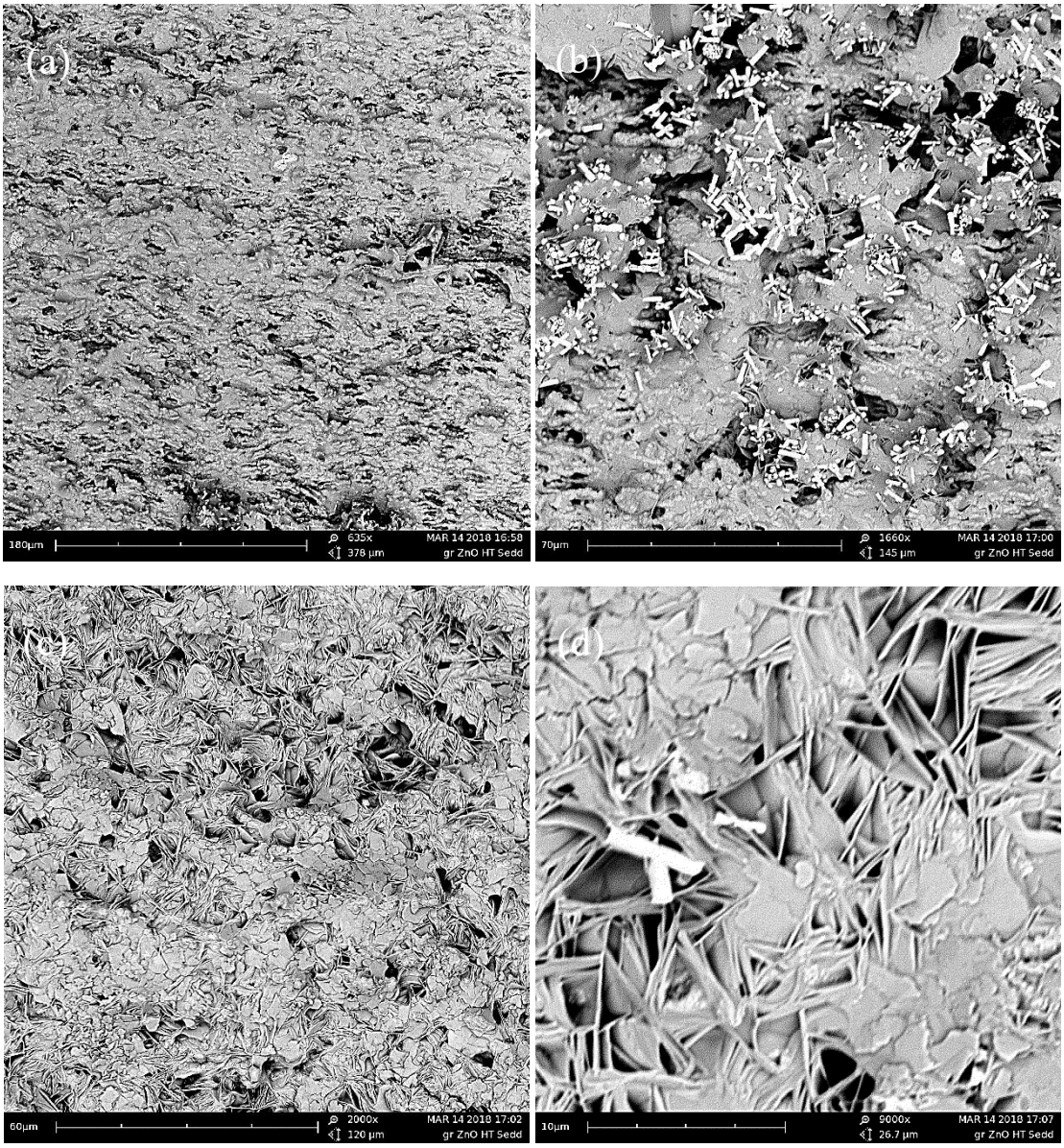

Figure 81: ZnO over LIG deposited by hydrothermal technique (with seed layer): a) 4 hours of growth in 180 µm scale, b) 4 hours of growth in a 70 µm scale, c) 6 hours of growth layer in a 60 µm scale, d) 6 hours of growth in 10 µm scale

4.5 Absorbing layer made of La_2CuO_4

Different deposition techniques have been used to synthesize La_2CuO_4, such as sputtering in DC mode and RF mode and PLD at different deposition times.

4.5.1 *La_2CuO_4 sputtering results*

4.5.1.1 As deposited

In this process, we used Si substrate, and a glass with 5 nm of Au coating layer (to improve its conductivity) substrate to determine the absorption, then and last a glass substrate with a layer of AZO around 300 nm as planed in the scheme.

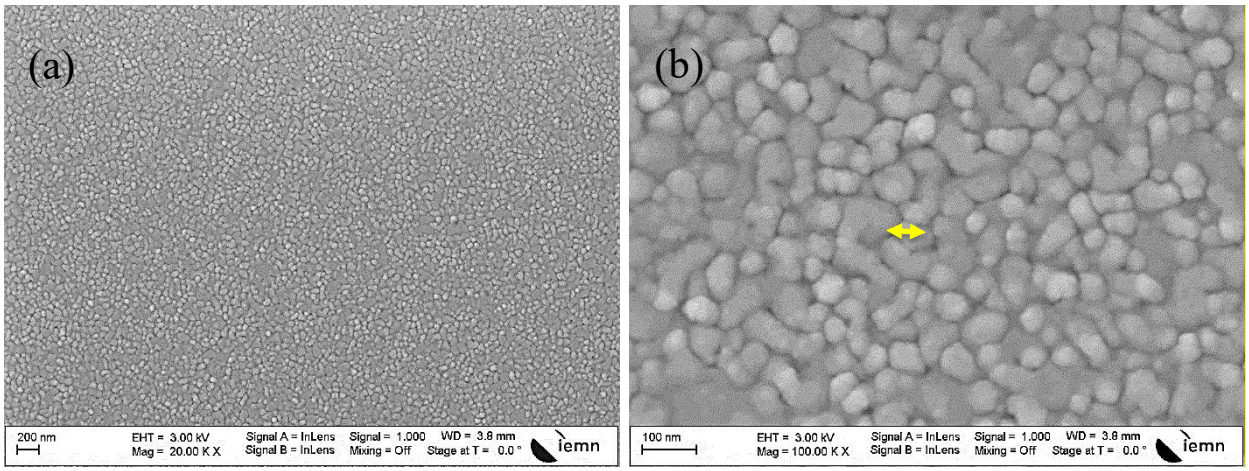

Figure 82: La_2CuO_4 over a coted layer of Au (5 nm) on a glass substrate by sputtering: a) in a 200 nm scale, b) in a 100 nm scale.

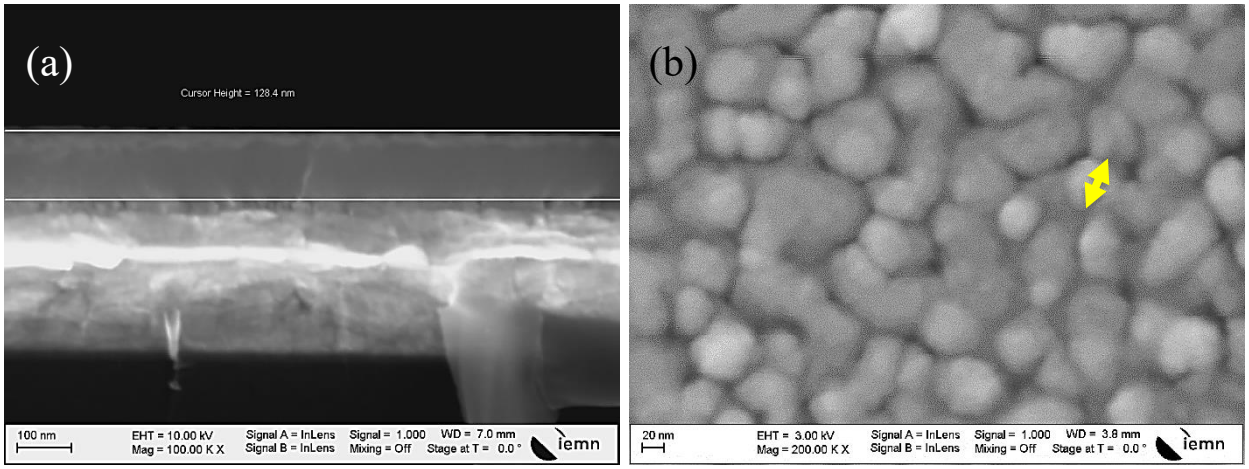

Figure 83: La_2CuO_4 over a coted layer of Au (5 nm) on a glass substrate by sputtering: a) cross-section in a 100 nm scale, b) in a 20 nm scale.

The SEM images of the La_2CuO_4 fabricated by DC-sputtering on an Au layer are shown in Fig. 82 and reflect well-distributed grain shapes with a size of (25-30 nm).

The cross-section image in Fig. 83.a reflects a thin layer of approximately 130 nm of the La_2CuO_4 structure with a grained surface (Fig. 83.b).

A comparison study was conducted in the deposition of thin films of La_2CuO_4 obtained by RF-sputtering and DC-sputtering. The SEM images of the La_2CuO_4 fabricated by RF-sputtering on an Au layer reflect a sponge surface aspect (Fig. 84).

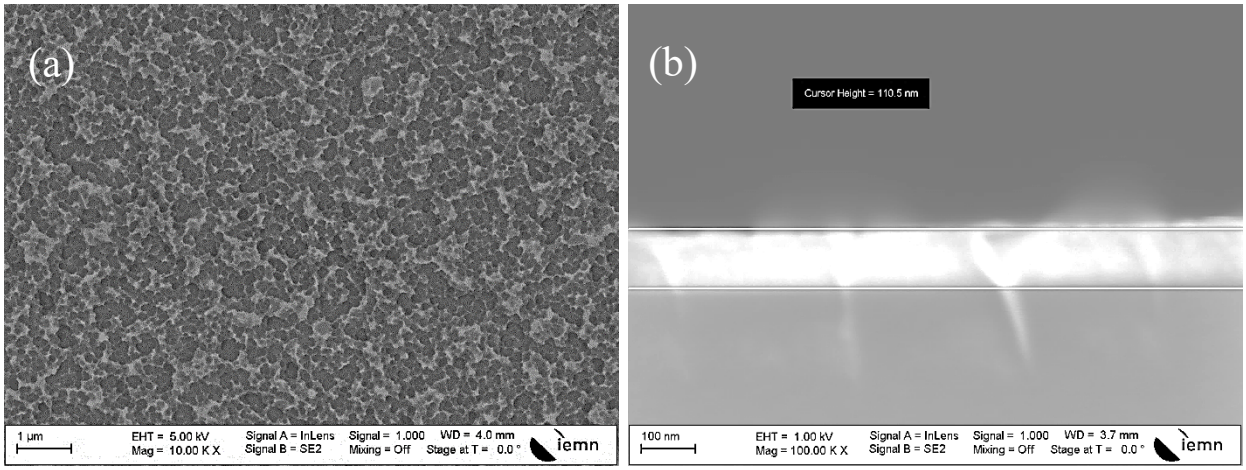

Figure 84: SEM images of La_2CuO_4 over a Si substrate using RF sputtering: a) top view in a 1 µm scale, b) cross-section in a 100 nm scale.

On the contrary, the SEM images of the La_2CuO_4 fabricated by DC-sputtering on an Au layer reflect a well-distributed deposition with islands topography (Fig. 85).

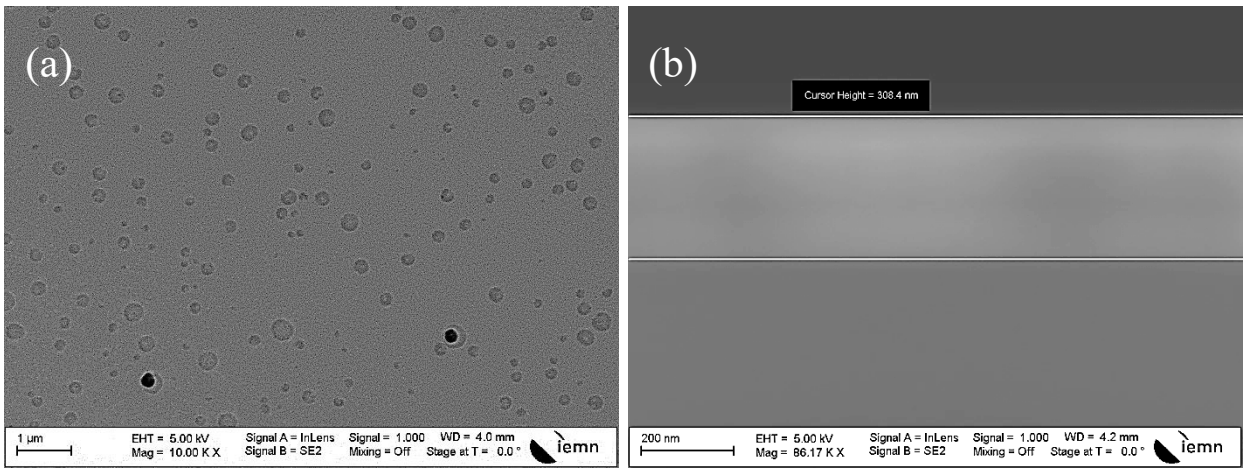

Figure 85: SEM image of La_2CuO_4 over a Si substrate using DC sputtering: a) top view in a 1 µm scale, b) cross-section in a 200 nm scale.

During the fabrication process, it was noted that the RF-sputtering technique consumes more time, energy, and materials to produce the same thickness as in the DC-sputtering technique: 10 minutes in DC mode are equivalent to 30 minutes in RF mode and produced a thin layer of ~ 50nm thickness.

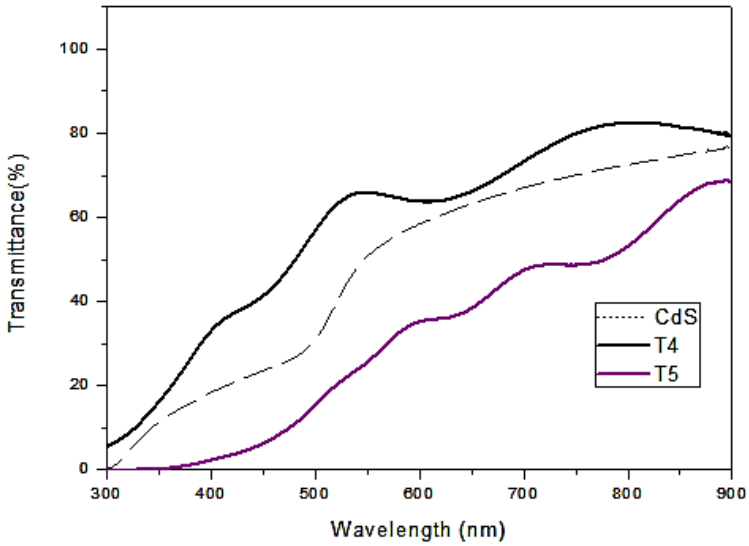

Figure 86: Comparison of UV-vis spectra for different thicknesses of La_2CuO_4: T4 represents 50 nm, T5 represents 480 nm. Comparison is made with a 20 nm thick CdS film.

.

Several samples of different thickness (50, 200, 480 and 850 nm) have been elaborated. The UV-Vis transmittance spectra for samples of 50 and 480 nm thickness are shown in Fig. 86. It can be observed an absorption band edge that is different for the two thicknesses, illustrating that material bandgap is not constant when film thickness is tuned: thicker is the film, lower is the bandgap. This was confirmed by the bandgap value that is estimated by the Tauc plot for the different film thicknesses, 50nm, 480nm, and 850nm, as shown in the Fig.94 is around 3.75 eV, 3.25 eV, and 3 eV, respectively. It have been noticed thatthereis a red shift in the band gap by the increasing of the film thickness, confirmed similar studies on the same perovskite materials (LCO, and STO). [22, 23]

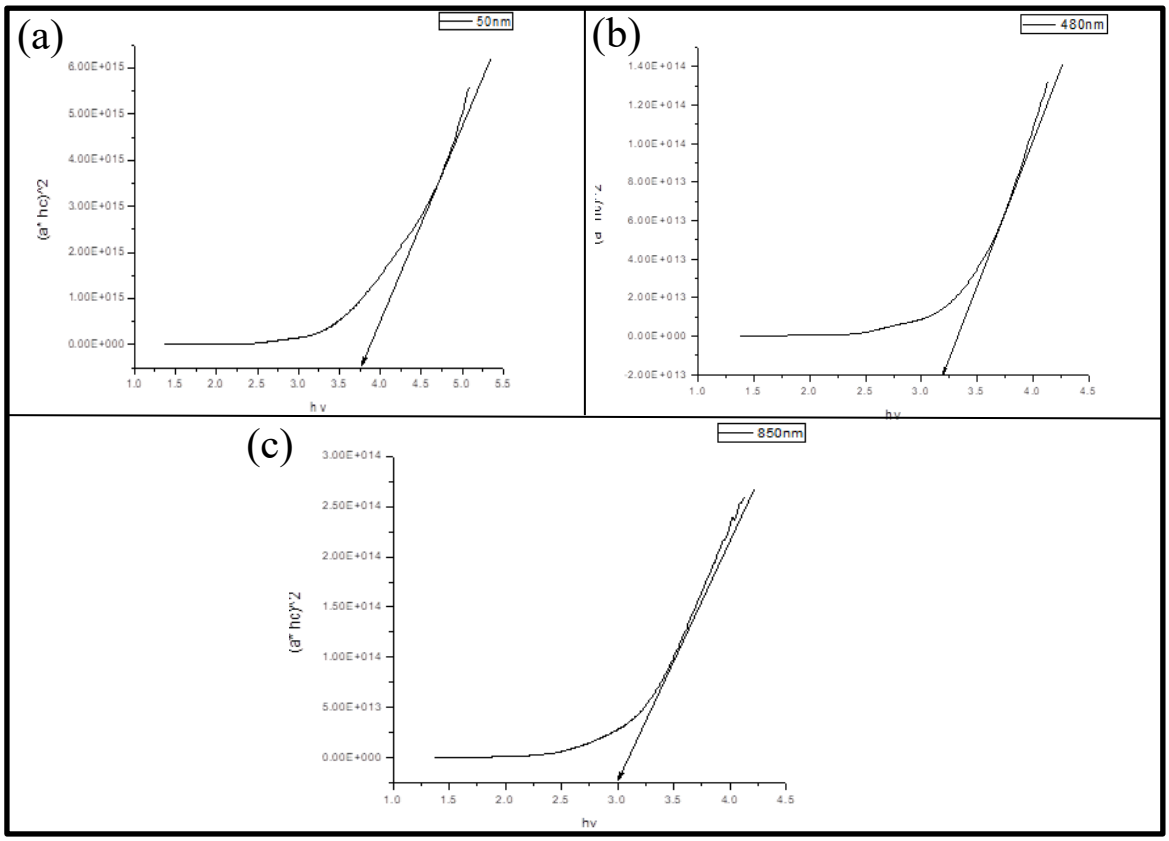

Figure 87: T_{auc} plot and corresponding optical bandgap of the thin-films of La_2CuO_4: a) 50nm in thickness, b) 480nm in thickness, c) 850nm in thickness

To investigate and confirm the distribution of the sputtered material (La_2CuO_4), an EDX analysis was made (Fig. 88).

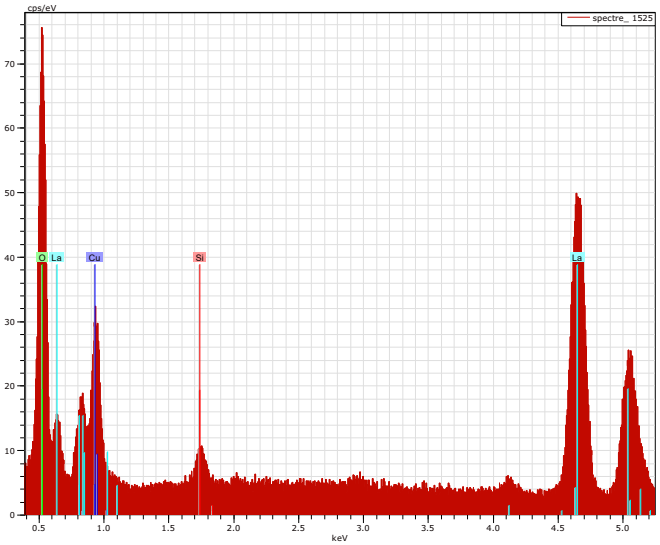

Figure 88: EDX analysis of La_2CuO_4 film over a Si substrate using sputtering in DC mode.

The EDX analysis indicates the presence of the basic elements composing La_2CuO_4. The respective ratio of elements seems fulfilled but the stoichiometry of the film shall require further investigation to be clearly stated. An overall uniform material distribution can be observed (Fig. 89).

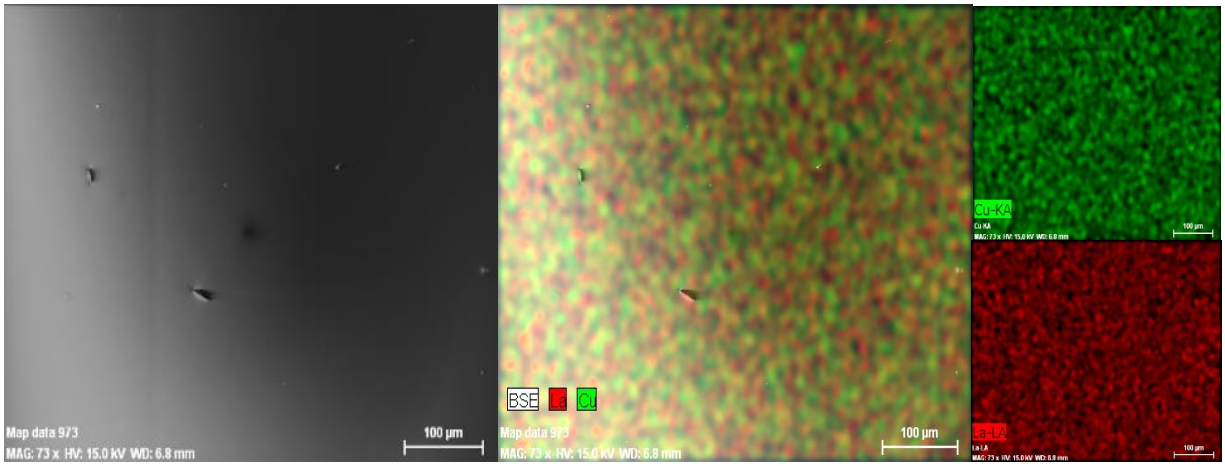

Figure 89: EDX reading of La_2CuO_4 over a Si substrate using sputtering, confirmed a uniform distribution.

The morphological properties were also studied by the AFM technique to identify the topology of the surface. The AFM images for a DC-sputtered La_2CuO_4 of 50nm thickness over a glass substrate are shown in (Fig. 90). It was revealed discrete spherical entities with smooth surface features that are consistent with the SEM images. Their diameter ranges from 22 to 60 nm, with an average value of around 40 nm. The average roughness is 9.8 nm.

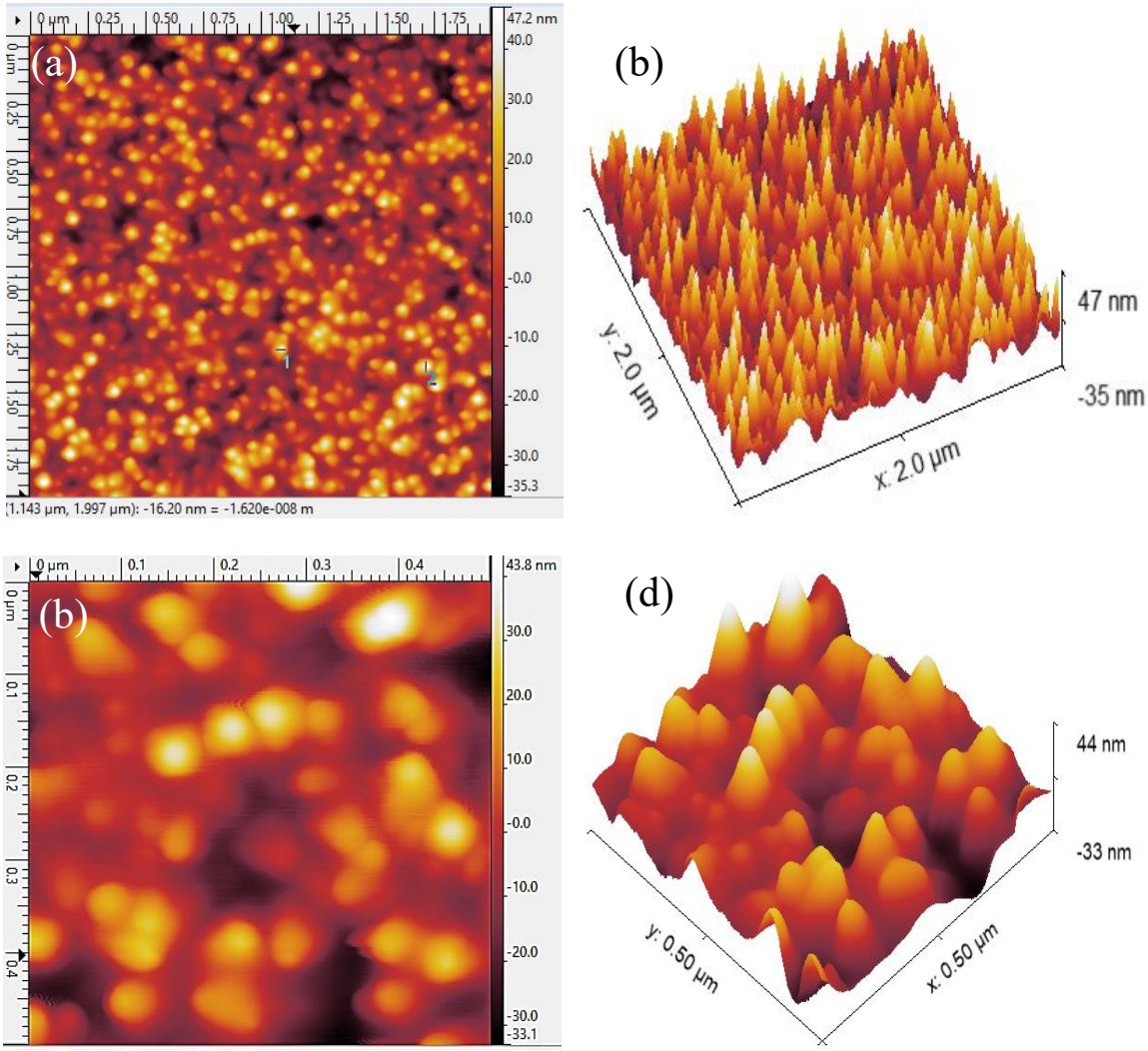

Figure 90: AFM image for 50nm-thick La_2CuO_4 layer over a glass substrate: a) Surface topography low resolution, b) Low-resolution 3D computed image, c) Surface topography higher resolution, d) Higher resolution 3D computed image.

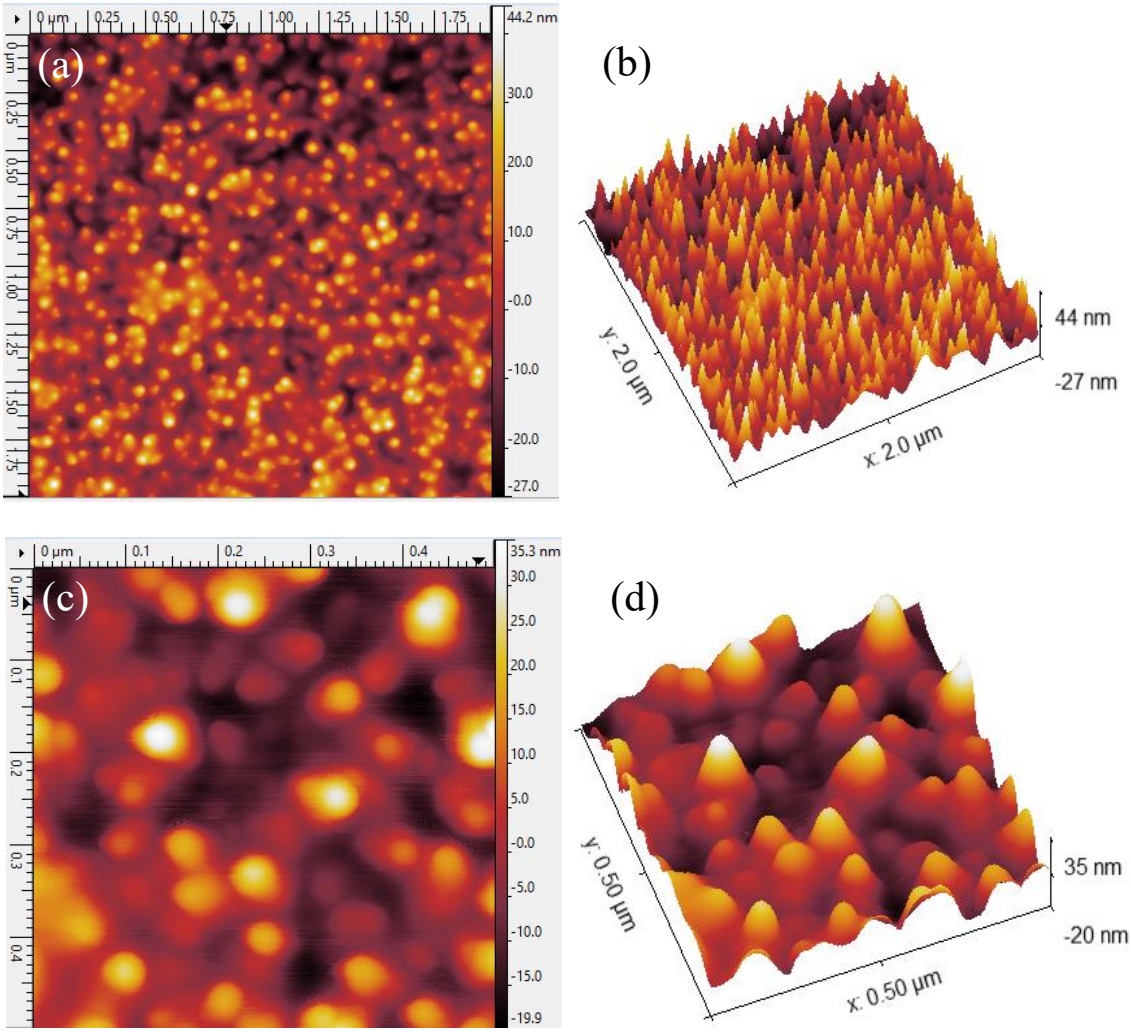

Figure 91: AFM image for 450 nm-thick La_2CuO_4 layers (over a glass substrate): a) Surface topography low resolution, b) Low-resolution 3D computed image, c) Surface topography higher resolution, d) High-resolution 3D computed image.

The AFM scans for La_2CuO_4 of 450nm thickness over a glass substrate are shown in Fig. 91 and revealed the same spherical entities. The histogram of the island heights corresponding to the AFM image cross-section height analysis of these entities showed spherical-shaped particles with a diameter ranging from 15 to 40 nm. Their average diameter determined was around 35 nm and average roughness is 7.9 nm.

4.5.1.2 Post anneal

Thermal annealing was made to investigate its effect on material properties. Using a Kapton substrate and taking into consideration its temperature limitation, we used a

maximum temperature of 450˚C. After several trials during different time sequences in Ar atmosphere, no significant structural changes have been noticed.

To compare the films obtained by sputtering to others obtained using other techniques [19-21], a Si substrate has been used allowing anneal to higher temperature: 600 ˚C for 30 min in Ar under an atmospheric pressure followed by a moderate cooling (150˚C/h). In those conditions, the surface showed a clustered large spherical grains (430nm) topology for a layer of 450nm thickness (Fig.92 b to d). (Fig. 92a) represents the surface morphology of the DC sputtered film before annealing.

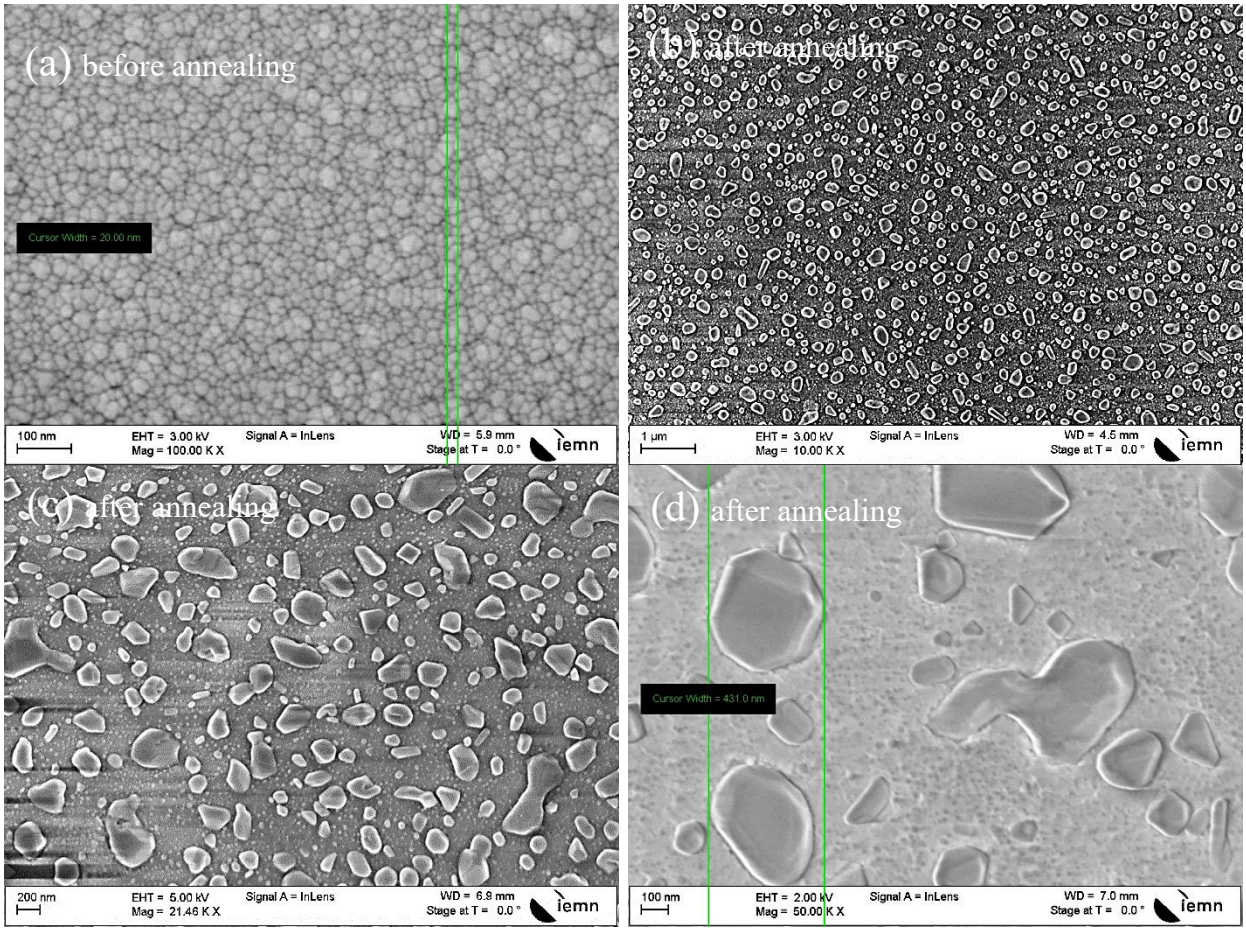

Figure 92: La_2CuO_4 over a coated layer of Au (5 nm) on Si substrate: a) before annealing in a 100 nm scale, b) after annealing in a 1 µm scale, c) after annealing in a 200 nm scale, d) after annealing in 100 nm scale

Such an experiment has also been done on a 50nm-thick film. After the annealing (Fig. 93a & b), it has been noticed that the surface is covered with two groups (based on size)

of clustered grains. The large size (~180nm) grains clustered by thermal treatment and small size (~20nm) the original before the annealing process.

For both set of experiments post-anneal results in a clustering of species, which is a rather similar behavior as obtained with the perovskite family material after heat-treatment. [19-21]

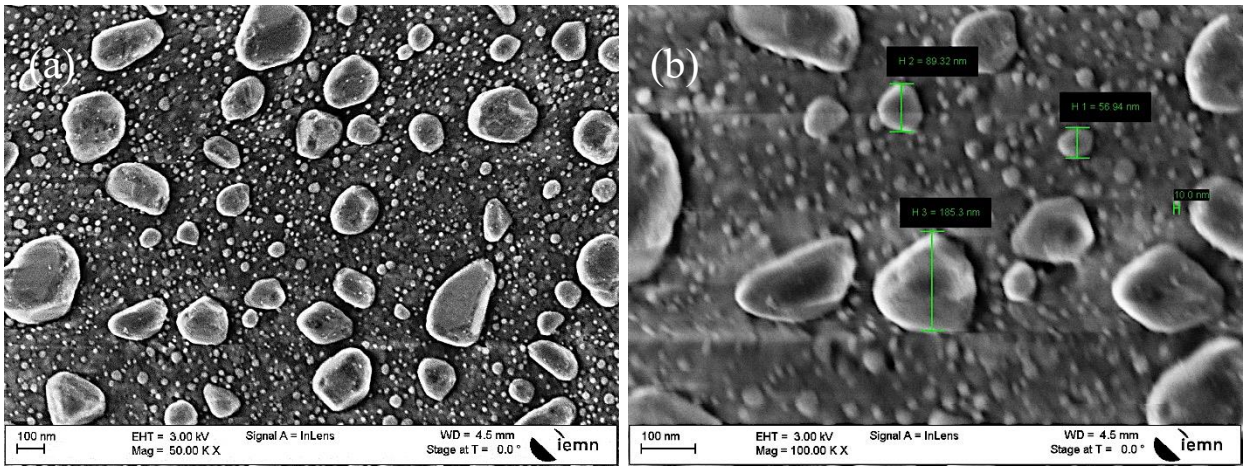

Figure 93: *SEM images of La_2CuO_4 over a coated layer of Au (5 nm) on Si substrate after annealing: a) in a 100 nm scale, b) in a 100 nm scale.*

4.5.2 *La_2CuO_4 PLD results*

In this technique, thin films of La_2CuO_4 were deposited with a different number of pulses (1000, 3000, and 5000) (Fig. 94). A 248 nm KrF laser with pulse lengths of 15 ns and a repetition rate of 10 Hz was engaged as the light source. The estimated laser pulse fluence on the surface of the 2-inch target was 500 mJ/pulse, and the focal lens focused the laser beam on the La_2CuO_4 target for around 8 $J.mm^{-2}$. The films were deposited on a (100) Si substrate at a temperature of 480°C in a 500 mTorr background pressure of high purity oxygen. A rotational movement during the process with a speed 90 degree/s has been applied to the substrate holder.

Figure 94: La_2CuO_4 over ZnO (400nm thickness) with Si substrate for a) 5000 pulses, b) 3000 pulses, c) 1000 pulses.

Since the PLD deposition by 1000 pulses did not provide quantifiable or uniform distribution, and the 5000 pulses deposited a thicker layer (~400nm) with the NPs aggregated in each other which is far from our targeted active layer (Fig. 95), both were dismissed from farther investigating and only the 3000 pulses sample gave NPs (Fig. 96).

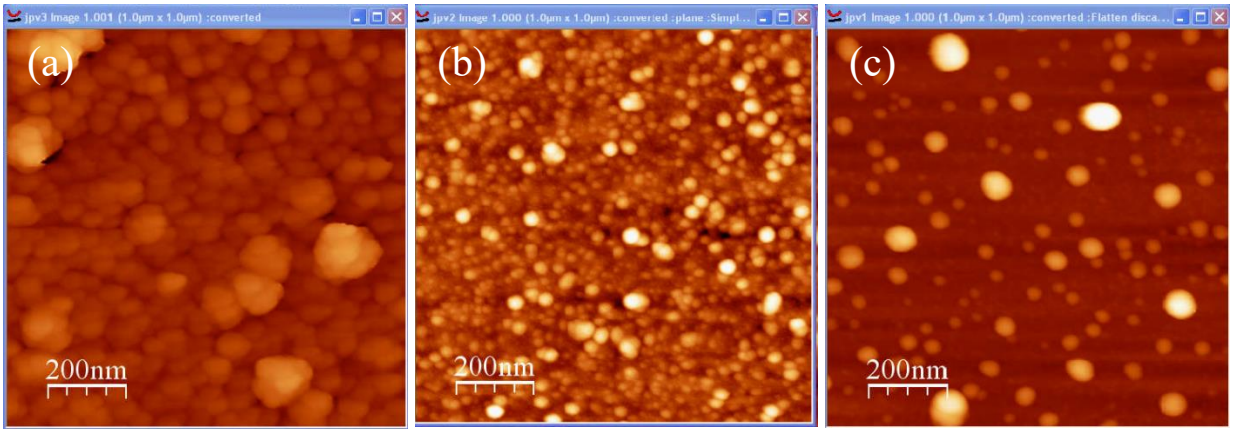

Figure 95: AFM scans for La_2CuO_4 fabricated by PLD with different number of pulses: a) 5000 pulses, b) 3000 pulses, c) 1000 pulses.

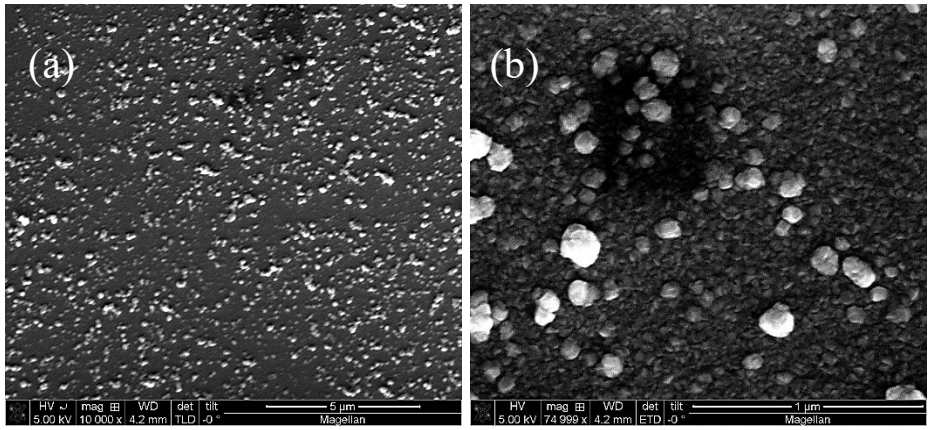

Figure 96: SEM images of La_2CuO_4 on Si wafer using 3000-pulse laser deposition process: a) on a 5 um scale, b) in a 1 um scale.

The AFM scans for La_2CuO_4 fabricated by PLD (3000 pulses) thickness over a Si substrate (Fig. 95b) revealed NPs size about 10nm- 40nm. Those NPs expected to give high absorption for our design. Unfortunately, such a deposition on glass substrate could not have been made and no confirmation about their absorption can be given right now.

4.6 First attempt of solar cell

After going through the fabrication of the different constituting layers of the cell using different techniques, the next step was to attempt merging all those processes to get the structure of a solar cell.

As shown in Fig. 97, La_2CuO_4 NPs (~50 nm) were successfully attached to a ZnO thin layer (~300 nm) by using the PLD technique over the graphene sheets fabricated by LIG based on Kapton substrate.

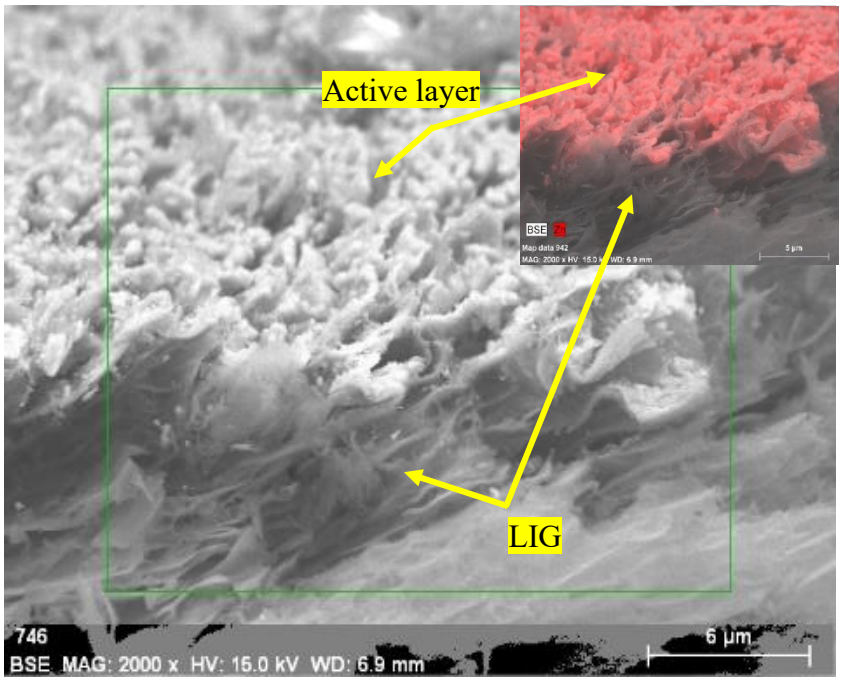

Figure 97: SEM cross-section image of LIG/ZnO/La_2CuO_4 (red-colored EDX image).

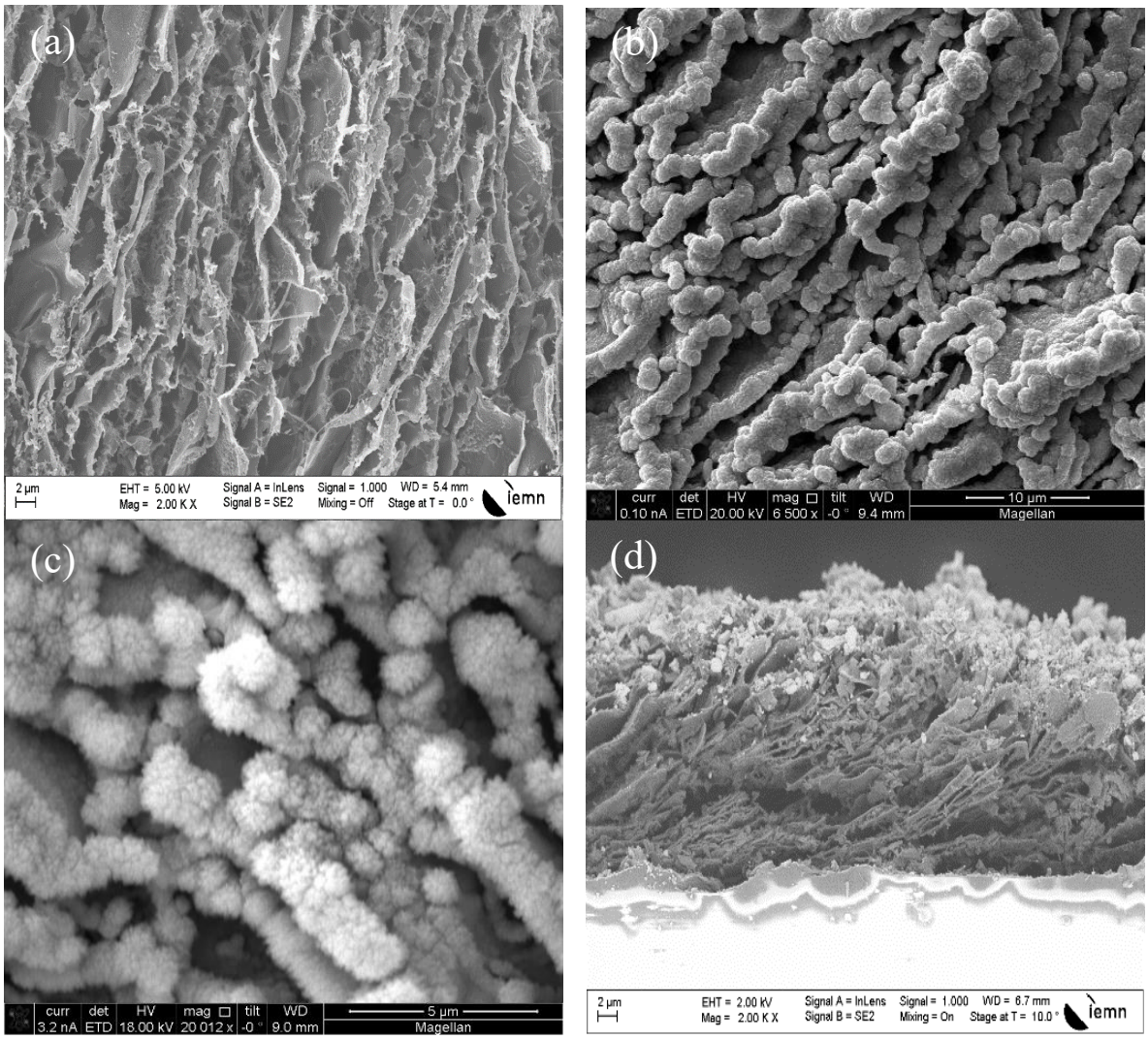

Figure 98: SEM images of the fabrication process: a) LIG sheets, b) ZnO thin layer covering LIG, c) La_2CuO_4 NPs deposited on top of the ZnO layer, d) Cross-section image of LIG/ZnO/La_2CuO_4.

The device fabrication started with the layer of LIG (back electrode) on the Kapton substrate (Fig. 98.a). Then, the thin layer of ZnO was deposited (granite surface) on top of the LIG (Fig. 98.b). The ZnO surface was then covered by La_2CuO_4 NPs (snowfall surface) (Fig. 98.c). SEM as FIB cross-section images confirm the La_2CuO_4 NPs formation on the ZnO thin layer (Fig. 98.d & 99).

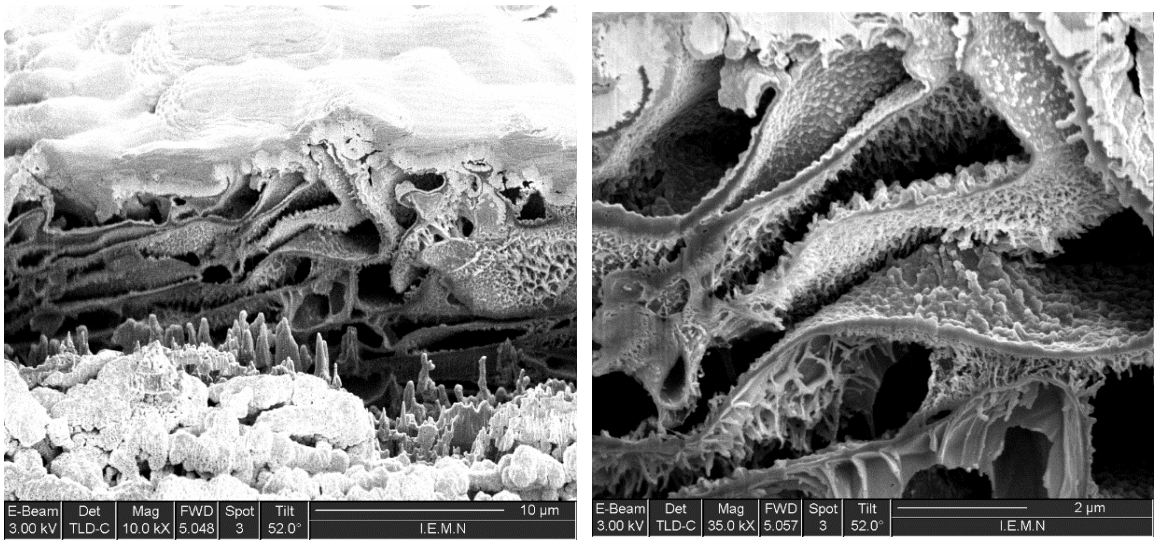

Figure 99: FIB cross-section images of LIG/ZnO/La_2CuO_4.

An AZO layer was then deposited on top as well as an Au top-electrode. Different prototypes were fabricated as shown in Fig. 100.

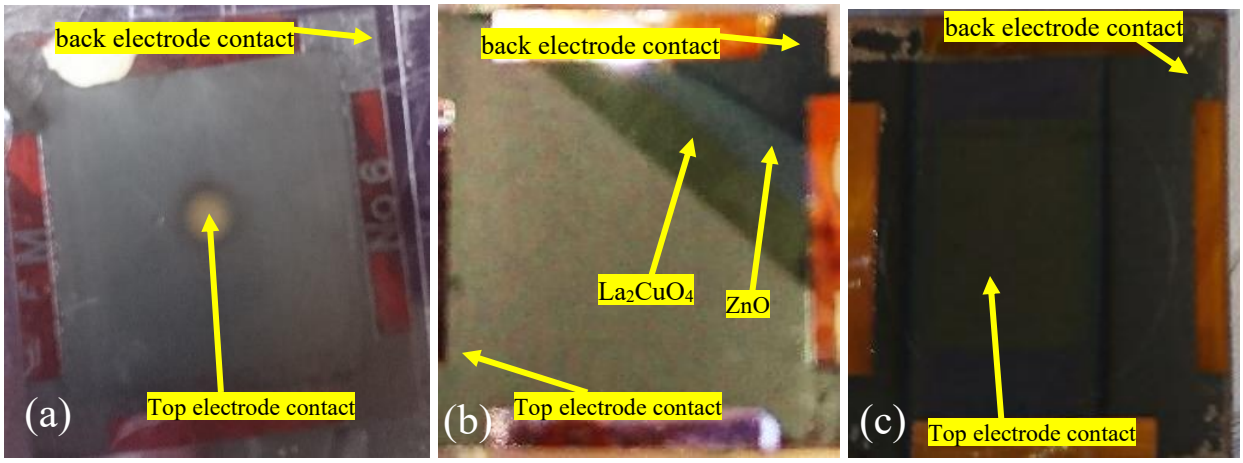

Figure 100: Different solar cell prototypes: a) centered top electrode, b) partially covered step top electrode, c) partially covered centered top electrode.

The I-V curve shown in Fig. 101a) shows an almost photoconductor behavior illustrating that no junction is present in the device that is rather understandable considering the materails used. A very small photocurrent is obtained (approx. 3 µA @ 2V) under AM1.5G illumination that nevertheless shows a photoelectric behavior (Fig. 101b)). This small value can be linked to a bad photoconversion within the La_2CuO_4 or a bad carrier transport between the NPs and the carrier transport layers. Even if this first attempt was not really convincing, it shows that some photocurrent can be obtained and so that the NPs genrate

photocarriers. Obviously, it shall be reiterated with a deeper insight at each step of fabrication to fully investigate the potentialities of this structure

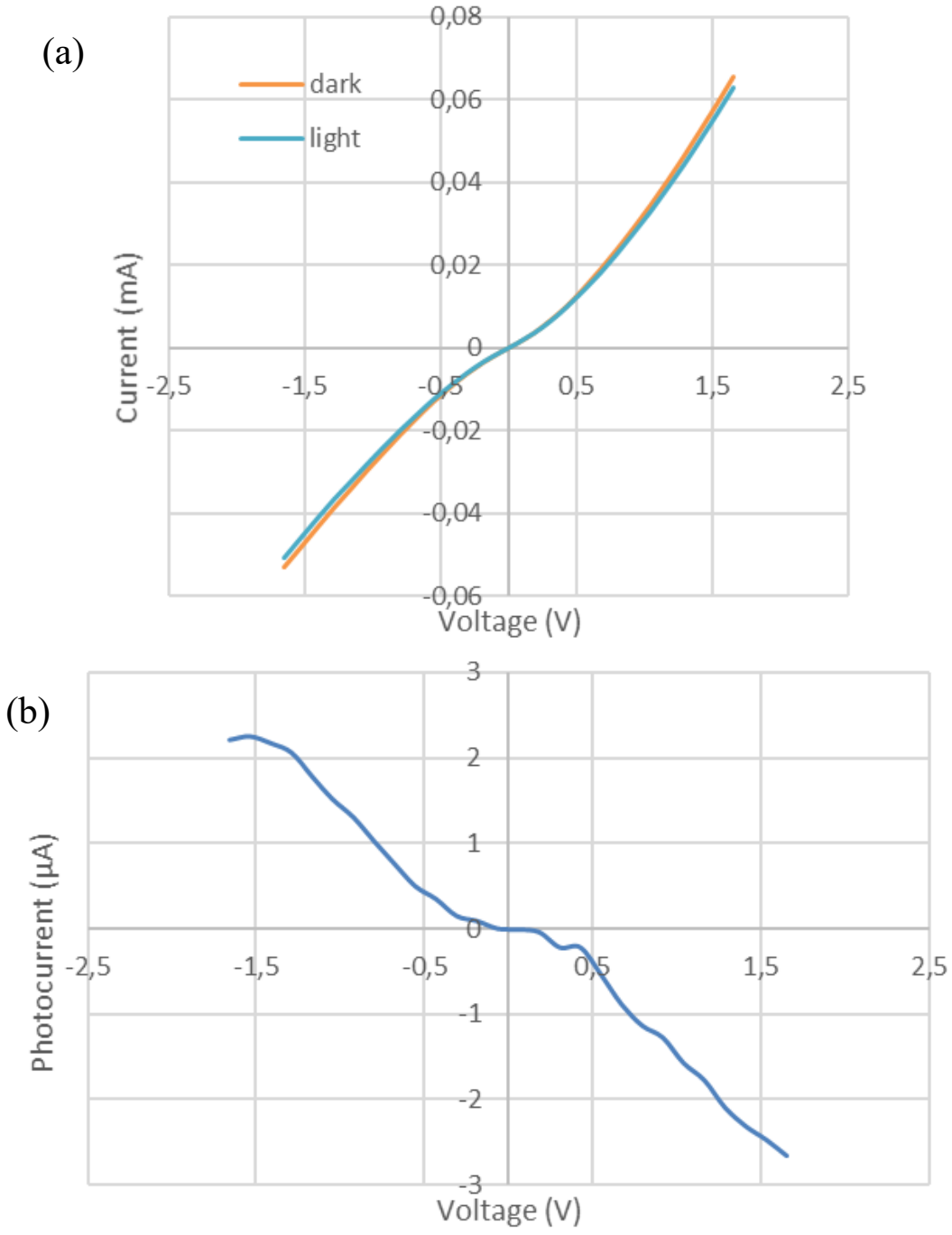

Figure 101: Measurements under AM1.5G solar simulator: a) I-V curves in dark and under illumination. b) photocurrent versus voltage

4.7 Conclusion

In this chapter, we presented the major results we obtained on the deposition of graphene electrode, MO (ZnO) and absorber (La_2CuO_4) layers using different different deposition techniques. Even if some adequate properties have been obtained on some materials, it is clear that it contributes more to lay the groundwork getting a QDSSC device than to get one. It appears that full fabrication of a cell could more probably be based on different fabrication techniques, each of those being more dedicated to get higher performance of one layer.

References

1. Rani, P. and A.S. Kumar, *A Spectroscopic Study of Th (IV) Ion in Aqueous Medium and Its Analytical Importance*. 2010.
2. Garip, Ş., *The characterization of bacteria with Fourier transform infrared (FTIR) spectroscopy*. 2005, Citeseer.
3. Mohiuddin, S.F., *Electrical and optical characterization of PLD grown films of barium strontium titanate*. 2011, Northern Illinois University.
4. Ibrahim, R.K., et al. *Enhance the solar cell efficiency by reduction of reflection losses*. in *IOP Conference Series: Materials Science and Engineering*. 2019. IOP Publishing.
5. Akhtar, T.A., et al., *The tomato cis–prenyltransferase gene family.* The Plant Journal, 2013. **73**(4): p. 640-652.
6. Gomes Silva, C., et al., *Influence of excitation wavelength (UV or visible light) on the photocatalytic activity of titania containing gold nanoparticles for the generation of hydrogen or oxygen from water.* Journal of the American Chemical Society, 2010. **133**(3): p. 595-602.
7. Hassanien, A. and A.A. Akl, *Effect of Se addition on optical and electrical properties of chalcogenide CdSSe thin films.* Superlattices and Microstructures, 2016. **89**: p. 153-169.
8. Hassanien, A.S. and A.A. Akl, *Influence of composition on optical and dispersion parameters of thermally evaporated non-crystalline Cd50S50− xSex thin films.* Journal of Alloys and Compounds, 2015. **648**: p. 280-290.
9. Abou-Ras, D., T. Kirchartz, and U. Rau, *Advanced characterization techniques for thin film solar cells*. 2016: John Wiley & Sons.
10. Hamadani, B.H. and B. Dougherty, *Solar cell characterization*, in *Semiconductor Materials for Solar Photovoltaic Cells*. 2016, Springer. p. 229-245.
11. Schroder, D.K., *Semiconductor material and device characterization*. 2015: John Wiley & Sons.
12. Kassier, G.H., *The characterization of bulk as-grown and annealed ZnO by the Hall effect*. 2006, University of Pretoria.
13. Mienie, S., *Electrical characterization of materials and devices for photovoltaic applications*. University of Pretoria.
14. Skoog, D.A., et al., *Fundamentals of analytical chemistry*. 2013: Nelson Education.
15. Nanakoudis, A., *What is SEM? Scanning electron microscope technology explained.* June 7, 2018.
16. González, B.G.-D.J.G., *SEM & AFM analysis for silicon-based solar cells.* 2014.
17. Technologies, K., *Atomic Force Microscopy - What is it?* 2019.
18. Ye, D., et al., *Growth of uniformly aligned nanorod arrays by oblique angle deposition with two-phase substrate rotation.* Nanotechnology, 2004. **15**(7): p. 817.
19. Azizi, A. and S. Sadrnezhaad, *Effects of annealing on phase evolution, microstructure and magnetic properties of mechanically synthesized nickel-ferrite.* Ceramics International, 2010. **36**(7): p. 2241-2245.
20. Xiao, W., et al., *Synthesis, characterization, and lithium storage capability of AMoO4 (A= Ni, Co) nanorods.* Chemistry of Materials, 2009. **22**(3): p. 746-754.
21. Jia, C., et al., *Annealing temperature dependence of ferromagnetism in Co-doped TiO2 nanofibres.* Materials Science and Engineering: B, 2007. **140**(1-2): p. 10-14.

22. Sato, Y., et al., *Electrolyte dependence of transport properties of SrTiO3 electric double layer transistors.* Japanese Journal of Applied Physics, 2017. **56**(5): p. 051101.
23. Van Benthem, K., C. Elsässer, and R. French, *Bulk electronic structure of SrTiO 3: Experiment and theory.* Journal of Applied Physics, 2001. **90**(12): p. 6156-6164.

Conclusions and Perspectives

Conclusions

The significant impact of third generation solar cells based on nanostructures may hold the key to solving the world's increasing demand for eco-green and low-cost energy. To that end, this thesis investigates ways in improving the active layer in solar cells based on quantum confinement energy generated in nanoparticles (QDs). My initial goal was targeting a full working cell based on new materials within my Ph.D.. This objective was particularly challenging and, time being, I came around revisiting this idea. My work was then built around investigating material growth conditions and corresponding material properties in order reaching the initial goal eventually.

In this work, I assessed numerous growth techniques on as many materials, evaluating pros and cons of each, considering each couple "elaboration technique-material" either by itself than by its behavior in a full cell fabrication sequence. Even if I investigated some other materials, I focused my work on the active layer considering a La_2CuO_4 material. Then, I characterized it in respect of solar absorption, electron mobility and the ability to be implemented probably in the design. Similarly, my study concentrated on the transport layer introduced as MOs (ZnO) and last the electrodes represented by the 3D structural sheets of graphene (LIG). Consequently, a parametric investigation on the growth and fabrication of the QDSSC layer, then enhancing the PLD, sputtering, and chemical growth conditions and revealing the fundamental properties of QDSSCs. Even if a first solar cell structure has been made, no significant photoelectric behavior has been obtained

Active layer outcomes

It is noted that the influence of the increase in the NPs numbers at the fabrication stage in the active layer did not enhance efficiency as it was expected. It starts an aggregation between the NPs, which reduces the quantum confinement energy generated by the absorbed light in the QDs structures (moving away from quantum level). Consecutively, more considerable recombination is taking place and less efficient carrier extraction occurs in that layer that leads to degrade the photocurrent and efficiency of the cell.

Transfer layer outcomes

Successful fabrication and growth of the transfer layer (ZnO) via sputtering and PLD has been obtained at low temperature and on various substrates like LIG, silicon, and glass. It has been identified that the growth parameters (temperature, pressure, and deposition time) are vital to control the crystallinity, morphology, and defect levels in the synthesized nanostructures. The issue of controlling the orientation of the nanostructures was addressed. SEM, XRD, and AFM analysis show that the nanostructures are highly crystalline.

The chemical synthesis using the SILAR technique was very promising on glass and ITO substrate via the literature, but the hexagonal nanorods were distributed in a non uniformly way during the growth on the LIG and that is due to week attachment force between the two even though a seed layer of ZnO partially solved this issue and supported the growth of perpendicular nanorods on the surface of the LIG. However, due to bubble formation in the solution, many spots without any growth appeared on the surface. The configuration of nano-hexagonal rods was our original target for the solar cell to be coated by the NPs of the absorber layer, but the lack of uniform layer of ZnO (presence of openings) will create a short circuit between the electrodes. More optimization should be done on this point.

Electrodes layer outcomes

The results of the LIG fabrication and the CVD graphene growth help in estimating a comparison between the two technologies in terms of optimizing an electrode layer for the solar cell structure. The main factors that distinguished the role of the graphene type (CVD or LIG) were the physical characteristics (flexibility, transparency, conductivity, and endorsement) and concerns about fabrication cost.

The LIG was the right candidate for the back electrode in the solar cell since it has a good conductivity (~60Ω/cm), flexibility since it was built on a flexible substrate. Also, an advantage of the LIG was the economic cost in term of material needed in the fabrication process (Kapton), the speed of fabrication (a few seconds for one cm^2) and last the equipment/conditions required for the fabrication which is a laser CNC machine without any adjusted temperature or pressure environment.

On the other hand, the thin graphene layer (single sheet has 3-5 atomic carbon structure) created by the CVD has higher transparency comparing to the LIG (vertical graphene sheets almost aligned to each other) that allowed it to be used as a top electrode. The drawback of the CVD process was the high-cost in the fabrication since it required more materials, time and energy comparing to the LIG.

Device outcomes

The fabrication of a solar cell structure based on NPs as an active layer was investigated via multiple techniques. The results showed the possibility of using the different layers separately for their task in the device. But, due to the roughness of LIG that might cause a short circuit between the top/bottom electrodes, the fast charge recombination in the active layer that the electrodes could not overcome, and even an unwanted layer (oxidation of graphene) created during the fabrication, several charge barriers emerge that give a shallow efficient device.

Perspectives

In this thesis, significant challenges come across for QD solar cell development and among them the strain accumulation when a large number of QD layers were fabricated. While the incorporation of a strain compensation layer such as AZO was also attempted to decrease the total strain within the QD layers during this work, the initial experimental results were not very encouraging, indicating that further study and development of the strain balance effect of MOs based layer on QD structure are necessary. It would be worth changing the fabrication technique and growth condition of QDs to confirm their best location in the active region and, alternatively, increasing the total absorption of QDs.
Furthermore, eliminating losses and short circuits in the electrodes is worth to have more dedicated study as the growth of the active layers on an inexpensive substrate with light-trapping strategies on it. This approach would allow structures such as MO on graphene to reduce the total cost of the QDSSCs and make it possible to fabricate smaller-scale light-trapping structures on flexible substrates. This strategy could be a worthwhile subject for future investigation.

Table of Figures

Table of Tables

Abstract:
Among all harvesting technologies, photovoltaic technology is, right now, the one that can provide the highest level of power for mobile applications. Here, we focus on the development of new materials providing a sustainable and low environmental footprint approach for the fabrication of flexible solar cells. Based on a polymer flexible support, different fabrication technologies have been investigated to elaborate materials with adequate performance for building such a solar cell. Low cost laser writing technique has been used to produce nanostructured graphite electrodes using even the polymer substrate as base material. Numerous technologies, based either on physical or chemical deposition process, have been investigated to produce the absorbing material. This one is made of nanoparticles, i.e. semiconductor quantum dots. Such demonstrations have already been successfully demonstrated using mainly lead based material. In our goal targeting green technology, there is no way using such a material. We focus then on an exploratory material, a copper and lanthanum based oxide. Among the different fabrication methods, we focused on pulsed laser and sputtering deposition techniques. In order going to a solar cell structure, absorbing material has been deposited on the nanostructured graphite electrodes and the obtained film has been characterized. First attempt of a solar cell using a transparent conductive oxide, based on zinc, has been launched. A very low photoelectric behavior has been observed.

Résumé:
Parmi les différentes technologies de récupération d'énergie, la technologie photovoltaïque est celle qui fournit actuellement le plus haut niveau pour les applications mobiles. Ce travail est focalisé sur le développement de nouveaux matériaux permettant d'obtenir des cellules solaires flexibles fondées sur des matériaux et procédés durables et à faible empreinte écologique. A partir d'un support flexible en matériau polymère, différentes technologies de fabrication ont été explorées pour élaborer les matériaux constitutifs d'une cellule solaire. Une technique d'écriture laser a été utilisée pour fabriquer une électrode nanostructurée en graphite directement à partir du support polymère. De nombreuses technologies d'élaboration, soit par voie physique soit par voie chimique, ont été étudiées pour la réalisation du matériau absorbant. Celui-ci est réalisé à partir de nanoparticules de semiconducteurs ou boites quantiques. De nombreuses démonstrations de l'utilisation de boites quantiques en photovoltaïque ont déjà été faites, mais majoritairement basées sur des matériaux à base de plomb. De tels matériaux ne sont évidemment pas dans la lignée de mise au point d'une technologie à faible impact environnemental. Nous nous sommes alors attachés à étudier un matériau des plus exploratoire dans ce domaine, un oxyde de cuivre et lanthane. Parmi les différentes techniques de fabrication, deux ont particulièrement été utilisées, le dépôt par pulvérisation cathodique et celui par laser pulsé. Ce matériau a été déposé sur l'électrode inférieure en graphite nanostructuré de manière à obtenir une caractérisation proche de celle d'une cellule solaire. Un premier essai de cellule a d'ailleurs été tenté en utilisant une électrode supérieure transparente en oxyde de zinc. Ce premier essai n'a malheureusement pas été des plus concluants, un faible photocourant ayant été obtenu.